Development of a Plasmonic Refractive Index Sensor with Enhanced Sensitivity

by

Rabiul Al Mahmud

MASTER OF SCIENCE
IN
ELECTRICAL AND ELECTRONIC ENGINEERING

Department of Electrical and Electronic Engineering
Islamic University of Technology (IUT)
Board Bazar, Gazipur-1704, Bangladesh.
July, 2020.

© 2020 Rabiul Al Mahmud
All Rights Reserved.

CERTIFICATE OF APPROVAL

The thesis titled,"**Development of a Plasmonic Refractive Index Sensor with Enhanced Sensitivity**" submitted by Rabiul Al Mahmud, St. No. 171021018 of Academic Year 2017-18 has been found as satisfactory and accepted as partial fulfillment of the requirement for the Degree MASTER OF SCIENCE IN ELECTRICAL AND ELECTRONIC ENGINEERING on July 15, 2020.

Board of Examiners:

Dr. Rakibul Hasan Sagor (Supervisor)
Associate Professor, Chairman
Electrical and Electronic Engineering Department,
Islamic University of Technology (IUT), Gazipur.

Dr. Md. Ruhul Amin (Ex-Officio)
Professor and Head, Member
Electrical and Electronic Engineering Department,
Islamic University of Technology (IUT), Gazipur.

Dr. Mohammad Rakibul Islam
Professor and Dean of FSTE, Member
Electrical and Electronic Engineering Department,
Islamic University of Technology (IUT), Gazipur.

Dr. Golam Sarowar
Professor, Member
Electrical and Electronic Engineering Department,
Islamic University of Technology (IUT), Gazipur.

Dr. Mohammad Jahangir Alam
Professor, Member (External)
Electrical and Electronic Engineering Department,
Bangladesh University of Engineering and Technology (BUET), Dhaka.

Declaration of Candidate

It is hereby declared that this thesis report or any part of it has not been submitted elsewhere for the award of any Degree or Diploma.

Dr. Rakibul Hasan Sagor
Associate Professor,
Electrical and Electronic Engineering department,
Islamic University of Technology (IUT),
Date: July 15, 2020.

Rabiul Al Mahmud
Student No.: 171021018,
Academic Year: 2017-18,
Date: July 15, 2020.

Dedicated to my family members

Table of Contents

List of Figures

List of Tables

List of Abbreviations

SPP	Surface Plasmon Polariton
MIM	Metal Insulator Metal
IMI	Insulator Metal Insulator
RI	Refractive Index
FOM	Figure of Merit
QF	Quality Factor
ER	Extinction Ratio
SR	Sensing Resolution
FEM	Finite Element Method
EM	Electromagnetic
TM	Transverse Magnetic
TE	Transverse Electric
TEM	Transverse Electric and Magnetic

Acknowledgment

All praise and gratitude be to Allah, the most beneficent, the most merciful.

Also I would like to express my sincere gratitude to my thesis supervisor Dr. Rakibul Hasan Sagor, Associate Professor, Department of Electrical and Electronic Engineering, Islamic University of Technology (IUT), for the continuous support of my M.Sc. study and research with his patience, motivation, enthusiasm, and immense knowledge. His guidance helped me in all the time of engineering study, research, and up to writing of this thesis.

I would like to thank all the faculty members of the department of Electrical and Electronic Engineering, Islamic University of Technology (IUT) for their support and inspiration.

Finally, I must express my very profound gratitude to my parents and to my family for providing me with unfailing support and continuous encouragement throughout my tenure of study and through the process of researching and writing this thesis. This accomplishment would not have been possible without them.

Rabiul Al Mahmud
July, 2020

Abstract

Plasmonic devices are based on the propagation of surface plasmon polaritons. In this thesis, waveguide design with metal-insulator-metal configuration is considered to support the propagation of the surface plasmon polaritons. Silver has been placed as metal. The design topology of the refractive index sensor, as well as its design parameters, are the fundamental parameters to improve the performance of the sensor. The plasmonic refractive index sensors with a straight waveguide and different side coupled resonators have been proposed and analyzed. The equilateral triangular, regular pentagonal, and semi-circular resonator are the three different designs of the resonator. The resonators are of disc-type and ring-type. The finite element method has been implemented as a numerical computational tool. The scattering boundary condition is implemented on the non-port boundary of the sensors. The detection of refractive index change has been numerically simulated and analyzed using COMSOL Multiphysics. The simulation environment has been validated by re-simulating an existing sensor from the literature. The re-simulation results have been compared and found a maximum error of 4.14% in sensitivity calculation. The sensitivity achieved using our proposed designs has been found to be 2713 nm/RIU with a high figure of merit (FOM) of 35.1 for the design with the ring-type triangular resonator. It is shown that the sensor can detect a refractive index change of $\mathbf{3.68 \times 10^{-6}}$, which is the sensing resolution of the sensor, for dielectrics whose refractive indices are between 1 to 1.03 and also between 1.33 to 1.42. This range of refractive index indicates the application of the sensor as a gas sensor and biosensor. Simplicity and compact design with high refractive index sensitivity and FOM of the plasmonic device make the design comparable with many excellent sensors in the literature. The other significant applications of the sensor cover bio-sensing, biomedical applications like cancer cell detection, nanosensing, and optical filter applications.

Chapter 1

Introduction

1.1 Surface Plasmon Polaritons

The reduction of size and integration into external devices of the semiconductor devices, circuits, and components are the key factors for the performance, speed, and ease-of-use of them. Nevertheless, the integration of electronic devices for sensing and information processing is highly approaching the fundamental speed and bandwidth limits. It causes hindrance to the exploration of further advance in the area of science and technology. Electrons are the carrier of the information in electronic devices, and light can be a possible replacement. However, one of the significant problems of the electromagnetic waves as the information carrier in the optical signal processing devices and integrated circuits is the low levels of integration and miniaturization available. In this sense, electronic devices are far better than optical devices. This problem is the direct cause of the diffraction limit of light in the dielectric media. The diffraction limit does not permit the localization of electromagnetic waves into nano-regions smaller than the wavelength of light in the material.

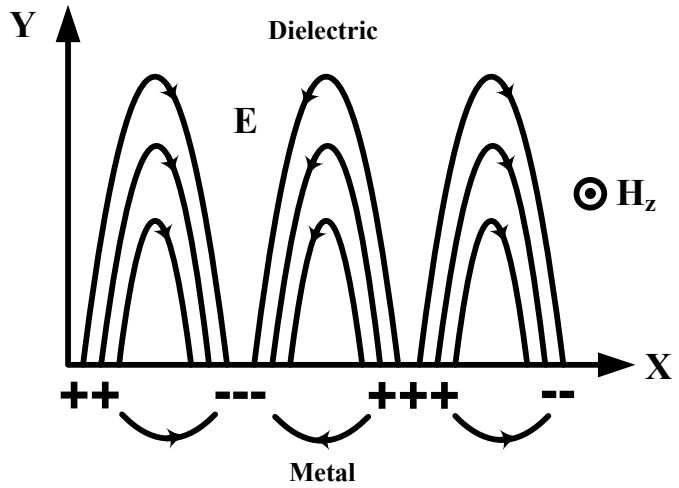

Figure 1.1: SPP propagation on the interface of metal and dielectric.

The choice of the material is significant; materials with negative permittivity are one of the most realizable solutions to overcome diffraction limit and localize electromagnetic waves in nanoscale. The available metals can be utilized for this purpose.

In the last few years, researchers have shown their interest in the optical structures where surface plasmon polaritons (SPPs) can propagate. Surface plasmon refers to charge motion in metal, and polariton refers to the electromagnetic wave propagation in the dielectric. So SPPs are formed due to the interaction of electromagnetic fields and electron oscillations, which traverse on the interface between a conductor and a dielectric [1]. It is important to note that SPPs can overcome the diffraction limit and confine light in subwavelength dimensions, which offers nanoscale plasmonic devices [2], [3]. SPPs are the basis of plasmonics, which can be utilized in highly integrated optical devices [4]. The SPP propagation on the interface of metal and dielectric has been depicted in Fig. 1.1.

1.2 Metal Insulator Metal (MIM) Topology and Plasmonic Devices

As mentioned before, the metallic structure and interfaces are known to guide SPP; various nanostructure has been proposed to guide SPP using metals. The proposed structures includes thin metal films, chains of metal nanoparticles, cylindrical metal nanorods and nanoholes in a metallic medium, Insulator-Metal-Insulator (IMI), Metal-Insulator-Metal (MIM), slot waveguides in the form of rectangular nanogaps in thin metal films, sharp metal wedges, nano grooves in metal substrates, and hybrid plasmonic waveguides formed by dielectric nanowires coupled to a metal surface [3]. The propagation loss and field confinement of the electromagnetic wave are the parameters that need to be acknowledged during designing plasmonic devices. The different structures show different profiles of propagation loss and localization of SPP. Metal films (single-surface) and IMI structures are better for long-range transmission; decreasing the thickness of the film or strip results in more reduced localization of the long-range mode. The MIM structure provides strong confinement of the filed with a considerable amount of propagation loss. One of the major requirements for interconnections in highly integrated optical circuits is the strong field confinement[1]–[3].
Among these many possible configurations for the realization of SPPs propagated plasmonic devices, Metal-Insulator-Metal (MIM) structured waveguide can be used to convey both electrical and optical signals in an integrated circuit. It provides a way of integrating traditional electronic circuits and photonic circuits on the same chip [5]. Due to the unique optical feature of MIM configurations, they have received much interest in the design of optical devices.The MIM configuration offers nanoscale plas-

monic devices like refractive index sensors [6]–[11], filters [12], [13], switches [9], [14], demultiplexers [15], [16], couplers [17], splitters [11], [18], etc.

1.3 Plasmonic Refractive Index Sensor

The Refractive index sensor is one of the essential devices among the plasmonic devices for its application to detect the refractive indices of different dielectric materials present in the design of the sensor. The dielectric materials include a wide range of materials like gaseous materials, bio-molecules, chemicals, etc. The MIM waveguides inherit more propagation loss than silicon photonic waveguides [19], but demonstrate strong field confinement[20]. Propagation loss will have less weight in comparison with field confinement for sensing purposes [20]. SPPs in MIM structure is an appropriate candidate for compact integrated optical circuits, and also on-chip applications can be realized.

Table 1.1: Refractive Indices of different cancer cells and their corresponding normal cells [24].

Cell Name	Cell Type	Concentration Level (%)	Refractive Index
Jurkat	Normal Cell	30-70	1.376
	Blood Cancer	80	1.39
HeLa	Normal Cell	30-70	1.368
	Cervical Cancer	80	1.392
PC12	Normal Cell	30-70	1.381
	Adrenal Gland Cancer	80	1.395
MDA-MB-231	Normal Cell	30-70	1.385
	Breast Cancer	80	1.399
MCF-7	Normal Cell	30-70	1.387
	Breast Cancer	80	1.401
Basal	Normal Cell	30-70	1.36
	Skin Cancer	80	1.38

Most vital applications of the refractive index sensors are in biomedical engineering like cancer cell detection, blood component measurements, health care applications [22]–[25]. Quantification of refractive indices of different food and chemical products can assure the quality of that particular [26]. The experimental data from Cole *et. al.* [21], refractive index versus concentration data for few proteins and viruses has been depicted in Fig. 1.2 and 1.3. Using these data, Al Mahmod *et. al.* [27] has designed a refractive index sensor which has a sensitivity of 1383 nm/RIU. The refractive in-

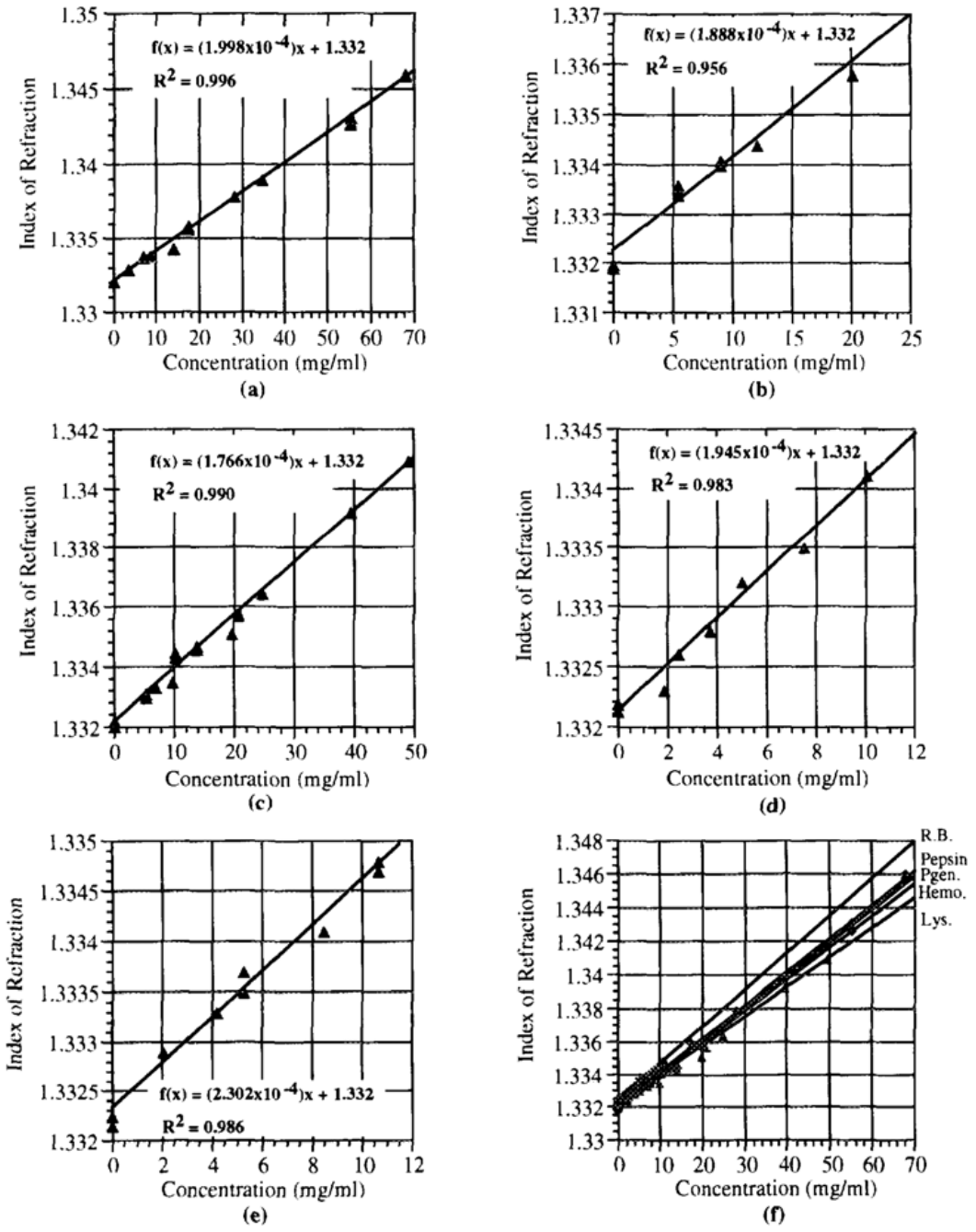

Figure 1.2: Refractive index versus concentration data for selected proteins: (a) pepsin, (b) hemoglobin, (c)lysozyme, (d) pepsinogen, (e) ribonuclease. (f) A compilation of protein data [21].

dices of different blood groups, glucose, and hemoglobin concentration in the blood are reported to be sensed by the proposed refractive index sensors. The variation of the refractive index with these parameters have been depicted in Fig. 1.4 and 1.5. The refractive indices of different cancer cells and their corresponding normal cells have also been reported in the literature, has been shown in Table 1.1. In most of the cases of the biological specimen, the refractive index is found to be between 1.33 to 1.40.

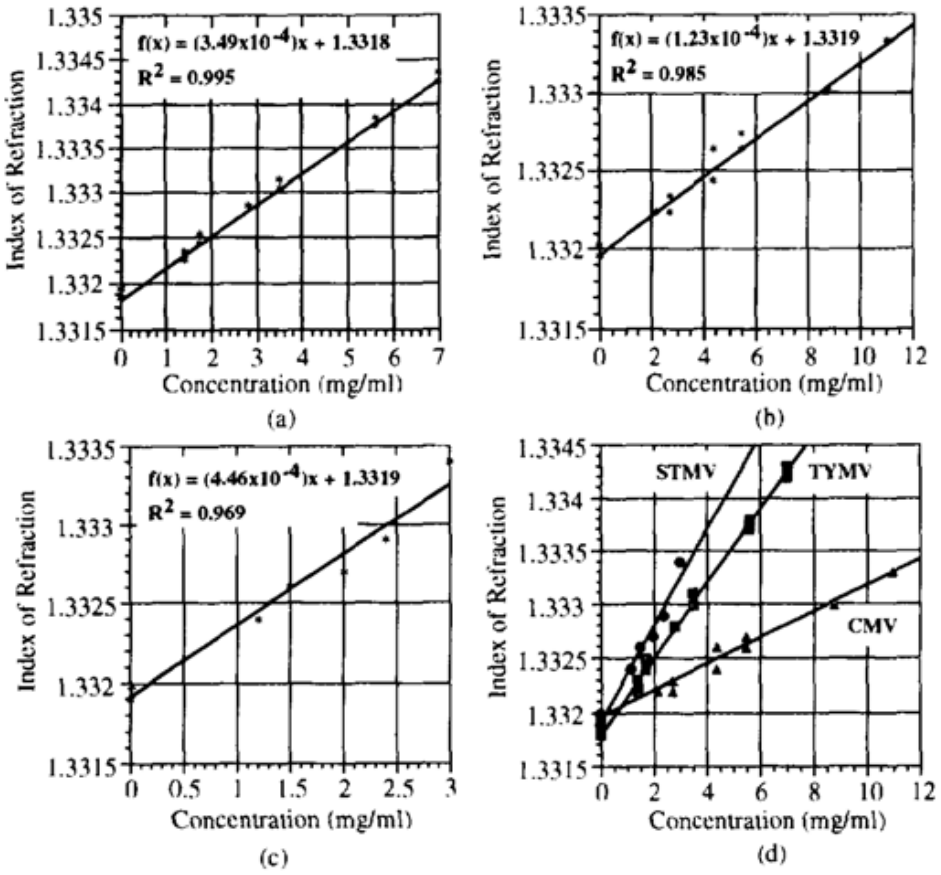

Figure 1.3: Refractive index versus concentration data for selected viruses: (a) turnip yellow mosaic virus (TYMV), (b) satellite tobacco mosaic virus (STMV), (c) cucumber mosaic virus (CMV) [21].

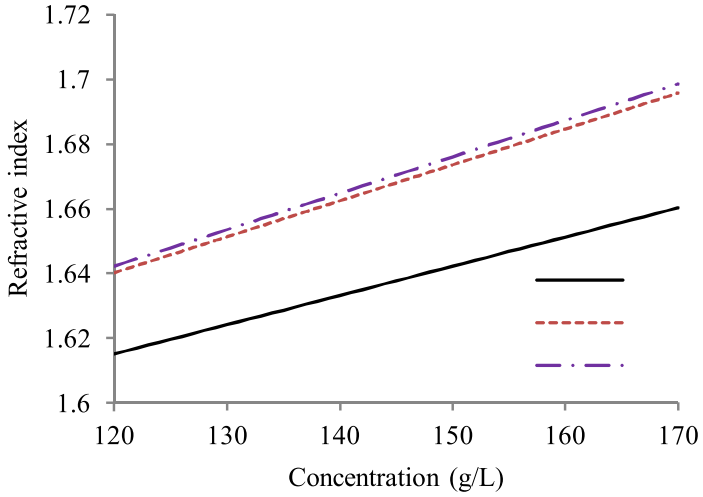

Figure 1.4: Variation of RI of different blood groups against concentration of hemoglobin level (for λ = 750 nm, T = 300 K) [22].

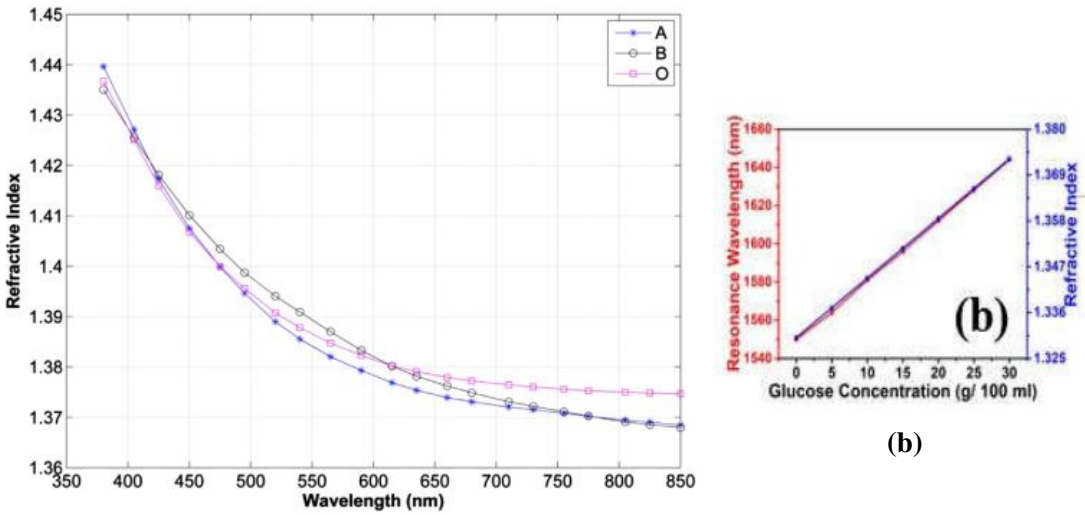

(a) (b)

Figure 1.5: (a) Variation in refractive indices of three different blood groups with wavelength for C_A = 146.2 g/L, C_B = 111.1 g/L and C_O = 108.9 g/L in room temperature [8], (b) Glucose concentration versus refractive index [23].

In this thesis, a few designs of refractive index sensor will be proposed that will have enhanced sensitivity and FOM. The proposed designs will be presented for the sensing of gaseous components (refractive index 1.0 to 1.03) and for sensing biological components (refractive index 1.33 to 1.40). The sensors can be implemented as bio-implantable lab-on-chip applications.

1.4 Literature Review

Surface plasmon based sensors have been a much-researched field from the late 1980s. Surface plasmon resonance (SPR) sensors have been presented in integrated optical devices. Batchelder *et. al.* presented the SPR based optical sensor that can detect specific material in 1989 [28]. Dielectric and metal films were integrated with a planar optical waveguide to support SPR based sensor for the aqueous environment by Lavers *et. al.* in 1994 and for detecting the change in transmitted power by Harris *et. al.* in 1995. More other integrated optical surface plasmon resonance (SPR) sensors have been demonstrated in the late 1990s [29]–[33]. The thin metal films were deposited on top of integrated optical waveguide systems as a platform for the attachment of sensing films. These SPR sensors were designed in dielectric materials with low refractive index contrast; thus, the dimensions of these devices were large and unsuitable for lab-on-chip applications. Few other SPP sensors have been presented based on various detection schemes. For example, SPP resonance of nanoparticles [34], [35], enhanced transmission through nanohole arrays [36], [37] are presented in 2003-2007. Vesseur *et. al.* has demonstrated gold nano-resonator fabrication using focused-ion-

beam milling for SPP in 2008.

In 2010, Jin *et. al.* has designed a refractive index sensor with a side coupled-cavity using MIM waveguide where SPP can traverse [38]. A sensitivity of 454.5 nm/RIU has been investigated in that research by simulating the sensor by finite difference time domain (FDTD) calculations with the perfectly matched layer (PML) as an absorbing boundary condition. Xu *et. al.* proposed a double cavity sensor design, which is a modified configuration than Jin *et. al.* with the purpose of the improved sensitivity.

In regards to the quality and performance of a plasmonic device for sensing application, sensitivity, and FOM have the most significance [39]. How well a sensor can detect the refractive index change and how easily detection can be performed, can be investigated by those two features. With the calculation of the Figure of Merit (FOM), plasmonic responses of different designs with a single sharp notch spectrum can be compared to get the idea of the quality. As it is easier to detect a resonance shift for narrow lines, sensitivity relative to Full Width at Half Maximum (FWHM), which is FOM, becomes the key feature to ascertain the quality of the sensor. The objectives of the researchers are found to be the improvement of the sensitivity as well as the FOM of the sensors by proposing different geometric designs in a small area. The comparison of the RI sensors with MIM configuration, silver (Ag) used as metal, reported in the literature has been represented in Table 1.2 with the year of publication, the spectrum type, the topology of the design, the material modeling implemented during the computation, the maximum sensitivity and the FOM of the sensors.

Table 1.2: Comparison of the RI sensors with MIM configuration reported in the literature with silver as metal

Ref.	**Year**	**Spectrum**	**Topology**	**Metal Model**	**Sensitivity** (nm/RIU)	**FOM** (RIU^{-1})
[38]	2010	Notch-type	Side coupled single cavity	Lorentz-Drude	454.5	-
[40]	2013	Lorentzian	Double metal disk cavities	Drude	1160	80
[41]	2014	Notch-type	Side coupled double cavities	Drude	1030	-
[42]	2014	Notch-type	Loop-shaped stub	Drude	970	21

(Continued)

Ref.	Year	Spectrum	Topology	Metal Model	Sensitivity (nm/RIU)	FOM (RIU^{-1})
[43]	2015	Notch-type	Tooth-shaped cavity	Drude	733	30.5
[44]	2015	Notch-type	Side-coupled hexagonal cavity	Lorentz-Drude	1562	38.6
[45]	2015	Lorentzian	Ring resonator with two straight MIM waveguides	Debye-Drude	868	43.9
[46]	2015	Fano-resonance	Tooth-shaped stubs	Drude	1060	176.7
[47]	2015	Lorentzian	Ring resonator	Drude	3960	-
[48]	2015	Fano-resonance	A stub and groove resonator	Drude	1260	-
[49]	2016	Lorentzian	Fillet cavity	Drude	1496	124.6
[50]	2016	Fano-resonance	Side-coupled cavity	Lorentz	985	28.2
[51]	2016	Lorentzian	Hexagonal ring cavity	Lorentz-Drude	4270	22
[52]	2016	Lorentzian	Nano-disk resonator	Drude	1555	87.9
[53]	2016	Fano-resonance	Double rectangular cavities	Debye-Drude	509	7.5
[54]	2016	Fano-resonance	Cascaded double asymmetric cavities	Drude	-	74.3
[55]	2017	Lorentzian	Elliptical-ring resonator	Drude	780	-
[56]	2017	Lorentzian	Metallic nano-rods in race-track resonator	Lorentz-Drude	2610	52
[8]	2017	Lorentzian	Silver nano-rods in a square resonator	Lorentz-Drude	2320	-
[57]	2017	Fano-resonance	Rectangular and ring resonators	Debye-Drude	1125	74

(Continued)

Ref.	Year	Spectrum	Topology	Metal Model	Sensitivity (nm/RIU)	FOM (RIU^{-1})
[58]	2017	Fano-resonance	MIM waveguide-coupled trapezoid cavity	Debye-Drude	750	65.2
[59]	2017	Lorentzian	Side-coupled stub-hexagon resonators	Drude	560	178
[60]	2018	Lorentzian	Double side-coupled square ring resonators	Drude	806	66
[61]	2018	Notch-type	Octagonal ring cavity	Lorentz-Drude	1540	-
[62]	2018	Lorentzian	Array of hexagonal nano-holes	Drude	3172	101
[63]	2018	Fano-resonance	Square type split-ring resonator	Drude	1700	60.7
[64]	2018	Notch-type	Concentric ring resonators	Drude	1060	203.8
[7]	2018	Fano-resonance	Dual side-coupled ring resonators	Debye-Drude	1160	-
[22]	2018	Lorentzian	Pair of elliptical Resonators	Drude	1100	224
[27]	2018	Lorentzian	Two MIM waveguides coupled to a ring resonator	Drude	1383	-
[65]	2018	Notch-type	Two slot waveguide based micro rings that encircle a gold disc	-	800	37
[6]	2019	Fano-resonance	Circular split-ring resonator cavity	Debye-Drude	1114.3	55.71
[10]	2019	Notch-type	Si ring resonator	Drude	636	211.3
[66]	2019	Fano-resonance	End-coupled vertical cavity side-coupled by two horizontal cavities	-	1382	35.3

(Continued)

Ref.	Year	Spectrum	Topology	Metal Model	Sensitivity (nm/RIU)	FOM (RIU^{-1})
[67]	2019	Fano-resonance	two triangle stubs coupled with a circular split-ring resonance cavity	Debye-Drude	1500	65.2
[68]	2019	Notch-type	Six square micro-ring cavities of different sizes	Debye-Drude	700	191.6
[69]	2019	Fano-resonance	MIM waveguide with two stubs coupled with one ring resonator	Debye-Drude	1268	280
[70]	2019	Lorentzian	End coupled square ring resonator	Lorentz-Drude	1367	25
[71]	2019	Fano-resonance	Tooth cavity-coupled ring splitting cavity	Debye-Drude	1200	-
[72]	2020	Notch-type	two concentric double-square resonators	Lorentz-Drude	1380	104
[73]	2020	Notch-type	Dumbbell-shaped cavity slots	Drude	1260	120

Notch filter and band-pass filter can be implemented using the notch-type and Lorentzian type response of frequency spectrum respectively [74]–[76]. Some of the proposed designs of the refractive index sensor by the researchers have been depicted in Fig. 1.6. The resonators are found to be of some regular shaped geometry or derived from the regular geometry to improve the performance of the sensors. Both the disc-type and the ring-type resonator are found to be proposed by the researchers.

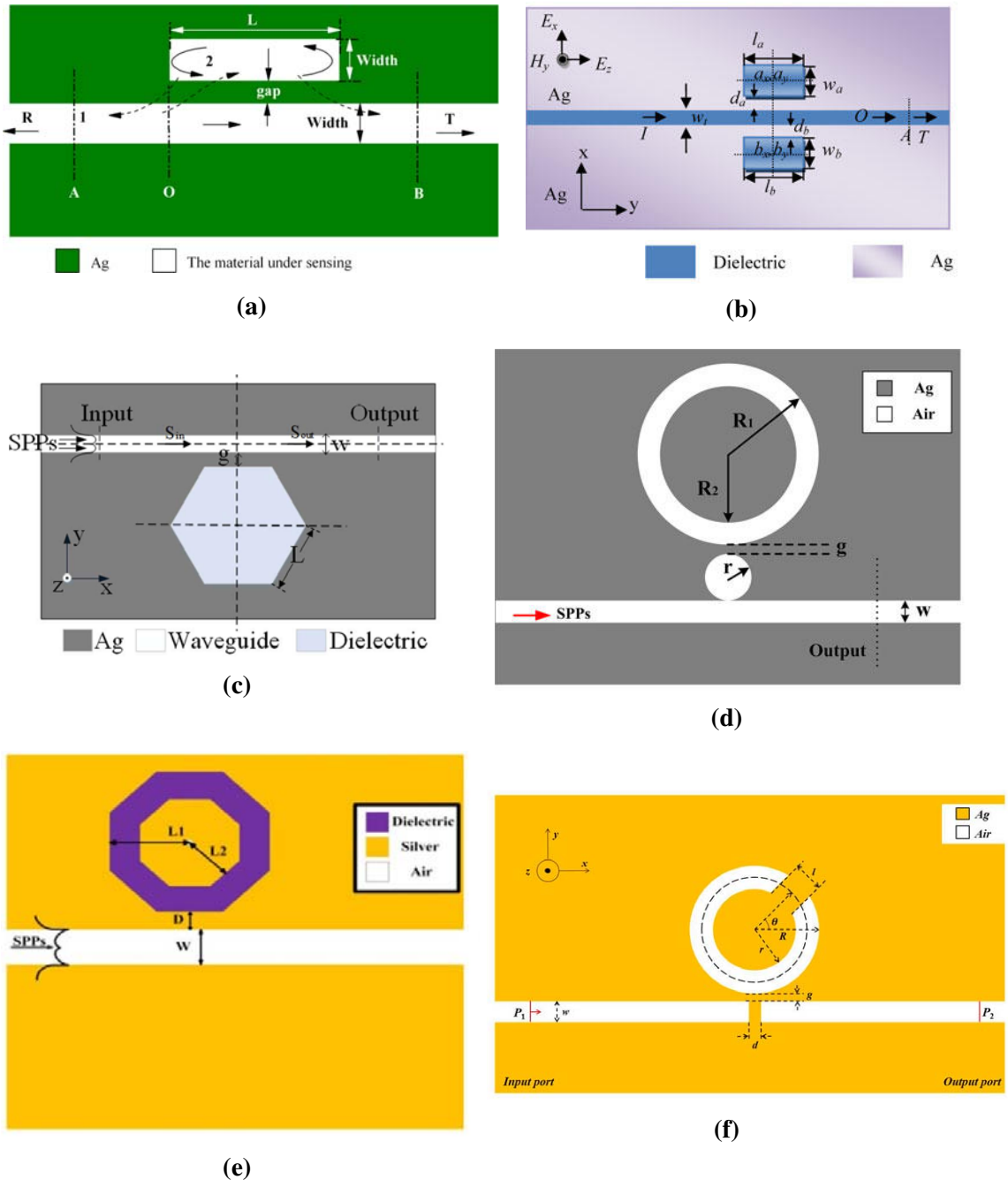

Figure 1.6: The proposed designs of refractive index sensors with MIM configuration in the literature by (a) Jin *et. al.* [38], (b) Xu *et. al.* [41], (c) Xie *et. al.* [44], (d) Li *et. al.* [77], (e) Ghorbani *et. al.* [61], and (f) Wang *et. al.* [6]

1.5 Thesis Objective

The principal objective of this thesis is to design a refractive index sensor with MIM configuration to make an improvement of the sensitivity and FOM of the refractive index sensor, which can be realized as a filter and biosensor. More particularly, the objective incorporates the following:

- To propose new design of a refractive index sensor with MIM configuration.
- To investigate the sensitivity and FOM of the refractive index sensor and to compare the quality of the sensor with the available sensors in the literature.
- To realize the design of the refractive index sensor as filter and biosensor.

1.6 Thesis Outline

Chapter 1 introduces the basics of SPPs with the waveguide of MIM configuration and discusses the different plasmonic devices, including the refractive index sensor. The contribution of the researchers in the field of refractive index sensor to date and the thesis outline has been discussed.

Chapter 2 discusses the basic wave equations and material modeling of the metals. The discussion also includes the details of FEM with the way of theoretical calculation of S-parameters and transmittance.

In the **Chapter 3**, the theoretical investigation of ring resonator with MIM configuration is discussed. The discussion of the different parameters ascertaining the quality of a good refractive index sensor is included. The re-simulation of an already published sensor has been performed using COMSOL Multiphysics and compared with the former.

Chapter 4 includes the designing of the proposed refractive index sensors. The performance parameters have been investigated for the purpose of exploring the design parameters. The applications of the proposed designs as biosensors and as filters have been presented.

In the **Chapter 5**, a conclusion has been made on the best design in regards to the sensitivity and FOM of the refractive index sensors of the literature. The scopes of the future research in this field has been discussed.

Chapter 2

Wave Theory and Material Modelling

SPPs are formed due to the propagation of electromagnetic waves in dielectric and electrons in the metal. Maxwell's equations describe the electromagnetic property of waves. The propagation, interactions, influence on each other of the electric and magnetic fields can be understood from these equations. The wave equation, which can be derived from Maxwell's equations, governs the propagation of the EM wave in a medium. The intuition of the property of the medium can be achieved from the materials of the medium. Silver and gold are the two most popular metals for the designing of plasmonic devices. Material modeling and boundary conditions are required for computational purposes. The finite element method is one of the numerical tools that can be applied to calculate the electromagnetic field of the plasmonic device. Transmittance is the relationship between the input and output of the device. The performance of the plasmonic devices can be investigated with transmittance.

2.1 Maxwell's and Wave Equations

2.1.1 Maxwell's Equation

Maxwell's equations are the set of expressions, written in differential or integral form, describing the relationships among the fundamental electromagnetic quantities. Electromagnetic analysis requires solving Maxwell's equations. Here the equations are written in differential form as Finite Element Method (FEM) can handle this form. Maxwell's equations for the general time-varying fields can be expressed as

$$\nabla \times \mathrm{H} = \mathbf{J} + \frac{\partial \mathrm{D}}{\partial t}, \tag{2.1}$$

$$\nabla \times \mathrm{E} = -\frac{\partial \mathrm{B}}{\partial t}, \tag{2.2}$$

$$\nabla \cdot \mathrm{D} = \rho, \tag{2.3}$$

$$\nabla \cdot \mathrm{B} = 0, \tag{2.4}$$

where,
E = Electric field intensity,
D = Electric flux density/ displacement,
H = Magnetic field intensity,
B = Magnetic flux density,
J = Current density,
ρ = Electric charge density.

These equations are also known as *Maxwell-Ampere's Law, Faraday's Law, Gauss's Law of electric and magnetic form* respectively. The *equation of continuity* is another fundamental equation for Electromagnetic Wave (EM) wave,

$$\nabla \cdot \mathbf{J} = -\frac{\partial \rho}{\partial t}. \tag{2.5}$$

2.1.2 Constitutive Equations

The *constitutive equations* are also significant for macroscopic properties of the medium in a closed system. The equations are given below,

$$\mathrm{D} = \varepsilon_0 \mathrm{E} + \mathrm{P}, \tag{2.6}$$

$$\mathrm{B} = \mu_0 \left(\mathrm{H} + \mathrm{M}\right), \tag{2.7}$$

$$\mathbf{J} = \sigma \mathrm{E}, \tag{2.8}$$

where, ε_0 is the permittivity of vacuum, μ_0 is the permeability of vacuum, and σ is the electric conductivity. Assuming the velocity of EM wave in vacuum as c_0 (velocity of light), permittivity and permeability of vacuum will have the following values

$$\mu_0 = 4\pi \cdot 10^{-7} H/m,$$

$$\varepsilon_0 = \frac{1}{c_0^2 \mu_0^2} = 8.854 \cdot 10^{-12} F/m.$$

Here, P is the *electric polarization vector* which is represented as the volume density of *electric dipole moment*. So P describes how the material is polarized due to the presence of an electric field E. Polarization is directly proportional to the electric field for the linear materials. The equation is

$$\mathrm{P} = \varepsilon_0 \chi_e \mathrm{E}, \tag{2.9}$$

where, χ_e is the *electric susceptibility*.
Similarly, M is the *magnetization vector* which is represented as the volume density of *magnetic dipole moment*. So M describes how the material is magnetized due to the presence of a magnetic field H. At the same time, magnetization is directly proportional to the magnetic field for the linear materials. The equation is

$$\mathrm{M} = \mu_0 \chi_m \mathrm{H}, \tag{2.10}$$

where, χ_e is the *magnetic susceptibility*.
The constitutive equations for the linear materials becomes

$$\mathrm{D} = \varepsilon_0 \left(1 + \chi_e\right) \mathrm{E} = \varepsilon_0 \varepsilon_r \mathrm{E} = \varepsilon \mathrm{E}, \tag{2.11}$$

$$\mathrm{B} = \varepsilon_0 \left(1 + \chi_m\right) \mathrm{H} = \mu_0 \mu_r \mathrm{H} = \mu \mathrm{H}, \tag{2.12}$$

where,

$$\varepsilon_r = \left(1 + \chi_e\right), \tag{2.13}$$

$$\mu_r = \left(1 + \chi_m\right). \tag{2.14}$$

Generalized Constitutive Equations

There are some materials that have non-zero polarization and magnetization even if there is no electric field and no magnetic field present. The constitutive equations for non-linear materials can be derived for more general cases. The equation for the electric field becomes

$$\mathrm{D} = \varepsilon_0 \varepsilon_r \mathrm{E} + \mathrm{D}_r, \tag{2.15}$$

where, $\mathrm{D_r}$ is the *remanent electric flux density* which is the electric flux density even if no electric field is present.

The generalized equation for magnetic field for non-linear materials becomes

$$\mathrm{B} = \mu_0 \mu_r \mathrm{H} + \mathrm{B}_r, \tag{2.16}$$

where, $\mathrm{B_r}$ is the *remanent magnetic flux density* which is the magnetic flux density even if no magnetic field is present.
The current density can be generalized by adding an externally generated current J^e to the constitutive equation. The generalized relation becomes

$$\mathbf{J} = \sigma \mathrm{E} + J^e. \tag{2.17}$$

2.1.3 Wave Equation

The wave equation is main feature and governing equation in the propagation of EM waves. The derivation of the wave equation (electric) of the EM wave from Maxwell's equations has been shown.
Multiplying Equation 2.2 with ∇, we get,

$$\nabla \times (\nabla \times \mathrm{E}) = \nabla \times \left(-\frac{\partial \mathrm{B}}{\partial t} \right) = -\frac{\partial}{\partial t} (\nabla \times \mathrm{B}). \tag{2.18}$$

From Equation 2.1, 2.11 and 2.12, we get,

$$\nabla \times (\nabla \times \mathrm{E}) = -\mu \varepsilon \frac{\partial^2 \mathrm{E}}{\partial t^2}. \tag{2.19}$$

Considering $\frac{\partial}{\partial t}$ = $j\omega$, $\varepsilon = \varepsilon_0 \varepsilon_r$ and $\mu = \mu_0 \mu_r$, the equation becomes,

$$\nabla \times \left(\mu_r^{-1} \nabla \times \mathrm{E} \right) - k_0^2 \varepsilon_r \mathrm{E} = 0, \tag{2.20}$$

where, the wave number of free space be

$$k_0 = \omega \sqrt{\mu_0 \varepsilon_0} = \frac{\omega}{c_0}. \tag{2.21}$$

Using the relation $\varepsilon_r = n^2$ for the linear materials where n is the refractive index and assuming $\mu_r = 1$, the equation can be re-written as

$$\nabla \times (\nabla \times \mathrm{E}) - k_0^2 n^2 \mathrm{E} = 0. \tag{2.22}$$

2.2 Plasmonic Material Modelling

Metals like silver and gold are the most commonly used materials for designing plasmonic devices for their small ohmic loss i.e., high DC conductivity. The optical proper-

ties of these metals can be investigated by complex dielectric function i.e., permittivity and magnetic permeability. As the magnetic interaction of metals is not strong, permeability is considered as a unity. The complex dielectric function can be described in the following form:

$$\varepsilon_r(\omega) = \varepsilon_{r1}(\omega) - i\varepsilon_{r2}(\omega). \tag{2.23}$$

The real part of the permittivity is responsible for polarization property, and the imaginary part is for propagation loss. Complex Refractive index, $N = n - ik$, can be determined by the refractive index n and the extinction coefficient k. These are be described by the following equations:

$$n = \frac{1}{\sqrt{2}}\left[\left(\varepsilon_{r1}^2 + \varepsilon_{r2}^2\right)^{1/2} + \varepsilon_{r1}\right]^{1/2}, \tag{2.24}$$

$$k = \frac{1}{\sqrt{2}}\left[\left(\varepsilon_{r1}^2 + \varepsilon_{r2}^2\right)^{1/2} - \varepsilon_{r1}\right]^{1/2}. \tag{2.25}$$

2.2.1 Drude and Drude-Lorentz Model

Drude and Drude-Lorentz Model for metals are commonly used for modeling of metals. The optical properties like permittivity can be represented using the model equations. Drude-Lorentz model separates free-electron effects and bound-electron effects on complex dielectric function [74], [78]. The part on which free-electron effects act $\epsilon_r^{(f)}(\omega)$, can be expressed by the Drude model in the following form:

$$\varepsilon_r^{(f)}(\omega) = 1 - \frac{\Omega_p^2}{\omega\left(\omega - i\Gamma_0\right)}, \tag{2.26}$$

and the part on which bound-electron effects act $\epsilon_r^{(b)}(\omega)$, can be described by the Lorentz model in the following form:

$$\varepsilon_r^{(b)}(\omega) = \sum_{n=1}^{k} \frac{f_n\omega_p^2}{(\omega_n^2 - \omega^2) + i\omega\Gamma_n}, \tag{2.27}$$

where, ω_p refers to the plasma frequency, k refers to the number of oscillation with resonance frequency ω_n, dominant frequency f_n, damping frequency Γ_n and $1/\Gamma_n$ is the lifetime. Here $\Omega_p = \sqrt{f_0\omega_p}$ refers to the plasma frequency of the free-electron model having damping constant Γ_0 and oscillator strength f_0. Finally, the complex dielectric function can be described in the following form:

$$\varepsilon_r(\omega) = \varepsilon_r^{(f)}(\omega) + \varepsilon_r^{(b)}(\omega). \tag{2.28}$$

2.2.2 Modelling of Silver

The silver metal needs to be modeled for the simulation purpose. The equations related to the modeling has been discussed in the previous section. Table 2.1 represents the

Table 2.1: Drude and Drude-Lorentz model Parameters for silver metal.

Parameters	**Values (eV)**
Plasma frequency ($\hbar\omega_p$)	9.01
Damping constant (Γ_0)	0.048
Oscillator strength (f_0)	0.845
Dominant frequency (f_n)	[0.065; 0.011; 0.840; 5.646]
Damping frequency (Γ_n)	[3.886; 0.452; 0.065; 0.916; 2.419]
Resonance frequency (ω_n)	[0.816; 4.481; 8.185; 9.083; 20.29]
Number of resonance	6

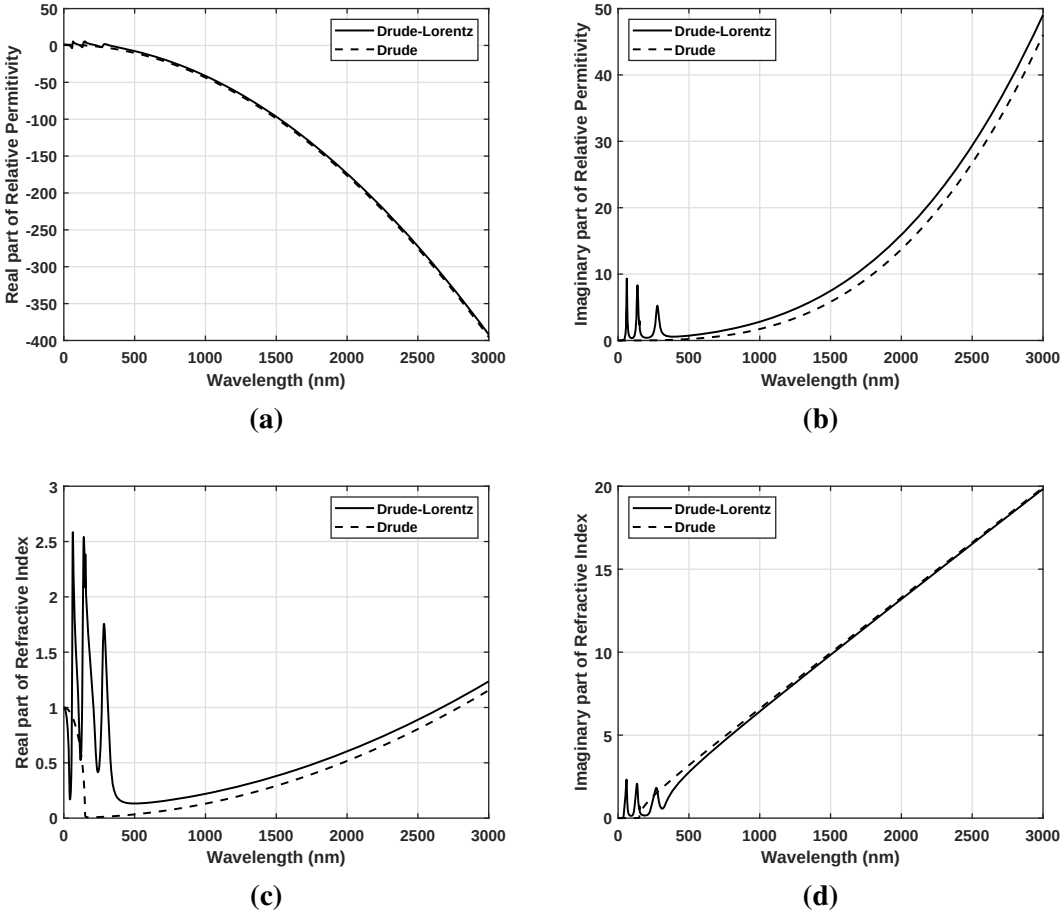

Figure 2.1: Relative permittivity and refractive index of silver Ag with the change of wavelength. (a) Real part of relative permittivity, (b) Imaginary part of relative permittivity, (c) Real part of refractive index, and (d) Imaginary part of refractive index.

numerical values to calculate complex dielectric function i.e relative permittivity from Equation 2.28. These numerical values have been taken from Rakic *et. al.* [78]. Complex refractive index can also be calculated using Equation 2.24 and 2.25. The real part and imaginary part of the relative permittivity and refractive index have been depicted in Fig. 2.1 respectively. From Fig. 2.1, it can be shown that the real part of the permittivity is negative for silver, which is an important parameter for SPP to propagate, and the imaginary part is responsible for propagation loss.

2.2.3 Modelling of Gold

In similar way of the silver, gold can be modelled using Equation 2.28, 2.24 and 2.25. The numerical values of the variables for the gold has also been taken from rakic *et. al.* [78] shown in Table 2.2.

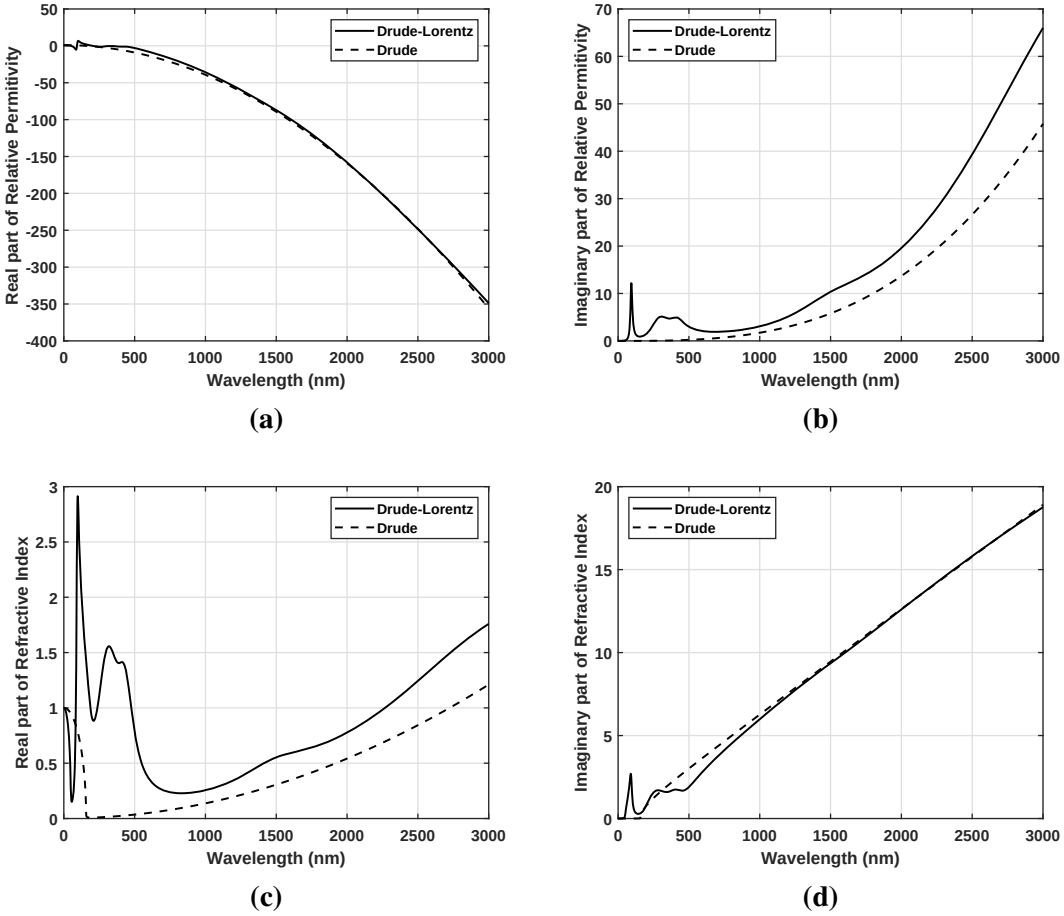

Figure 2.2: Relative permittivity and refractive index of gold Au with the change of wavelength. (a) Real part of relative permittivity, (b) Imaginary part of relative permittivity, (c) Real part of refractive index, and (d) Imaginary part of refractive index.

Table 2.2: Drude and Drude-Lorentz model Parameters for gold.

Parameters	**Value (eV)**
Plasma frequency ($\hbar\omega_p$)	9.03
Damping constant (Γ_0)	0.053
Oscillator strength (f_0)	0.760
Dominant frequency (f_n)	[0.024; 0.010; 0.071; 0.601; 4.384]
Damping frequency (Γ_n)	[0.241; 0.345; 0.870; 2.494; 2.214]
Resonance frequency (ω_n)	[0.415; 0.830; 2.969; 4.304; 13.32]
Number of resonance	6

The real part and imaginary part of the relative permittivity and the complex refractive index have been depicted in Fig. 2.2 for gold. It also shows negative permittivity for the real part and positive for the imaginary part. In this thesis, silver has been placed in MIM configuration as metal.

2.3 Boundary Condition

Scattering boundary conditions can be applied for the purpose of making the boundary transparent. This boundary condition is transparent for incoming incident waves also. The outgoing scattered wave for which the boundary is perfectly transparent (for plane scattered wave) be

$$E = E_{sc}e^{-jk(n\cdot r)} + E_0 e^{-jk(\mathrm{K}\cdot r)}. \tag{2.29}$$

The boundary is perfectly transparent for the scattered plane wave, which is at the normal incident to the boundary. The oblique incident plane wave is partially reflected from the boundary.

2.4 Finite Element Method

Problems that have complex geometry and inhomogeneous media can be handled by finite element method (FEM) more accurately and efficiently than other conceptually simpler and easier to code mathematical techniques like finite difference method, method of moments (MOM), etc. General code can be developed with FEM for a specific discipline, which can be applied to another field with some or no modification [79].

Four steps can be followed for the FEM analysis of any problem [80]:

- Discretization of the solution region into a finite number of elements,
- Formulation of governing equation for an element,

- Putting together all elements in the region,
- Solving the obtained equations of the problem.

A regular wave equation can be expressed as

$$\nabla^2\Phi + k^2\Phi = g, \tag{2.30}$$

where, Φ is the field quantity to be determined, g is the source, and k is the wavenumber of the medium. It is assumed that $k = g = 0$ for simplification of the calculation of an example with FEM, which implies the Laplace's equation. The Laplace's equation has been considered as $\nabla^2 V = 0$ for the purpose of illustration of FEM.

2.4.1 Discretization

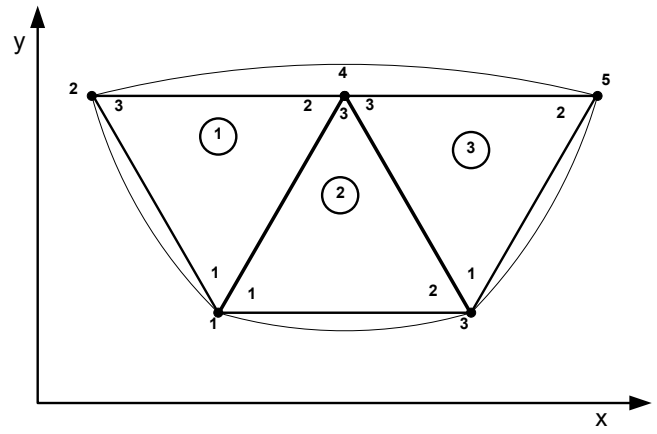

Figure 2.3: Solution region with its finite element discretization (assembly of three triangular element).

A very simple 2D region has been taken to illustrate the steps of FEM. The arbitrarily shaped curve in Figure 2.3 shows the solution region. The region has been divided into three triangular elements, which are referred to as finite element discretization. The approximate solution of the region can be expressed as

$$V(x, y) \approx \sum_{e=1}^{N} V_e(x, y), \tag{2.31}$$

where, N (=3) is the number of finite elements.

V_e can be represented by polynomial function for the case of triangular element as follows

$$V_e(x, y) = a + bx + cy, \tag{2.32}$$

where, a, b, c are constants to be determined. If a, b, c are known, it is possible to find V_e at any point within the element. It is assumed to have a linear variation of potential

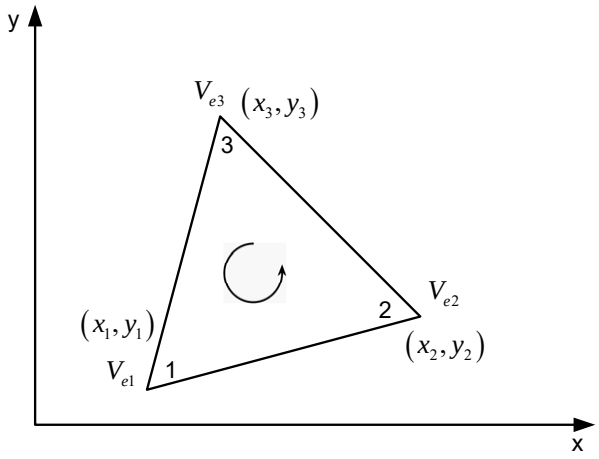

Figure 2.4: Single triangular element having local node 1-2-3 counterclockwise.

within the element as in Equation 2.32; electric field will also be uniform within the element

$$E_e = -\nabla V_e. \tag{2.33}$$

2.4.2 Governing Equations

A single triangular element has been taken which is shown in Figure 2.4. Potentials at different nodes can be expressed by the following matrix

$$[V_e] = \begin{bmatrix} V_{e1} \\ V_{e2} \\ V_{e3} \end{bmatrix} = \begin{bmatrix} 1 & x_1 & y_1 \\ 1 & x_2 & y_2 \\ 1 & x_3 & y_3 \end{bmatrix} \begin{bmatrix} a \\ b \\ c \end{bmatrix}. \tag{2.34}$$

The constants a, b, c can be determined from Equation 2.34 as

$$\begin{bmatrix} a \\ b \\ c \end{bmatrix} = \begin{bmatrix} 1 & x_1 & y_1 \\ 1 & x_2 & y_2 \\ 1 & x_3 & y_3 \end{bmatrix}^{-1} \begin{bmatrix} V_{e1} \\ V_{e2} \\ V_{e3} \end{bmatrix}. \tag{2.35}$$

Putting this into Equation 2.32, we get

$$V_e = \sum_{i=1}^{3} \alpha_i (x, y) V_{ei}, \tag{2.36}$$

where,

$$\alpha_1 = \frac{1}{2A}[(x_2 y_3 - x_3 y_2) + (y_2 - y_3)x + (x_3 - x_2)y],$$

$$\alpha_2 = \frac{1}{2A}[(x_3 y_1 - x_1 y_3) + (y_3 - y_1)x + (x_1 - x_3)y],$$

$$\alpha_3 = \frac{1}{2A}[(x_1y_2 - x_2y_1) + (y_1 - y_2)x + (x_2 - x_1)y],$$

$$A = \frac{1}{2}[(x_2 - x_1)(y_3 - y_1) - (x_3 - x_1)(y_2 - y_1)],$$

A is the area of the element e, and its value is positive for counterclockwise numbering, α is called the element shape function. It is to mention that Equation 2.36 can estimate potential at any point in the element provided that potential at the vertices are known. The energy per unit length associated with the element e corresponding to the Laplace equation is

$$W_e = \frac{1}{2}\int \varepsilon \left|E_e\right|^2 dS = \frac{1}{2}\int \varepsilon \left|\nabla V_e\right|^2 dS. \tag{2.37}$$

From Equation 2.36,

$$\nabla V_e = \sum_{i=1}^{3} V_{ei} \nabla \alpha_i. \tag{2.38}$$

Putting Equation 2.38 into Equation 2.38 and expressing the equation in matrix form gives

$$W_e = \frac{1}{2}\varepsilon [V_e]^t \left[C^{(e)}\right] [V_e,] \tag{2.39}$$

where, subscript t stands for the transpose of the matrix V_e and

$$C_{ij}^{(e)} = \int \nabla \alpha_i \cdot \nabla \alpha_j dS, \tag{2.40}$$

$$\left[C^{(e)}\right] = \begin{bmatrix} C_{11}^{(e)} & C_{12}^{(e)} & C_{13}^{(e)} \\ C_{21}^{(e)} & C_{22}^{(e)} & C_{23}^{(e)} \\ C_{31}^{(e)} & C_{32}^{(e)} & C_{33}^{(e)} \end{bmatrix}, \tag{2.41}$$

$[C^{(e)}]$ is the *element coefficient matrix*.

2.4.3 Assembling All the Elements

From a single element to N number of elements can be assembled for getting the solution of the whole region. The energy associate with the assemblage elements can be expressed as

$$W = \sum_{e=1}^{N} W_e = \frac{1}{2}\varepsilon [V]^t [C] [V], \tag{2.42}$$

where,

$$[V] = \begin{bmatrix} V_1 \\ V_2 \\ V_3 \\ \vdots \\ V_n \end{bmatrix}, \tag{2.43}$$

n is the total number of nodes, N is the number of elements and $[C]$ is the *global coefficient matrix* which consists of the element coefficient matrices.

The process of building a global coefficient matrix from individual coefficient matrices can be illustrated taking Figure 2.3 into consideration. The global numbering for the global nodes is 1, 2, 3, 4, and 5. The local numbering inside each of the three elements is 1-2-3, and the numbering is done in counterclockwise order inside each of them. The three individual matrices are numbered as 1,2 and 3 inside a small circle. So there are two types of numbering. The global coefficient matrix can be expressed by each of these numbering systems. If global numbering is taken into consideration, the global coefficient matrix will be a 5x5 matrix, expressed as

$$[C] = \begin{bmatrix} C_{11} & C_{12} & C_{13} & C_{14} & C_{15} \\ C_{21} & C_{22} & C_{23} & C_{24} & C_{25} \\ C_{31} & C_{32} & C_{33} & C_{34} & C_{35} \\ C_{41} & C_{42} & C_{43} & C_{44} & C_{45} \\ C_{51} & C_{52} & C_{53} & C_{54} & C_{55} \end{bmatrix}. \tag{2.44}$$

Here C_{ij} is due to the coupling between nodes i and j. The potential at the inter-element boundary of the elements must be identical. So C_{ij} will contain a contribution from the elements associated with the nodes i and j. Like, in Figure 2.3, elements 2 and 3 have global node 3 in common, so

$$C_{33} = C_{22}^{(2)} + C_{11}^{(3)}.$$

Node 5 is associated only with element 3, hence

$$C_{55} = C_{22}^{(3)}.$$

If there is no direct association between nodes, the global coefficient will be zero. It is to note that the global coefficient matrix is symmetric

$$C_{ij} = C_{ji}.$$

Considering all these, the global coefficient matrix expressed in terms of element coefficient matrix has been shown below-

$$[C] = \begin{bmatrix} C_{11}^{(1)} + C_{11}^{(2)} & C_{13}^{(1)} & C_{12}^{(2)} & C_{12}^{(1)} + C_{13}^{(2)} & 0 \\ C_{31}^{(1)} & C_{33}^{(1)} & 0 & C_{32}^{(1)} & 0 \\ C_{21}^{(2)} & 0 & C_{22}^{(2)} + C_{11}^{(3)} & C_{23}^{(2)} + C_{13}^{(3)} & C_{12}^{(3)} \\ C_{21}^{(1)} + C_{31}^{(2)} & C_{23}^{(1)} & C_{32}^{(2)} + C_{31}^{(3)} & C_{22}^{(1)} + C_{33}^{(2)} + C_{33}^{(3)} & C_{32}^{(3)} \\ 0 & 0 & C_{21}^{(3)} & C_{23}^{(3)} & C_{22}^{(3)} \end{bmatrix}. \quad (2.45)$$

2.4.4 Solving the Equations

Laplace's equation will be satisfied if the total energy in the solution region be minimum. Hence the partial differentiation with respect to each nodal value will be zero. Thus,

$$\frac{\partial W}{\partial V_k} = 0, \quad k = 1, 2, \ldots, n \ . \quad (2.46)$$

From Equation 2.42 and Equation 2.44 and taking partial derivative of W with respect to V_1,

$$\frac{\partial W}{\partial V_1} = 0 = V_1 C_{11} + V_2 C_{12} + V_3 C_{13} + V_4 C_{14} + V_5 C_{15}. \quad (2.47)$$

In general, the equation can be written as

$$\frac{\partial W}{\partial V_k} = 0 = \sum_{i=1}^{n} V_i C_{ik}. \quad (2.48)$$

Assuming the node 1 as free node, from Equation 2.47, it can be derived as

$$V_1 = -\frac{1}{C_{11}} \sum_{i=2}^{5} V_i C_{1i}. \quad (2.49)$$

From the above equation, it can be generalized as

$$V_k = -\frac{1}{C_{kk}} \sum_{i=1, i \neq k}^{n} V_i C_{ki}. \quad (2.50)$$

where node k is a free node. If node k is not connected with node i, C_{ki} will be zero. Only the nodes that are directly linked with node k contributes to V_k. The initial values of the potentials at different nodes are of two types. The known are kept as before, and the unknown is set to zero or averaging the known potentials [81]. Taking the initial values, all free node values are calculated. Thus the first iteration completes. In the second iteration, these values become the previous value. New values of potentials at

different nodes are calculated. This procedure is repeated until there is a negligible difference of potential at nodes between two iterations.

2.5 S-Parameter and Transmittance

Scattering parameters (S-parameters) are frequency-dependent, complex-valued matrices representing the reflection and transmission of EM energy measured at different ports of a particular device like sensors, filters, antennas, transmission lines, etc. Originally transmitted and reflected voltage waves of transmission lines were described in terms of S-parameters. Here all ports are assumed to be connected to matched loads. Voltage is not a well-defined term for high-frequency problems. In order to express S-parameters, the electric field can be a good solution. Electric field pattern on a port has to be represented as scalar complex-valued number corresponding to transmission line theory. An eigenmode expansion of the EM fields to be performed on the ports. Assuming that after performing eigenmode analysis on the ports 1, 2, 3, ..., here E_1, E_2, E_3, ... are the electric field patterns of the fundamental modes on these ports. It is assumed that electric field patterns are normalized with respect to the integral power flow across each port cross-section respectively. Unless it is TEM mode, normalization is frequency-dependent. The port excitation is applied by fundamental eigenmode. The computed electric field at the port comprises of excited field and the reflected field. The port boundary where there is excitation, the computed field can be represented as

$$\mathrm{E}_c = \mathrm{E}_1 + \sum_{i=1} S_{i1}\mathrm{E}_i. \tag{2.51}$$

On all other ports where there is no excitation can be represented as

$$\mathrm{E}_c = \sum_{i=1} S_{i1}\mathrm{E}_i. \tag{2.52}$$

The S-parameters are given by

$$S_{11} = \frac{\int_{port\_1} ((\mathrm{E}_c - \mathrm{E}_1) \cdot \mathrm{E}_1^*)\, dA_1}{\int_{port\_1} (\mathrm{E}_1 \cdot \mathrm{E}_1^*)\, dA_1}, \tag{2.53}$$

$$S_{21} = \frac{\int_{port\_2} (\mathrm{E}_c \cdot \mathrm{E}_2^*)\, dA_2}{\int_{port\_2} (\mathrm{E}_2 \cdot \mathrm{E}_2^*)\, dA_2}, \tag{2.54}$$

$$S_{31} = \frac{\int_{port\_3} (\mathrm{E}_c \cdot \mathrm{E}_3^*)\, dA_3}{\int_{port\_3} (\mathrm{E}_3 \cdot \mathrm{E}_3^*)\, dA_3}, \tag{2.55}$$

and so on.

The S-parameters for a device with n ports are

$$S = \begin{bmatrix} S_{11} & S_{12} & \cdots & S_{1n} \\ S_{21} & S_{22} & \cdots & S_{2n} \\ \vdots & \vdots & \cdots & \vdots \\ S_{n1} & S_{n2} & \cdots & S_{nn} \end{bmatrix}. \tag{2.56}$$

Transmittance or reflectance (time average power transmission/reflection coefficient) can be obtained by

$$T = |S_{ij}|^2. \tag{2.57}$$

S-parameters for the 2-port system have the following descriptions:
S_{11} is the input port voltage reflection coefficient,
S_{21} is the voltage transmission coefficient from port 1 to port 2 ,
S_{12} is the reverse voltage gain,
S_{22} is the output port voltage reflection coefficient.

S-parameters are also expressed in dB in the following manner

$$S_{ijdB} = 20 \log 10 \left(|S_{ij}| \right). \tag{2.58}$$

2.6 Port and Mode Analysis

The ports are the boundary conditions for denoting the input and output sides generally. Previously discussed S-parameter calculations involve the port boundary condition. The fields E_1, E_2, E_3, etc. should be normalized such that they represent the same power flow through the respective ports. The power flow is given by the time average Poynting vector,

$$S_{av} = \frac{1}{2} \mathrm{Re} \left(\mathrm{E} \times \mathrm{H}^* \right). \tag{2.59}$$

The normal component of the Poynting vector is the amount of power flowing out of a port,

$$n \cdot S_{av} = n \cdot \frac{1}{2} \mathrm{Re} \left(\mathrm{E} \times \mathrm{H}^* \right). \tag{2.60}$$

It is not possible to normalize the field with respect to the power flow below the cut-off frequency; the power flow is zero. In this region, the S-parameters are trivial and do not need to be calculated.

For TE waves

$$\mathrm{E} = -Z_{TE}\left(n \times \mathrm{H}\right), \tag{2.61}$$

where, Z_{TE} is the wave impedance

$$Z_{TE} = \frac{\omega\mu}{\beta}, \tag{2.62}$$

ω is the angular frequency of the wave, μ the permeability and β the propagation constant. The power flow then becomes

$$n \cdot S_{av} = n \cdot \frac{1}{2}\mathrm{Re}\left(\mathrm{E} \times \mathrm{H}^{*}\right) = -\frac{1}{2}\mathrm{Re}\left(\mathrm{E} \cdot \left(n \times \mathrm{H}^{*}\right)\right) = \frac{1}{2Z_{TE}}|E|^{2}. \tag{2.63}$$

For TM waves

$$\mathrm{H} = -Z_{TM}\left(n \times \mathrm{E}\right), \tag{2.64}$$

where, Z_{TM} is the wave impedance

$$Z_{TM} = \frac{\beta}{\omega\varepsilon}, \tag{2.65}$$

where, ε is the permittivity. The power flow then becomes

$$n \cdot S_{av} = n \cdot \frac{1}{2}\mathrm{Re}\left(\mathrm{E} \times \mathrm{H}^{*}\right) = \frac{1}{2Z_{TM}}\left(n \cdot \mathrm{Re}\left(\mathrm{E} \times \left(n \times \mathrm{E}^{*}\right)\right)\right) = \frac{1}{2Z_{TM}}|n \cdot E|^{2}. \tag{2.66}$$

Mode Analysis

It requires boundary mode analysis for the type of excitation in the port. This analysis finds the lowest fundamental mode that supports propagation in the waveguide and also solves for the propagation constant. The time-harmonic representation of the fields includes a complex parameter in the phase,

$$\mathrm{E}\left(r, t\right) = \mathrm{Re}\left(\widetilde{\mathrm{E}}\left(r\right)e^{j\omega t - \alpha z}\right). \tag{2.67}$$

The spatial parameter, $\alpha = \delta_z + j\beta = -\lambda$, can have a real part or imaginary part. The imaginary part, β, represents propagation constant and the real part, δ_z, represents the damping along the propagation direction.

Chapter 3

Performance Parameters of an RI Sensor

The ring resonator is one of the original designs of the refractive index sensors. The theoretical investigation of the ring resonator will help the understanding of the simulation results, where he resonant wavelength and transmittance of the ring resonator are the key parameters to investigate. The performance parameters of a refractive index sensor determine how well is the design of the sensor. The sensitivity, figure of merit, and resolution are the performance parameters of a refractive index sensor. Re-simulating, any well-established sensor from the literature, can validate the simulation environment. The performance parameters obtained from the re-simulation can be compared with the original result to get a sense of how well is the simulation environment.

3.1 Ring Resonator

The basic structure of a ring resonator with a radius R and a straight waveguide has been described in Fig.3.1, which is of unidirectional-type coupling. The relation between input and output of the straight and ring resonator can be described by the matrix relation [82],

$$\begin{bmatrix} E_{t1} \\ E_{t2} \end{bmatrix} = \begin{bmatrix} t & \kappa \\ -\kappa^* & t^* \end{bmatrix} \begin{bmatrix} E_{i1} \\ E_{i2} \end{bmatrix}. \tag{3.1}$$

Here, E_{i1} is the source complex mode amplitude at the input port, E_{t1} is the transmission complex mode amplitude at the output port, E_{t2} is the coupled complex mode amplitude to the ring, E_{t1} is the complex mode amplitude transmitted from the ring, and the coupling parameters κ and t depend on the coupling mechanism, and $*$ denotes the complex conjugate of the respective terms. It has been considered that the coupling is lossless; single polarized; none of the segments of the waveguide and elements of coupler couple waves of different polarization, attenuation constant contains different losses occurs during the propagation of waves in the resonator. As the networks are

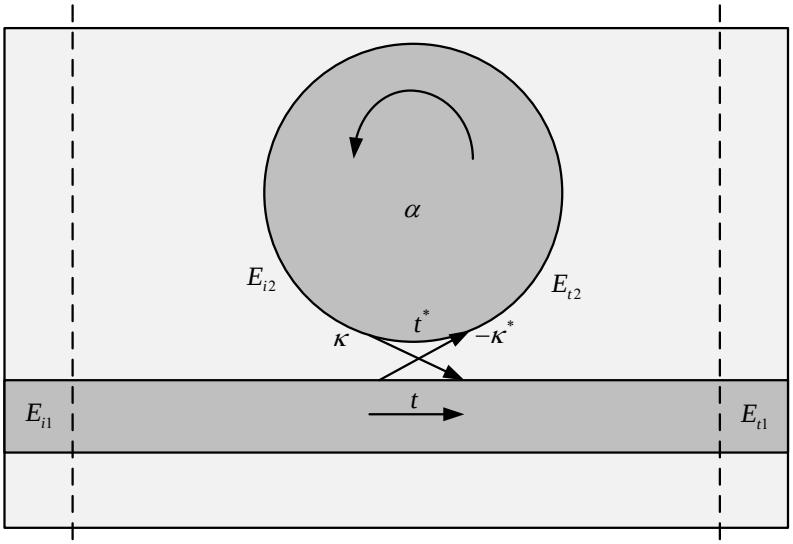

Figure 3.1: Structure of plasmonic waveguide side coupled with ring resonator.

reciprocal, the matrix is symmetric which gives

$$\left|\kappa^2\right| + \left|t^2\right| = 1. \tag{3.2}$$

E_{i1} can be considered as 1 for the purpose of simplification which implies the round trip in the ring being,

$$E_{i2} = \alpha \cdot e^{j\theta} E_{t2}, \tag{3.3}$$

where, α is the coefficient of loss of the ring, i.e. if α =1, no loss. Here θ can be expressed in the following form,

$$\theta = \frac{\omega L}{c} = \frac{2\pi c_0 L}{\lambda c} = k \cdot n_{eff} \cdot L = \beta \cdot L, \tag{3.4}$$

where, c be the phase velocity of the ring resonator given by $c = c_0/n_{eff}$, n_{eff} is the effective refractive index, L is the circumference of the ring given by $L = 2\pi r$, r is the radius of the ring measured from the center of the ring to the center of the waveguide. The vacuum wavenumber can be expressed in terms of the wavelength λ as $k = 2\pi/\lambda$. It can be written from (3.4), $\beta = k \cdot n_{eff}$.

From the matrix equations (3.1) and (3.3), the three terms E_{t2}, E_{t1}, and E_{i2} can be expressed in the following form,

$$E_{t2} = -\kappa^* + t^* \left(\alpha e^{j\theta} E_{t2}\right),$$

$$E_{t2}\left(1 - t^* \alpha e^{j\theta}\right) = -\kappa^*,$$

$$E_{t2} = \frac{-\kappa^*}{1 - \alpha t^* e^{j\theta}}, \tag{3.5}$$

$$E_{t1} = \frac{-\alpha + te^{-j\theta}}{-\alpha t^* + e^{-j\theta}}, \tag{3.6}$$

$$E_{i2} = \frac{-\alpha\kappa^*}{-\alpha t^* + e^{-j\theta}}. \tag{3.7}$$

The square of the complex mode amplitude E is the modal power. The transmission power of the waveguide P_{t1} and the circulating power in the ring P_{i2} can be described on resonance in the following form, having $\theta + \varphi_t = 2\pi m$ on resonance where $t = |t|\, e^{j\varphi_t}$ is the coupling loss, φ_t is the phase of the coupling, and m is an integer,

$$P_{t1} = |E_{t1}|^2 = \frac{\alpha^2 + |t|^2 - 2\alpha\,|t| \cos(\theta + \varphi_t)}{1 + \alpha^2|t|^2 - 2\alpha\,|t| \cos(\theta + \varphi_t)} = \frac{(\alpha - |t|)^2}{(1 - \alpha\,|t|)^2}, \tag{3.8}$$

$$P_{i2} = |E_{i2}|^2 = \frac{\alpha^2\left(1 - |t|^2\right)}{(1 - \alpha\,|t|)^2}. \tag{3.9}$$

On resonance $\theta = 2\pi m - \varphi_t$ and from (3.4), resonant wavelength λ_m can be derived as,

$$\frac{2\pi}{\lambda_m} \cdot n_{eff} \cdot L = 2\pi\left(m - \frac{\varphi_t}{2\pi}\right), \tag{3.10}$$

$$\lambda_m = \frac{n_{eff} \cdot L}{m - (\varphi_t/2\pi)}. \tag{3.11}$$

The value of the n_{eff} depends on the structure of the waveguide and the materials used in the design. The straight waveguide with width W is presented in Fig. 3.2. From port A, SPP has been excited in transverse magnetic (TM) mode where the incident light wavelength is higher than the width of the straight waveguide. The TM mode dispersion equation of this case can be described by [38],

$$\varepsilon_d\sqrt{n_{eff}^2 - \varepsilon_m} + \varepsilon_m\sqrt{n_{eff}^2 - \varepsilon_d}\tanh\left(\frac{W\pi\sqrt{n_{eff}^2 - \varepsilon_d}}{\lambda}\right) = 0, \tag{3.12}$$

where, ε_d is the permittivity of the dielectric, ε_m is the permittivity of the metal, n_{eff} is the effective refractive index, W is the width of the straight waveguide and λ is the wavelength of the incident light. From (2.28), we get the frequency-dependent ε_m and ε_d can be defined by $\varepsilon_d = n^2$ where n is the refractive index of the dielectric. The real part of n_{eff} for different values of n of the dielectric has been shown for a wavelength range of 800 nm to 3000 nm in Fig. 3.3. The waveguide design with the width

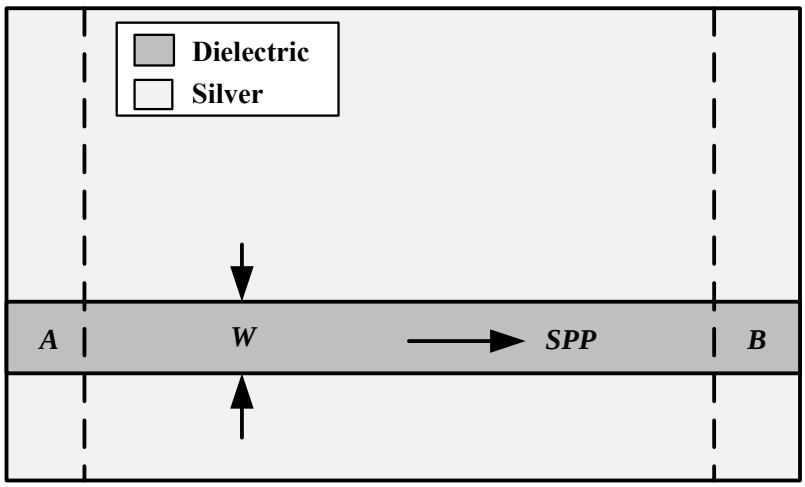

Figure 3.2: Basic structure of straight plasmonic waveguide with W = 140 nm.

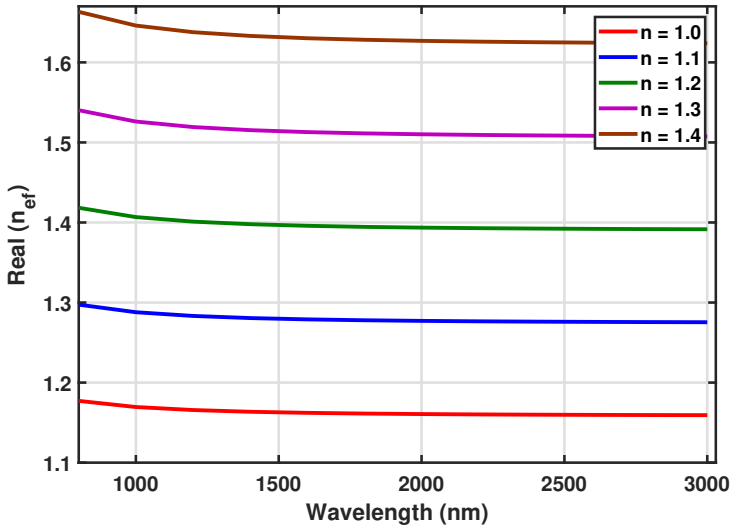

Figure 3.3: Real part of effective refractive index with change of wavelength for different values of n in the straight waveguide.

W larger than 20 nm can be fabricated with the fabrication technique of focused-ion-beam milling, electron-beam lithography, template stripping [83]–[86].

If it is considered that the power at port A is taken as P_{in} and port B as P_{tr} fot the structure shown in Fig. 3.2 , the transmittance of the device can be defined as

$$T = \frac{P_{tr}}{P_{in}}. \tag{3.13}$$

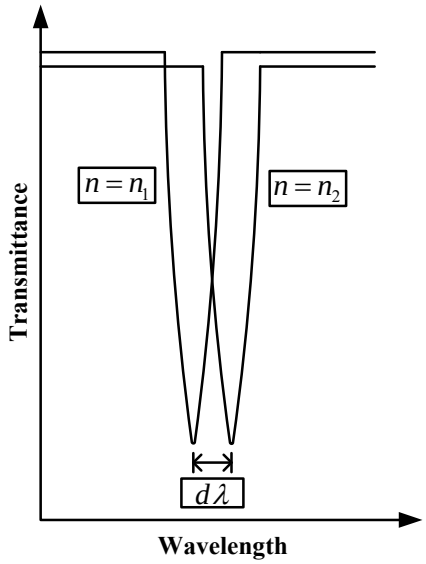

Figure 3.4: Transmittance versus wavelength plot for the calculation of sensitivity.

3.2 Parameters of Sensor Quality

Sensitivity and Figure of Merit (FOM) are the key measures for the quality of a plasmonic RI sensor [39]. The focus of the researchers is to make improvements to these parameters by designing different waveguide configurations within a small area.

3.2.1 Sensitivity

Ring and Cavity resonators are most commonly designed to get a frequency spectrum like Lorentzian, Notch-type, and Fano-resonance type, which have resonant frequencies [10]. Usually, the component whose refractive index has to be detected is placed in the cavity. If there is any change in the refractive index of the component placed in the cavity, the resonant wavelength shifts to the left or right. Sensitivity is the ratio of change in resonant wavelength and change in the refractive index.
The transmittance versus wavelength plot has been depicted for an example in Fig. 3.4. The transmittance is representing a notch-type response for different values of refractive index n. Here, $d\lambda$ represents the shift of the notch-type response i.e. resonant wavelength towards right for the change of refractive index from $n = n_1$ to $n = n_2$. The sensitivity, S, is determined by the shift of resonance wavelength, $d\lambda$, due to the change in refractive index $dn(= n_2 - n_1)$, can be expressed by the equation

$$S = \frac{d\lambda}{dn}. \tag{3.14}$$

The higher the value of the sensitivity, the better is the sensor. The design parameters are to be chosen, such that there will be a maximum shift of the resonant wavelength

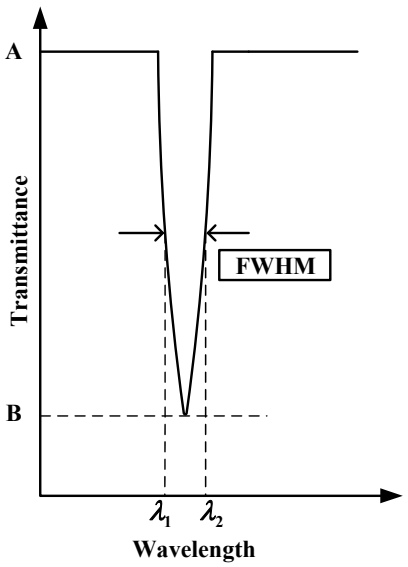

Figure 3.5: Transmittance versus wavelength plot for the calculation of FWHM.

of the transmittance of the sensor.

3.2.2 Figure of Merit (FOM)

It is easier to detect a resonance shift for the narrow linewidth of the spectrum. The full width at half maximum (FWHM) is the measure of how narrow the spectrum is. The transmittance versus wavelength plot has been depicted in Fig. 3.5 to show the calculation of FWHM. In Fig. 3.5, **A** and **B** are the maximum and minimum value points of the transmittance respectively. FWHM will be at $\frac{A+B}{2}$ and the corresponding values of the wavelength be λ_1 and λ_2. The FWHM can be calculated by the following equation

$$FWHM = \lambda_2 - \lambda_1. \tag{3.15}$$

The FOM can be calculated with the sensitivity and FWHM of the resonance spectrum [39], which is expressed by the equation

$$FOM = \frac{S}{FWHM}. \tag{3.16}$$

A better sensor will have the lower the value of FWHM and the higher value of sensitivity which can be ensured by the higher value of the FOM.

3.2.3 Resolution

Sensing resolution is the quantity by which the detection limit of the sensor can be determined i.e., how a small change in refractive index can the sensor detect. It can be defined as

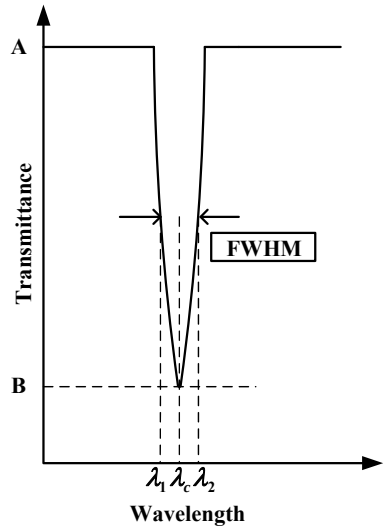

Figure 3.6: Transmittance versus wavelength plot for the calculation of quality factor.

$$SR = \frac{dn}{d\lambda}(\Delta\lambda), \tag{3.17}$$

where, $\Delta\lambda$ is the wavelength resolution, dn is the refractive index change and $d\lambda$ is the resonant wavelength shift for the change in n.

Another two parameters that can be kept into consideration are extinction ratio (ER), and resonant wavelength. The extinction ratio is the difference between the maximum and minimum value in the transmission response of the sensor. From Fig. 3.5, ER can be described as

$$ER = A - B. \tag{3.18}$$

The higher is the value of ER, the higher is the gap between the maximum and minimum points of the transmittance, the better is the detection. By the resonant frequency, estimation of the frequency range can be made to operate the sensor.

3.3 Parameter of Filter Quality

The quality of the filters is usually measured by the Quality Factor (QF). The QF is the ratio of the difference between frequencies at FWHM and the resonant frequency of transmittance. The resonant wavelength be λ_c in Fig. 3.6, and FWHM can be calculated from Equation 3.15 using λ_1, λ_2. The QF can be described by the following form,

$$QF = \frac{\lambda_c}{\lambda_2 - \lambda_1} = \frac{\lambda_c}{FWHM}. \tag{3.19}$$

The higher the value of QF is, the better is the device as filter.

3.4 Result Validation With COMSOL Multiphysics

Before moving onto the proposed design to simulate using COMSOL Multiphysics, one design has been taken from Xu *et. al.*, titled, "Refractive index sensing based on plasmonic waveguide side coupled with bilaterally located double cavities" published in *IEEE Transactions on Nanotechnology*. In that publication, analytic and simulation results have been published [41]. They utilized a 2D finite difference time domain (FDTD) method with a perfectly matched layer boundary condition for the purpose of simulation to get the transmittance of the design. The structure of the plasmonic waveguide side coupled with bilaterally located double cavities proposed in Xu *et. al.* has been depicted in Fig.3.7. There is a straight waveguide with width W_1, the gap between the straight waveguide and the cavities be g, and the length and width of the cavities be L and W_2 respectively. The transmission spectra of the design have been depicted from Xu *et. al.* in Fig. 3.8 with the design parameters chosen as g = 33 nm, W_1 = 40 nm, L = 360 nm, and W_2 = 80 nm.

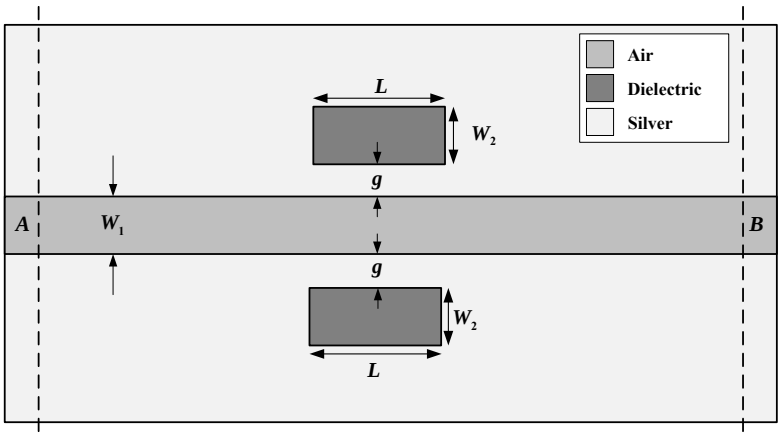

Figure 3.7: Structure of plasmonic waveguide side coupled with bilaterally located double cavities.

Using the same design parameter values, the 2D finite element method (FEM) with scattering boundary condition has been utilized to simulate and investigate the transmission spectra of the design with COMSOL Multiphysics, the detail outline of the methodology for the simulation in the COMSOL Multiphysics has been depicted in Fig. 3.9. First, the COMSOL Multiphysics setting for the space dimension is set to 2D, then the names and values of the different parameters like gap, length, width are set globally to be used in the whole process. After that, the main proposed design is built in COMSOL using the global parameters into account. After building the geometry, different materials are selected for the different domains according to the design of the device. The boundary conditions are then set, in this case, A and B with the dotted

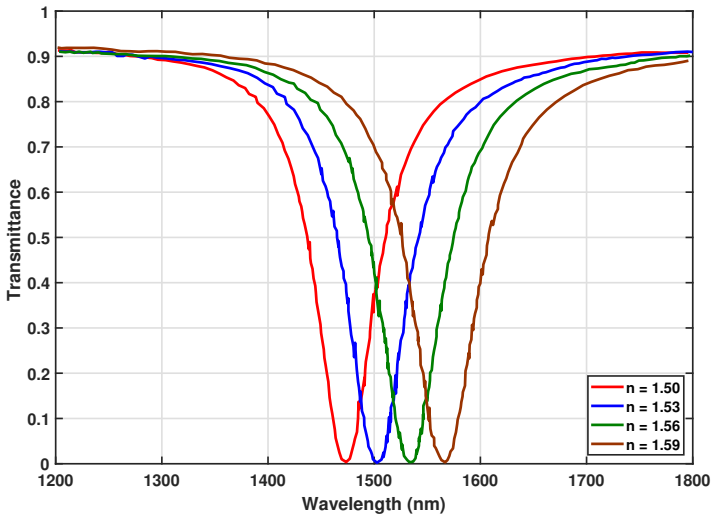

Figure 3.8: Transmittance versus wavelength with the data taken from Xu *et. al.*

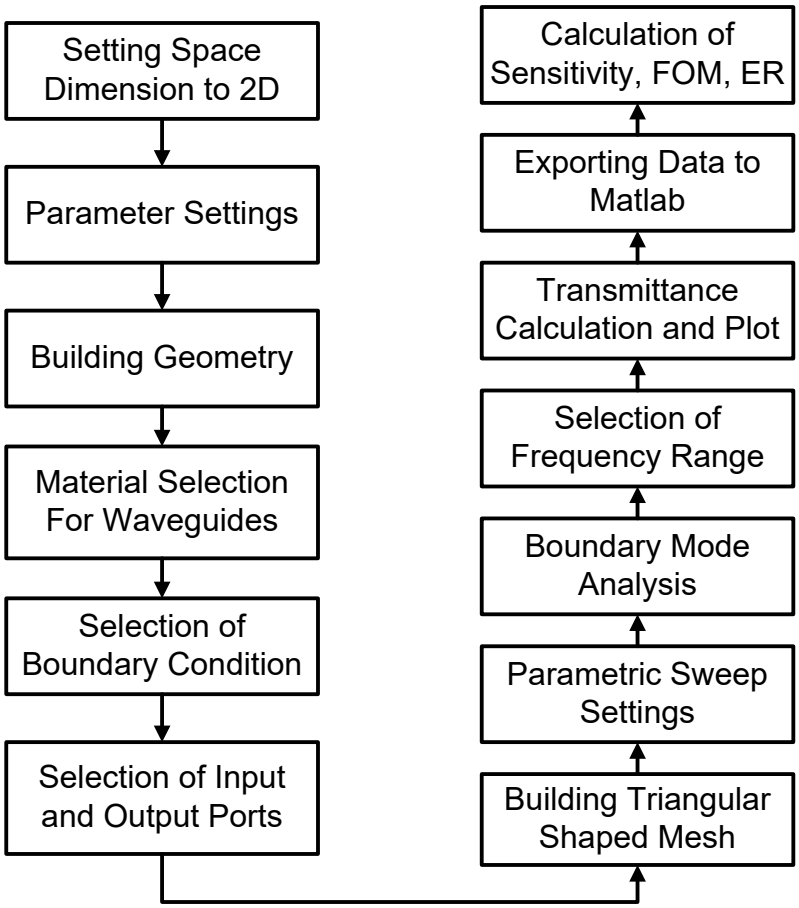

Figure 3.9: Outline of the methodology for the simulation in the COMSOL Multiphysics.

line has been selected as input and output port respectively, and the remaining side is set to scattering boundary conditions. Then, according to the geometry, the mesh has been built. In this case, a triangular-shaped mesh is selected to do the numerical

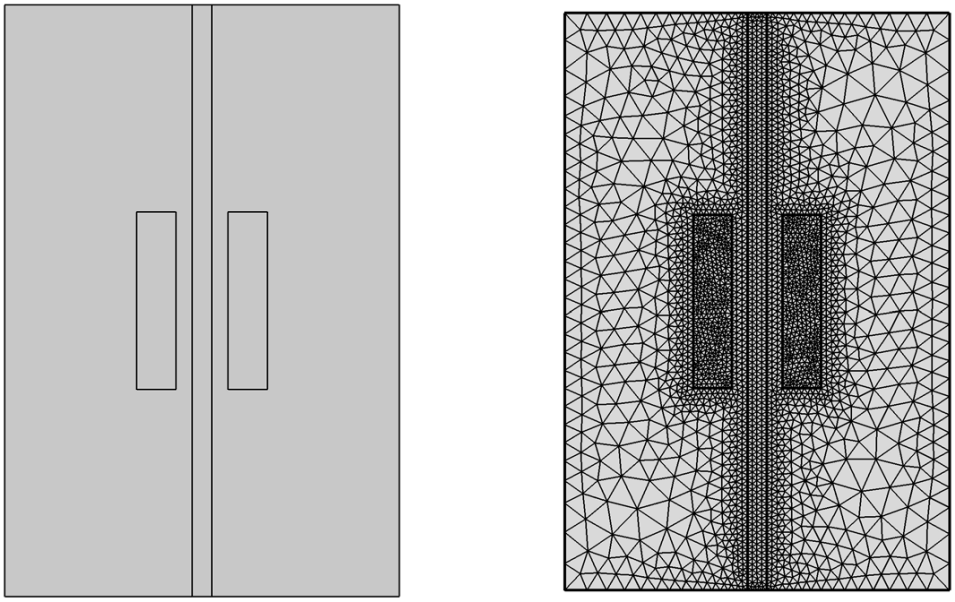

Figure 3.10: COMSOL Multiphysics view of the design and its mesh structure. (a) Geometric structure, (b) Mesh.

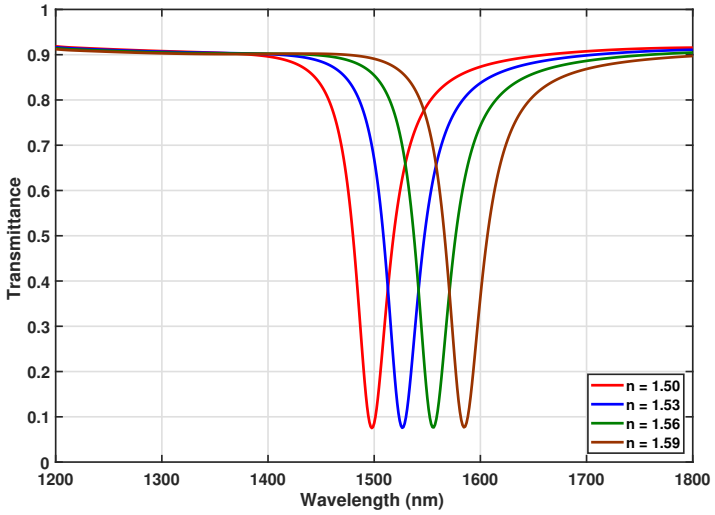

Figure 3.11: Transmittance versus wavelength re-simulated on COMSOL Multiphysics.

calculations. The analysis of the design can be done by using the parametric sweep of different parameters; for example, repetitive simulations with different values of the refractive index of the dielectric can be achieved easily by parametric sweep. Then during the simulation, boundary mode analysis is done by COMSOL Multiphysics to analyze the geometry and select the source and calculate the propagation constant. Based on these, the final simulation is done with the numerical calculation of the wave equation at different points of the design according to the mesh distribution. The calculation of the transmittance and the plot has been depicted using the data obtained

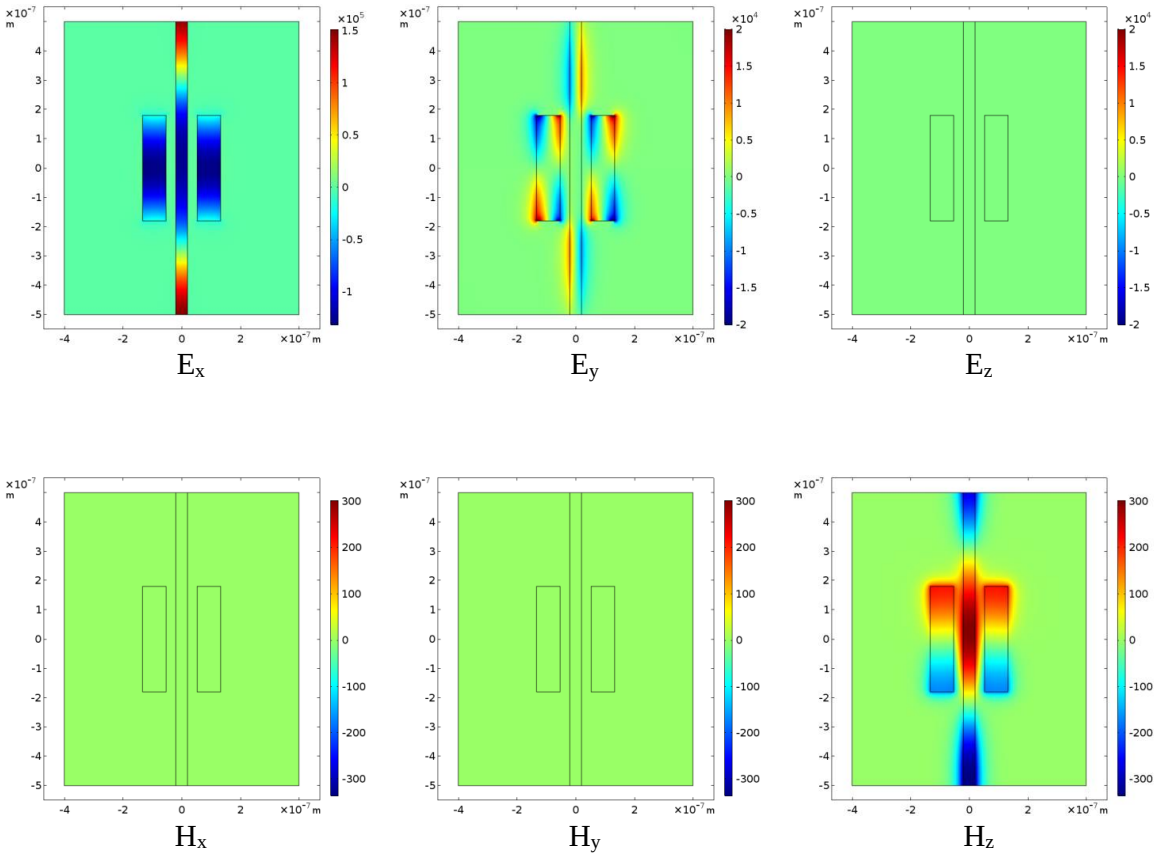

Figure 3.12: Electric and magnetic field components of the EM wave propagating in the device at the wavelength of 1500 nm with n = 1.53.

Table 3.1: Comparison of the results simulated on COMSOL Multiphysics with results from Xu *et. al.*.

Resonant Wavelength (nm) (Xu *et. al.*)	Resonant Wavelength (nm) (Simulated in COMSOL)	% of Difference (Resonant Wavelength)	Sensitivity (Xu *et. al.*)	Sensitivity (Simulated in COMSOL)	% of Difference (Sensitivity)
1473.60	1497.75	1.61	-	-	-
1502.60	1526.36	1.55	970	953.50	1.73
1533.20	1556.07	1.47	1030	990.60	3.97
1563.80	1585.46	1.36	1020	979.40	4.14

from the numerical calculations. The data of the transmittance for different values of the refractive index of the dielectric are exported to the Matlab for further investigation of different performance parameters like sensitivity, FOM, ER, etc.

The COMSOL Multiphysics view of the design and its mesh structure has been depicted in Fig. 3.10 and the transmittance depicted in Fig. 3.11. The electric and magnetic filed components of the EM wave propagating in the sensor has been shown

in Fig. 3.12 at the wavelength of 1500 nm with n = 1.53. The MIM configuration is propagating TM wave where the wave is propagating in y-direction.

The comparison of the results simulated on COMSOL Multiphysics with results from Xu *et. al.* has been shown in Table 3.1. Mainly the resonant wavelength and sensitivity of the two results have been compared. A right shift of the resonant wavelength has been observed from the original result and noticed a maximum percentage of difference of 1.61%, which is very low. In the case of sensitivity, the comparison shows that the maximum percentage of difference reached 4.14%, which is also low enough to consider. From the transmittance spectra, it is observed that in both cases, original and re-simulated, the maximum value point of transmittance is near to 0.9, and minimum value points have a difference near to 0.07, which suggests that the ER is almost same. It can be concluded that results obtained from the re-simulation of the design validate the simulation procedure of the COMSOL Multiphysics for the plasmonic refractive index sensor. The proposed designs in the next chapter has been simulated using the similar methodology using the COMSOL Multiphysics.

3.5 Re-simulation With CST STUDIO SUITE

CST STUDIO SUITE is another simulation environment for the plasmonic devices. The design presented by Xu *et. al.* has been re-simulated in CST to cross-verify the simulation results. The original work was in 2D, but the only 3D structure can be designed in CST. The design parameters have been kept as original g = 33 nm, W_1 = 40 nm, L = 360 nm, W_2 = 80 nm, and the height has been chosen as 150 nm. The CST view of the geometric structure with ports of the design has been depicted in Fig. 3.13 and the transmittance has been depicted in Fig. 3.14.

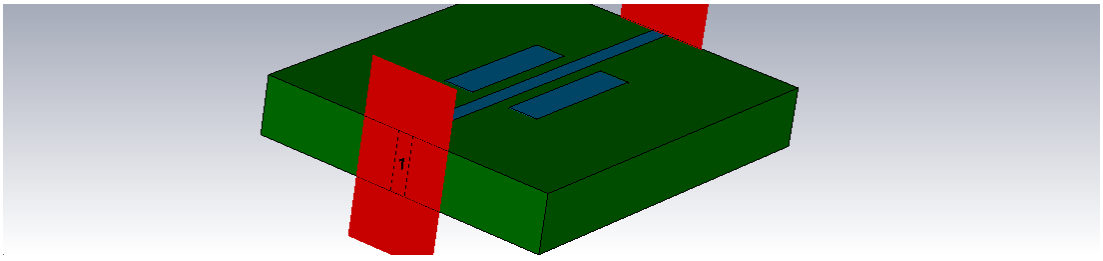

Figure 3.13: CST STUDIO SUITE view of the geometric structure with ports of the design.

The comparison of the results simulated on CST with results from Xu *et. al.* has been shown in Table 3.2. The resonant wavelength and sensitivity of the two results have been compared. A slightly left shift of the resonant wavelength has been observed from the original result. A maximum percentage of difference of 0.78% has been

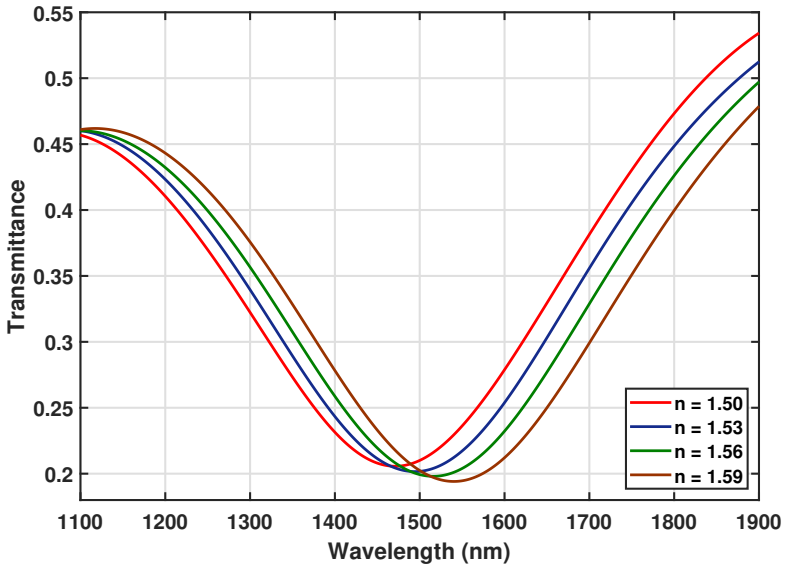

Figure 3.14: Transmittance versus wavelength re-simulated on CST STUDIO SUITE.

Table 3.2: Comparison of the results simulated on CST STUDIO SUITE with results from Xu *et. al.*.

Resonant Wavelength (nm) (Xu *et. al.*)	Resonant Wavelength (nm) (Simulated in CST)	% of Difference (Resonant Wavelength)	Sensitivity (Xu *et. al.*)	Sensitivity (Simulated in CST)	% of Difference (Sensitivity)
1473.60	1465.4	0.56	-	-	-
1502.60	1493.2	0.63	970	926.67	4.46
1533.20	1522.5	0.69	1030	976.67	5.17
1563.80	1551.6	0.78	1020	970	4.9

noticed in the case of resonant wavelength, which is very low. The comparison shows that the maximum percentage of difference reached 5.17% in the case of sensitivity. This error in the COMSOL is less than the error in the CST. The dip of the notch response obtained in CST is also showing higher FWHM than the original result and re-simulated result in COMSOL. The designing of the sensor in 3D can be a cause of this phenomenon.

Chapter 4

RI Sensor Designs, Performance Analysis, and Applications

Designing a refractive index sensor with improved performance is one of the main objectives. The refractive index sensor can have different design parameters that affect the final performance parameters. The objective is to search for a design topology of the sensor as well as a better set of design parameters to get improved performance. Three different designs of the resonator have been investigated, namely triangular, pentagonal, and semi-circular resonator. The resonators can be of disc-type and ring-type. The sensor as a biosensor and as a filter are examples of the applications of a refractive index sensor.

4.1 Sensor Design with Triangular Resonator

4.1.1 Basic Structure

The proposed designs of the sensor have been presented in Fig. 4.1 and Fig. 4.2. A disc-type and a ring-type triangular resonator are placed with a straight waveguide in the designs. The resonator is to be filled with the dielectric or material whose refractive index has to be sensed, the straight waveguide with the air, and other spaces with silver in both the cases. Thus, the designs form a MIM structure which ensures the propagation of the SPP in the interface of metal and dielectric.

In Fig. 4.1 and Fig. 4.2, the plane with dotted lines A and B denotes the ports of the sensors. The gap between the waveguides is marked with g in both cases. Assume that the equilateral triangle as resonator can be encircled by a circle with a radius R in both disc and ring-type sensors. The width of the straight waveguide and length of the side of the triangular resonator are denoted as W and L, respectively, in Fig. 4.1. The relation between L and R can be expressed as $L = \sqrt{3}R$. In ring-type resonator, L_1, L_2, W_1, and W_2 are the lengths of the equilateral triangles (outer and inner) and widths of the straight and ring waveguides respectively.

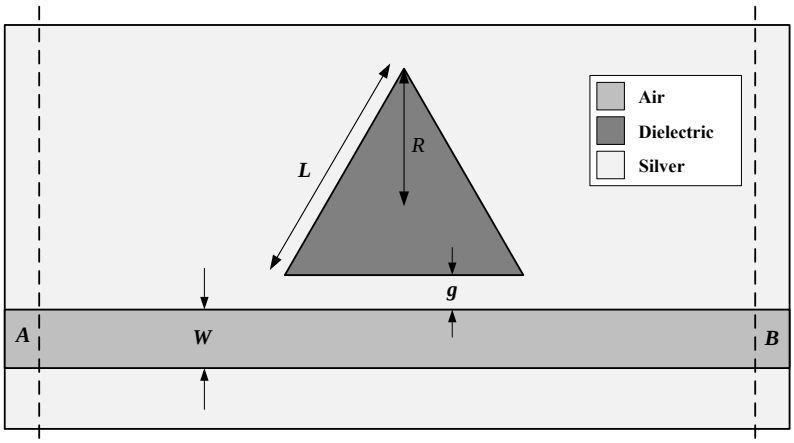

Figure 4.1: Basic structure of plasmonic waveguide with disc-type triangular resonator.

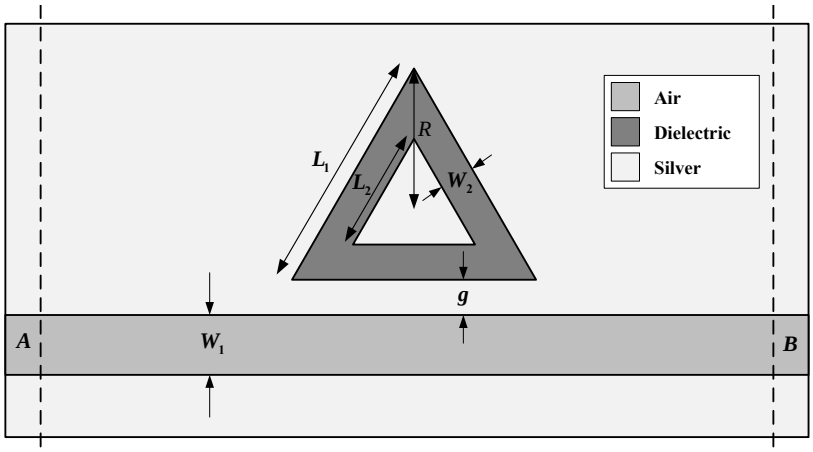

Figure 4.2: Basic structure of plasmonic waveguide with ring-type triangular resonator.

4.1.2 Results and Discussions

Disc-type Triangular Resonator

The parameters of the geometry are set as g = 38 nm, W = 140 nm, and L = 510 nm and the refractive index is varied from n = 1 to n = 1.02 with the step of 0.005 for the disc-type resonator. The transmission response of the design is shown in Fig. 4.3 which is observed to be a notch-type spectrum.

The transmittance of the sensor with a disc-type resonator for different values of the gap g is represented in Fig. 4.4. The values of the gap g are varied as 15 nm, 26 nm, 38 nm, 49 nm, and 60 nm. The coupling strength between the straight waveguide and the resonator depends on the gap between the waveguides. Here it is found that with the higher value of the gap, the coupling is lower as well as the value of the transmittance is smaller. The change of FWHM is also visible, which has an effect on FOM. The performance parameters are shown in Fig. 4.5 indicates the change of sensitivity, FOM, ER, and resonant wavelength for different values of the gap g. The

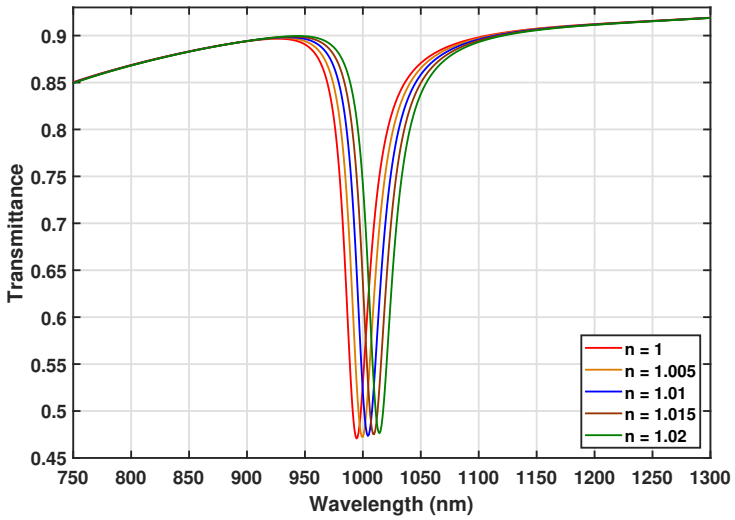

Figure 4.3: Transmittance vs wavelength for the design with disc-type triangular resonator for different values of n.

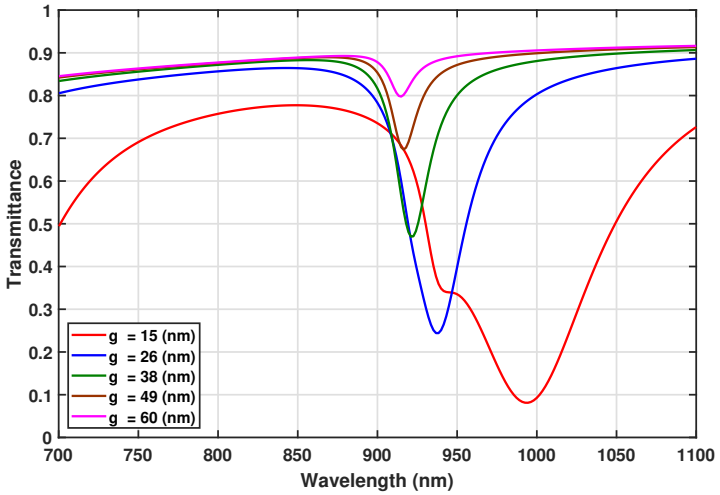

Figure 4.4: Transmittance vs wavelength for different values of gap of the design with disc-type triangular resonator.

resonance wavelength is shifting to the left that is resonant wavelength is decreasing with the increase of gap g and ER is also decreasing with the increase of the gap value. But the sensitivity remains almost the same when the gap is equal or more than 38 nm, and FOM is increasing with the increase of the gap g. If the value of the gap is less, both the sensitivity and the FOM are found to be less in value, although their ER has a higher value. At a higher value of the gap, sensitivity and FOM is high, but the ER is very small. These parameters are to be kept into consideration for designing the sensor.

The length (L) of the sides of the equilateral triangle, another design parameter of the sensor, also varied as 405 nm, 457 nm, 510 nm, 563 nm, 615 nm, 668 nm, and

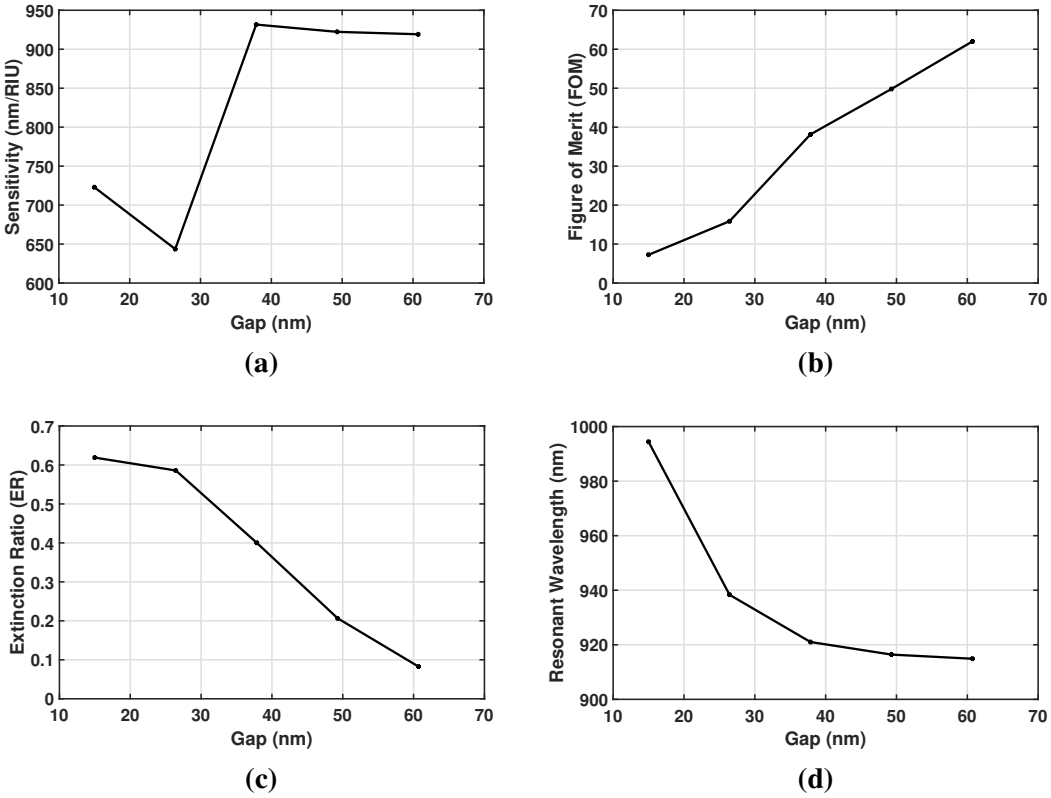

Figure 4.5: Performance parameters with the change of gap g of the RI sensor based on the disc-type triangular resonator. (a) Sensitivity, (b) FOM, (c) ER, and (d) Resonant Wavelength.

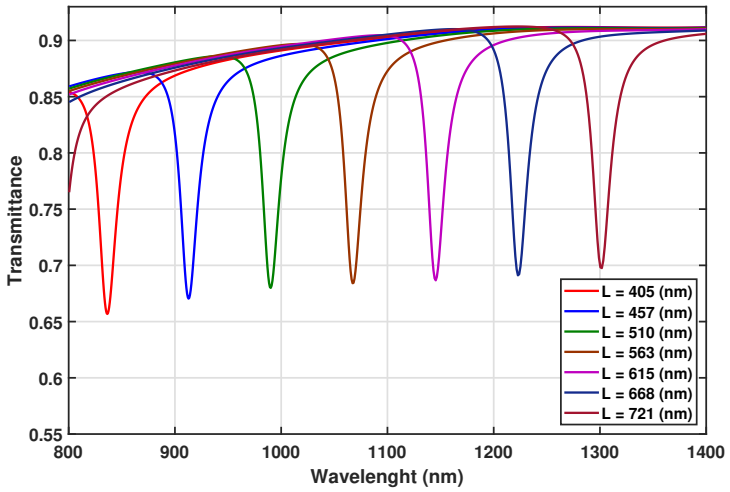

Figure 4.6: Transmittance vs wavelength for different values of length of the design with disc-type triangular resonator.

721 nm, as shown in Fig. 4.6. The sensor has been investigated for a wide range of performance controlling parameters. The performance parameters for the change of length L is depicted in Fig. 4.7. The resonant wavelength is shifting right with the increment of the length L that is resonant wavelength is showing increment with the increment of the L. The sensitivity and FOM are changing and increasing to some

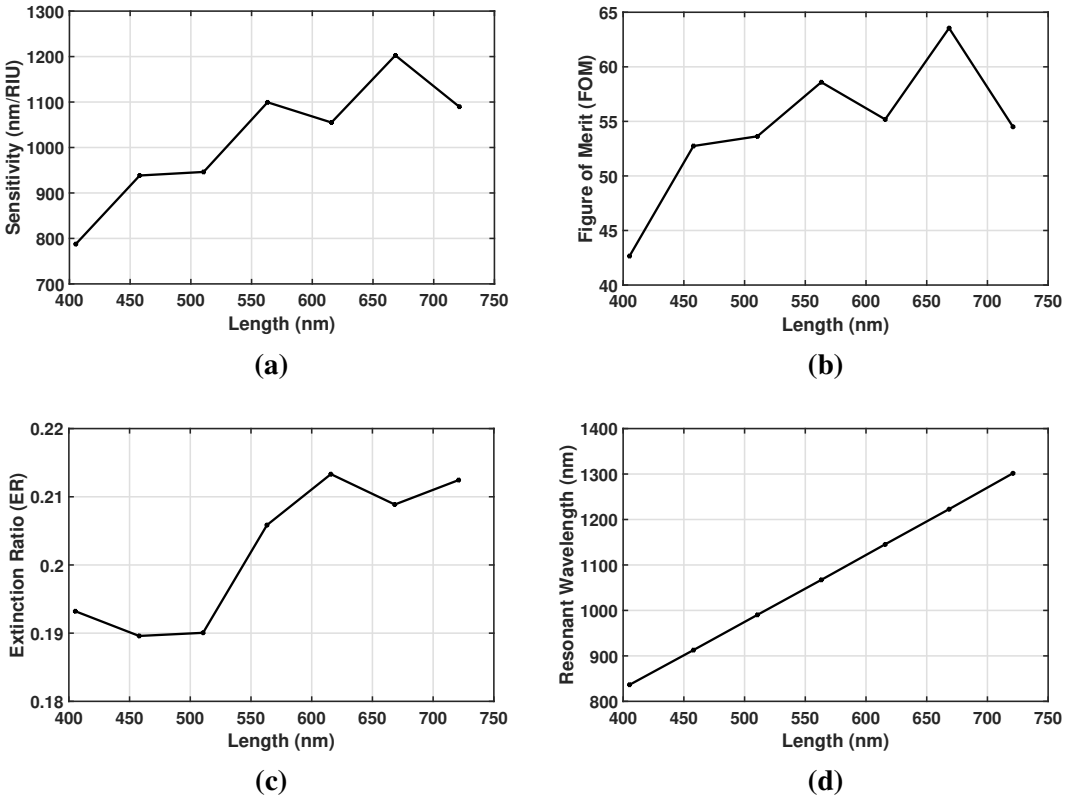

Figure 4.7: Performance parameters with the change of length L of the RI sensor based on the disc-type triangular resonator. (a) Sensitivity, (b) FOM, (c) ER, and (d) Resonant Wavelength.

extent with the increment of the L, but ER is found to be constantly keeping the average near to 0.2. The size of the device and the performance of the device is the optimization parameters. The maximum sensitivity and FOM for the disc-type sensor found to be 1203 nm/RIU and 63.5 respectively at 1223 nm resonant wavelength for g = 38 nm, and L = 668 nm.

Ring-type Triangular Resonator

In ring-type triangular resonator, the transmission response of the sensor is numerically calculated for the different design parameters: the gap (g) between the straight waveguide and resonator, the radius (R) of the circle where the outer equilateral triangle inscribed, and the width (W_2) of the ring-type resonator. These geometric parameters are set as g= 37 nm, W_1 = 140 nm, R = 340 nm, and W_2 = 160 nm and the transmittance is depicted in Fig. 4.8 with the varying wavelength from 1000 nm to 2500 nm for theIive index n = 1 to n = 1.03 with the step of 0.01. The transmittance is observed to be a notch spectrum having two modes around 1000 nm and 2000 nm of the wavelength. Fig. 4.9 represents the resonant wavelength with the change of the refractive index for two different modes. This representation shows that there is a linear relationship between the resonant wavelength and refractive index change in the case of both

the modes. The electric and magnetic filed components of the EM wave propagating in the proposed sensor has been depicted in Fig. 4.10 at the wavelength of 2085 nm with n = 1.01. The RI sensor is propagating TM wave where the wave is propagating in y-direction.

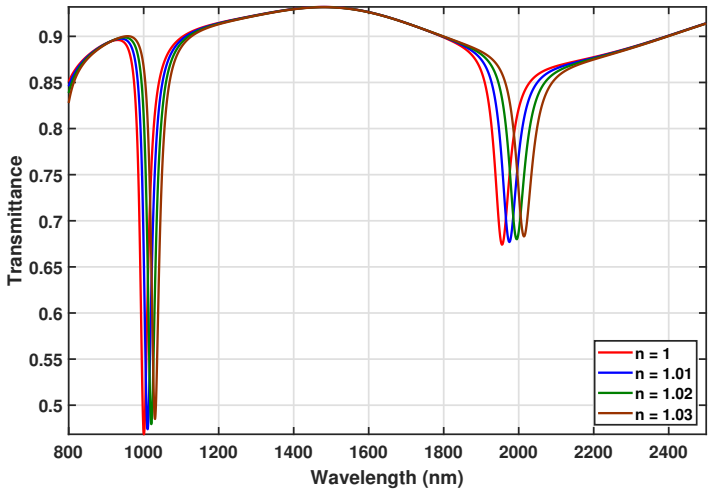

Figure 4.8: Transmittance vs wavelength for the design with ring-type triangular resonator for different values of n.

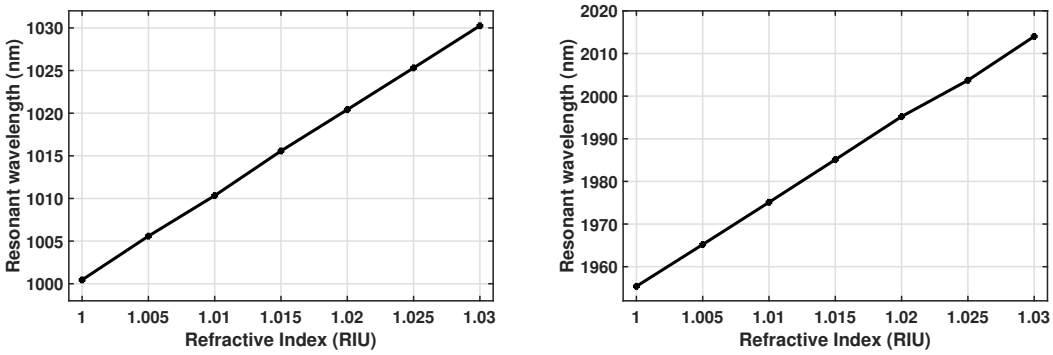

Figure 4.9: Change of resonant wavelength with the refractive index. (a) Mode 01, (b) Mode 02.

The resonant wavelength peak, sensitivity, and FOM for mode 01 and mode 02 are evaluated for the sensor and presented in Table 4.1. The representation shows that, for mode 02, initially, the maximum sensitivity achieved is 2059.1 nm/RIU for the FOM 43.1 at resonant wavelength 2014 nm for n = 1.03. Initially, the maximum sensitivity achieved as 1047.1 nm/RIU for the FOM 41.9 at the resonant wavelength of 1015.6 nm for n = 1.015 for mode 01.

The effect of design parameters has been studied by the investigation of the transmittance for different wavelengths and other performance parameters. First, the gap is

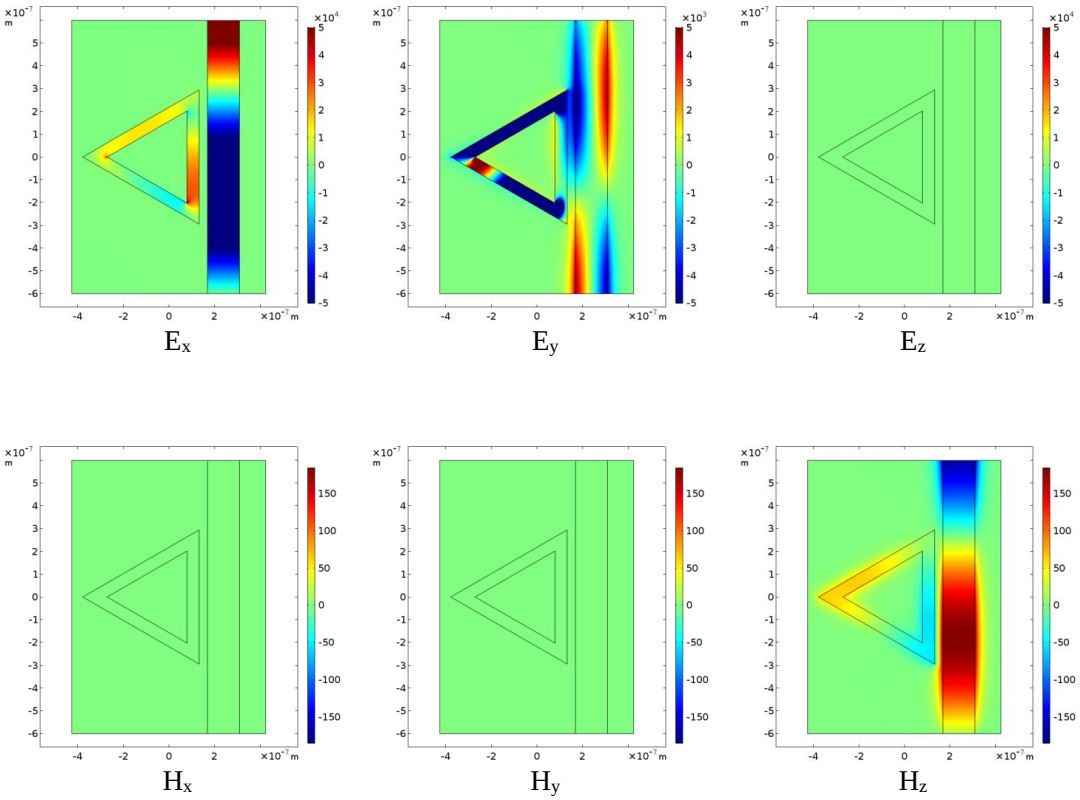

Figure 4.10: Electric and magnetic field components of the EM wave propagating in the proposed sensor at the wavelength of 2085 nm with n = 1.01.

Table 4.1: Calculation of sensitivity and FOM of the design with ring-type triangular resonator.

n	Resonant Peak (nm)		Sensitivity (nm/RIU)		FOM	
	Mode 1	Mode 2	Mode 1	Mode 2	Mode 1	Mode 2
1	1000.5	1955.4	———	———	———	———
1.005	1005.6	1965.2	1026.7	1960.8	41.2	42.9
1.01	1010.3	1975.1	950.4	1980.5	38.1	43
1.015	1015.6	1985.1	1047.1	2000.6	41.9	43
1.02	1020.4	1995.2	969.4	2021	38.7	43.1
1.025	1025.3	2003.7	978.7	1700	38.9	35.9
1.03	1030.3	2014	988.2	2059.1	39.2	43.1

varied as g being 15 nm, 26 nm, 37 nm, 49 nm, 60 nm, 72 nm, and the transmittance is depicted in Fig. 4.11 for R = 330 nm , W_2 = 200 nm, and n = 1.0. We observe minimal coupling for the higher gap value, which agrees with the theory. The change of FWHM and ER is also visible from the representation. In Fig. 4.12, Fig.4.14, and Fig. 4.16, different performance parameters i.e sensitivity, FOM, ER, and resonant wavelength has been depicted for different design parameters i.e gap g, radius R, and width W_2 respectively. The design parameters are varied over a very wide range of

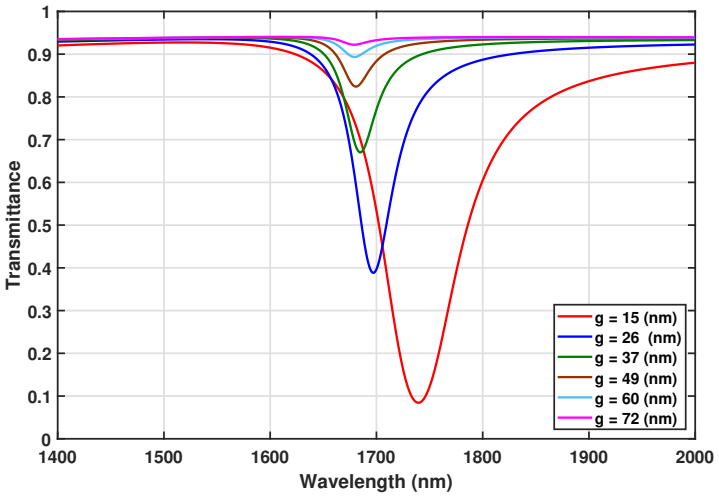

Figure 4.11: Transmittance vs wavelength for different values of gap of the design with ring-type triangular resonator.

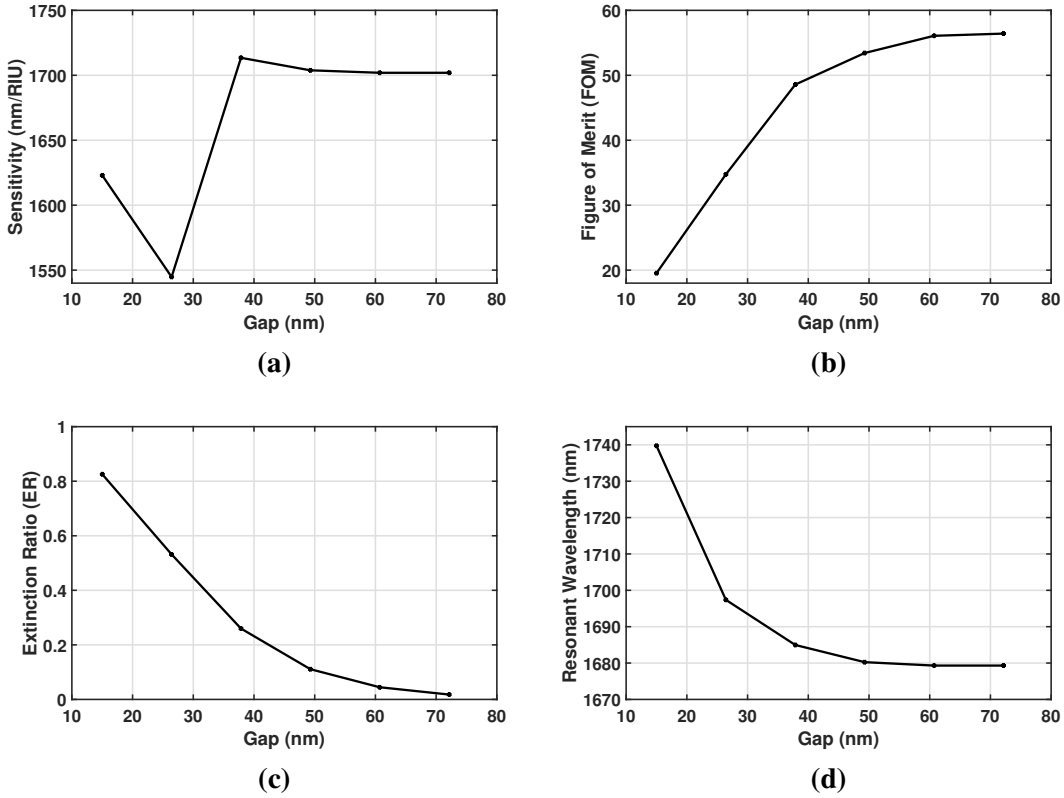

Figure 4.12: Performance parameters with the change of gap of the RI sensor based on the ring-type triangular resonator. (a) Sensitivity, (b) FOM, (c) ER, and (d) Resonant Wavelength.

values, which allows us to explore the performance of the sensor in the different frequency ranges. The resonant frequency is observed to be shifting left that is reducing with the increment of the gap g, shown in Fig. 4.12. The FOM shows increment, and the ER shows decrements with the increment in the design parameter g. However, the sensitivity shows to be almost constant after g = 38 nm before which, it shows to have

less sensitivity.

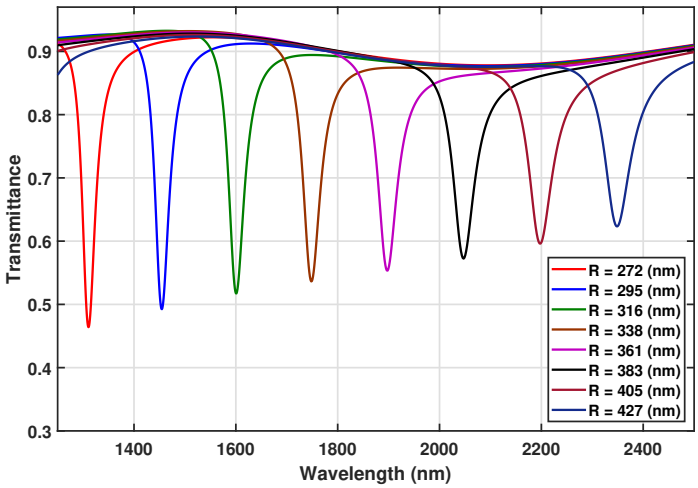

Figure 4.13: Transmittance vs wavelength for different values of radius of the design with ring-type triangular resonator.

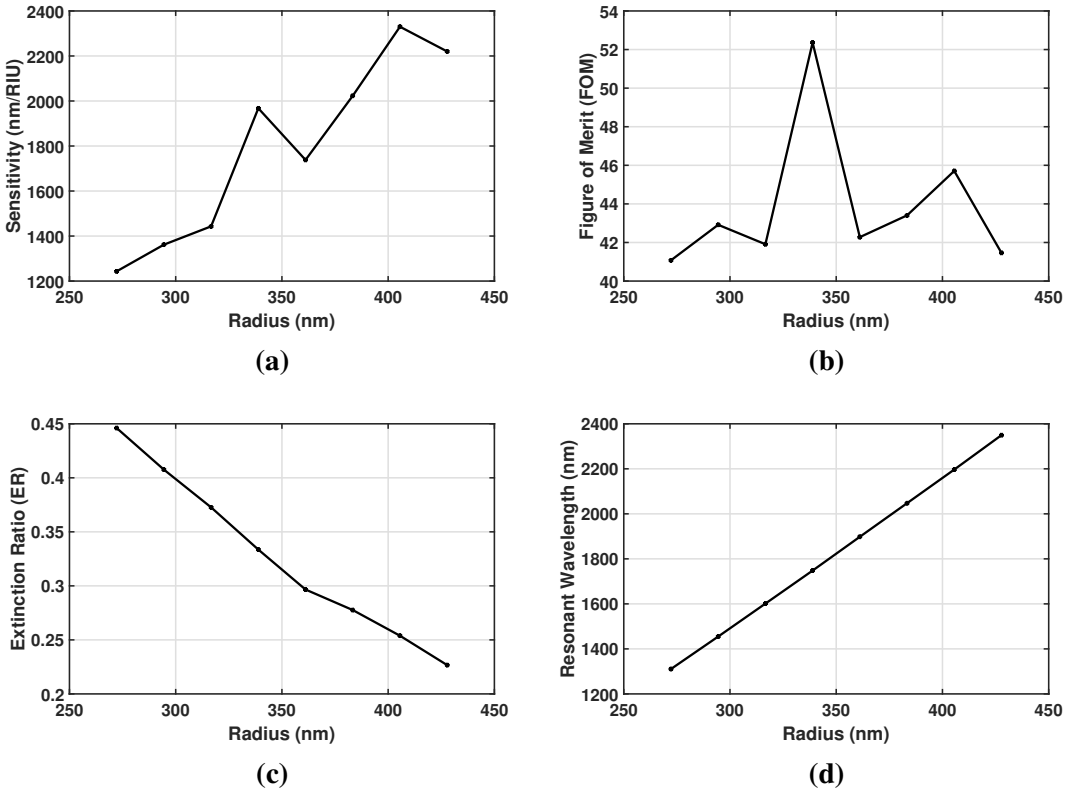

Figure 4.14: Performance parameters with the change of radius of the RI sensor based on the ring-type triangular resonator. (a) Sensitivity, (b) FOM, (c) ER, and (d) Resonant Wavelength.

The radius R of the circle inscribing the triangular resonator is being varied as 272 nm, 295 nm, 316 nm, 338 nm, 361 nm, 383 nm, 405 nm, and 427 nm and the transmittance is depicted in Fig. 4.13 for g = 32 nm , W_2 = 200 nm, and n = 1.0. This represen-

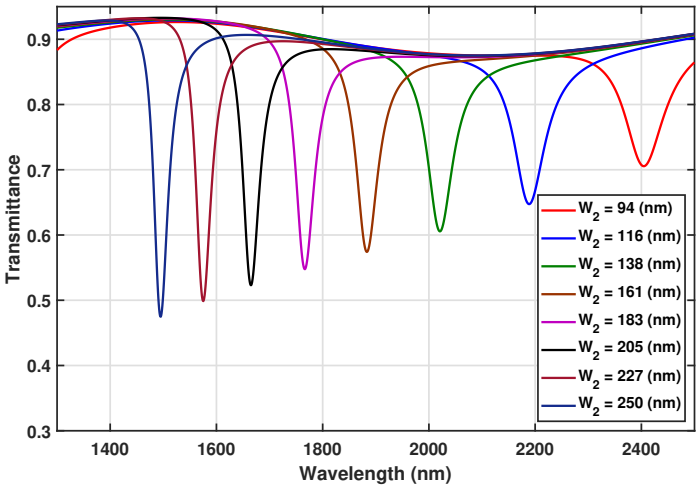

Figure 4.15: Transmittance vs wavelength for different values of width of the design with ring-type triangular resonator.

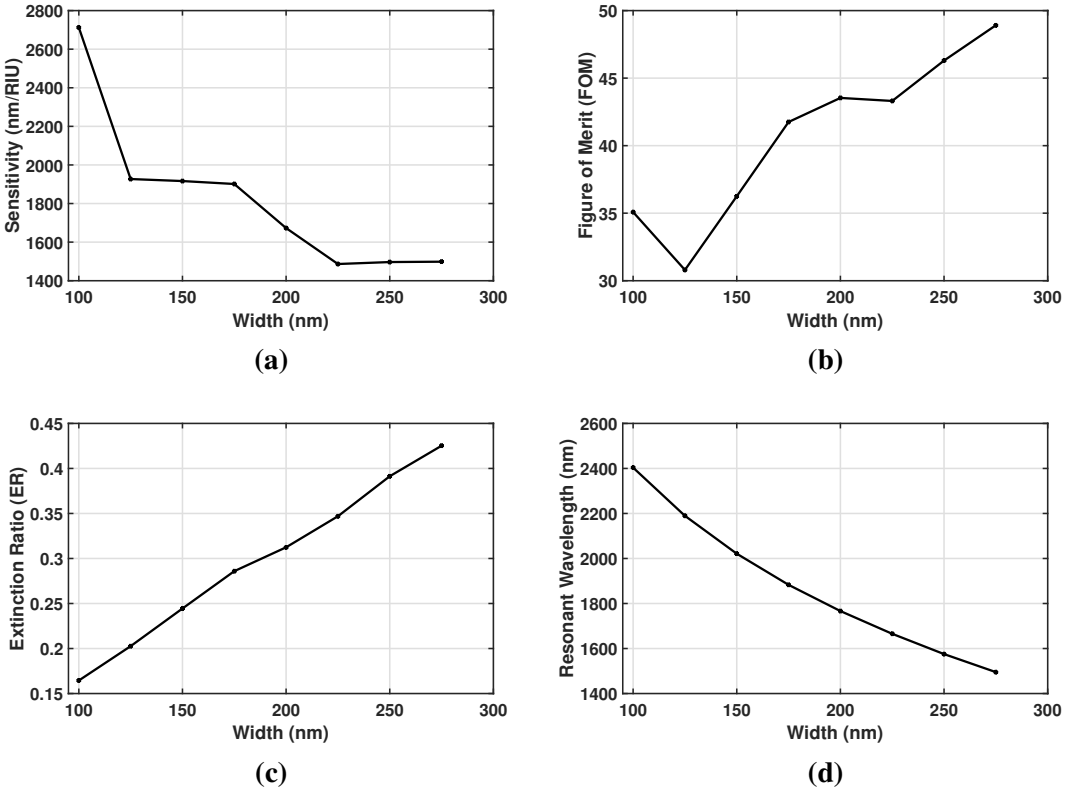

Figure 4.16: Performance parameters with the change of width of the RI sensor based on the ring-type triangular resonator. (a) Sensitivity, (b) FOM, (c) ER, and (d) Resonant Wavelength.

tation shows that the sensor can operate in a wide range of wavelengths, which can be set by choice of radius R. The performance parameters are shown in Fig. 4.14 where resonant wavelength shows shift right property i.e., the resonant wavelength is increasing for the increment of radius R. The maximum sensitivity found to be around 2275 nm/RIU, but the FOM is around 46, again for the maximum FOM of 52.36, the

sensitivity is found to be 1968 nm/RIU. Here the ER is found to be decreasing with the increment of the radius R. With the smaller size of the device, having g = 32 nm, W_2 = 200 nm, and R = 340 nm, it is possible to attain high enough sensitivity with a high value of FOM.

Lastly, the width W_2 of the resonator is varied as being 94 nm, 116 nm, 138 nm, 161 nm, 183 nm, 205 nm, 227 nm, 250 nm, and the transmittance is depicted in Fig. 4.15 for g = 32 nm , R = 330 nm, and n = 1.0. The representation shows that both the FWHM and the ER are changing with the change of the width W_2, which is the effect of the SPP path width. In Fig. 4.16, the resonant wavelength is shifting towards left i.e., decreasing with the increase of width W_2 and also ER is increasing with the increase of W_2. For higher sensitivity, the FOM is found to have a lower value; and for lower sensitivity, the FOM is high. A maximum sensitivity of 2713 nm/RIU with a quite high FOM of 35.1 is observed For the width value of W_2 = 94 nm of this sensor.

The comparison of the performance and design parameters of the disc-type and ring-type triangular resonator for maximum sensitivity and maximum FOM has been shown in Table 4.2.

Table 4.2: Comparison of the performance parameters and design parameters of the disc-type and ring-type triangular resonator for the maximum sensitivity and the maximum FOM.

		Disc-type Resonator		**Ring-type Resonator**	
		For Max Sensitivity	For Max FOM	For Max Sensitivity	For Max FOM
Performance Parameters	Sensitivity (nm/RIU)	1203	1203	2713	1968
	FOM	63.5	63.5	35.1	52.36
	ER	0.209	0.209	0.164	0.334
	Resonant wavelength (nm)	1223	1223	2404	1748
Design Parameters	g (nm)	38	38	32	32
	L / R (nm)	668	668	330	340
	W_2 (nm)	N/A	N/A	94	200

4.1.3 Conclusion

The design with the ring-type triangular resonator is an upgrade of the design with the disc-type resonator in the sense of the performance of the sensors. Finally, the ring-type triangular resonator is the proposed design, which has the sensitivity of 1968 nm/RIU with maximum FOM of this sensor 52.36 at resonant wavelength 1748 nm for the design parameters as g = 32 nm, R = 338 nm and W_2 = 200 nm. For maximum sensitivity as high as 2713 nm/RIU with FOM 35.1 with the design parameters as g = 32 nm, R = 330 nm and W_2 = 94 nm can be considered.

4.2 Sensor Design with Pentagonal Resonator

4.2.1 Basic Structure

The proposed refractive index sensor contains a pentagonal resonator. In Fig. 4.17 and 4.18, disc-type and ring-type pentagonal resonator has been placed with a straight waveguide respectively. The geometric parameters for disc-type resonator design are the width of the straight waveguide denoted by W, the length of a side of the pentagonal shaped resonator denoted by L, and the gap between the straight waveguide and the resonator denoted by g. If the regular pentagonal resonator circumscribed by a circle with a radius R, the relationship between L and R can be described by the following equation,

$$L = \sqrt{\frac{5-\sqrt{5}}{2}}R. \tag{4.1}$$

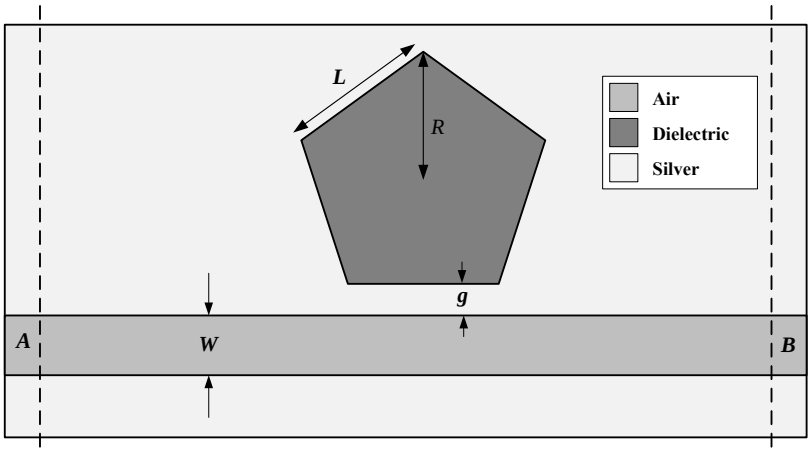

Figure 4.17: Basic structure of plasmonic waveguide with disc-type pentagonal resonator.

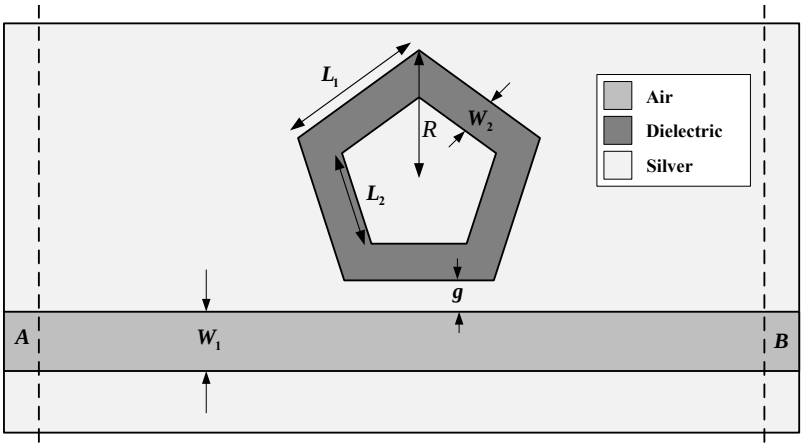

Figure 4.18: Basic structure of plasmonic waveguide with ring-type pentagonal resonator.

The geometric parameters of the ring-type resonator design are the width of the straight

waveguide denoted by W_1, the lengths of the sides of the pentagonal resonator having outer and inner pentagonal shape denoted by L_1 and L_2 respectively, the width of the ring denoted by W_2, and the gap between the straight waveguide and the resonator denoted by g. In this case, if the outer pentagon circumscribed by a circle with a radius R, the relationship between L_1 and R can also be described by the Equation 4.1. In the case of both the designs, the air has been placed in the straight waveguide, the dielectric whose refractive index is to be detected placed in the resonator (disc-type or ring-type), silver Ag has been placed in the rest of the part of the design. Here the input and output port has been marked with the dotted line and denoted by A and B, respectively. The transmittance can be calculated by the Equation 3.13 where power at port A is P_{in} and power at port B is P_{tr}.

4.2.2 Results and Discussions

Disc-Type Pentagonal Resonator

The design has been simulated by using a numerical calculation. The sensor has been first calculated numerically using the geometric parameters set to gap g = 32 nm and the radius of the circle, which circumscribe the resonator R = 415 nm and the refractive index is varied from n =1.0 to n = 1.02 with a step of 0.005. The transmittance of the sensor with the change of wavelength has been depicted in Fig. 4.19 for the different n values of 1.0, 1.01 and 1.02. Two different modes are observed in the representation, and the resonant wavelength for different values of the refractive index has been depicted in Fig. 4.20. The resonant wavelengths are changing almost linearly with the change of refractive index.

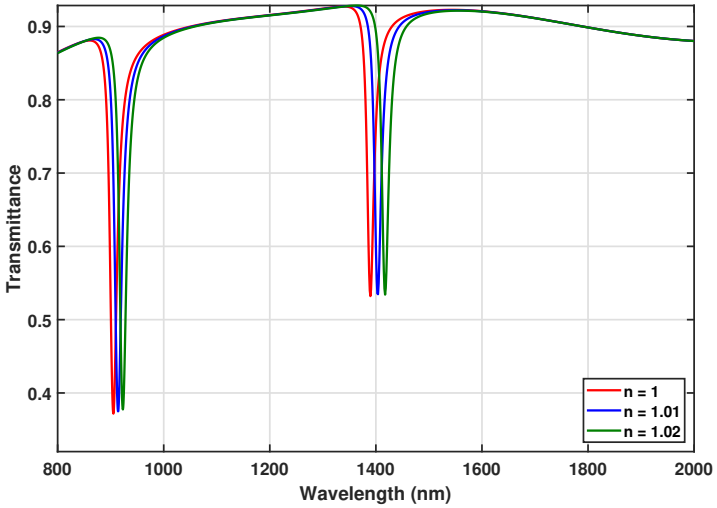

Figure 4.19: Transmittance vs wavelength for the design with disc-type pentagonal resonator for different values of n.

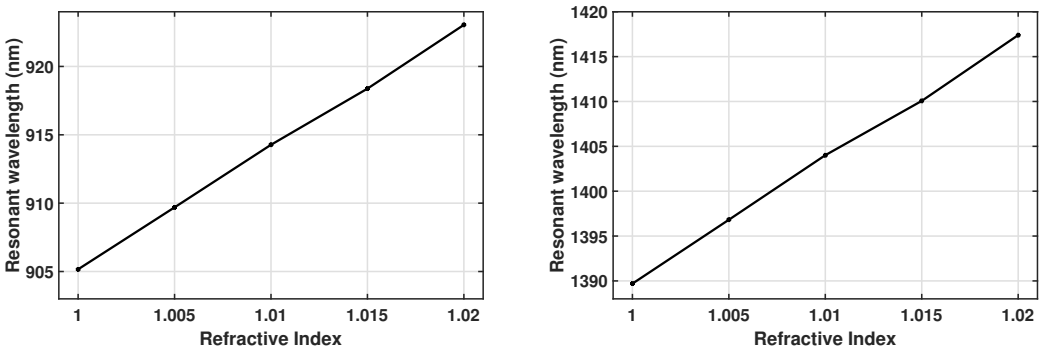

Figure 4.20: Change of resonant wavelength with the refractive index. (a) Mode 01, (b) Mode 02.

Table 4.3: Calculation of sensitivity and FOM for the design with disc-type pentagonal resonator.

n	Resonant Peak (nm)		Sensitivity (nm/RIU)		FOM	
	Mode 1	Mode 2	Mode 1	Mode 2	Mode 1	Mode 2
1	905.2	1389.7	——	——	——	——
1.005	909.7	1396.8	906.2	1424.2	95.1	56.4
1.01	914.3	1404.0	915.3	1438.9	95.4	56.9
1.015	918.4	1410.1	821.4	1210.4	79.5	50.9
1.02	923.0	1417.4	932.9	1466.4	95.9	57.8

The calculation of sensitivity for the disc-type pentagonal shaped resonator has been shown in Table 4.3. From the representation, it is observed that the maximum sensitivity achieved for mode 01 is 932.9 nm/RIU, with a high FOM of 95.9 having a resonant wavelength peak at 923 nm. For mode 02, a maximum sensitivity of 1466.4 nm/RIU has been achieved with having FOM of 57.8 at a resonant wavelength of 1417.4 nm. The FOMs calculated for mode 01 are higher than those of mode 02, but the sensitivity is found to be higher for mode 02.

The gap g between the straight waveguide and the resonator has been varied as 14 nm, 23 nm, 32 nm, 41 nm, and 50 nm and their corresponding transmittance for R = 300 nm, and n = 1.0 has been depicted in Fig. 4.21 for the change of wavelength. This shows that with the increase of gap, the transmittance is changing and getting less coupled, making the transmittance close to unity. The variation of the performance parameters with the change of the gap has been depicted in Fig. 4.22. The ER is decreasing, and the FOM is increasing with the increment of the gap g. The optimum gap should be chosen depending on the application. The sensitivity has been observed to be within the range of 1000-1200 nm/RIU, and the resonant wavelength is shifting

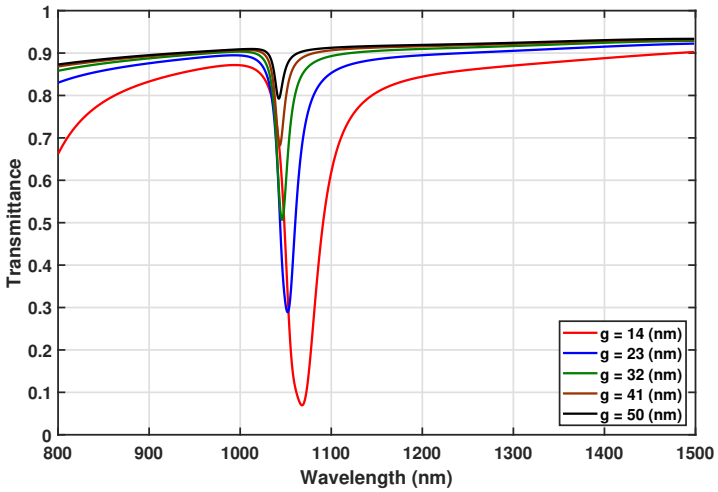

Figure 4.21: Transmittance vs wavelength for different values of gap g of the design with disc-type pentagonal resonator.

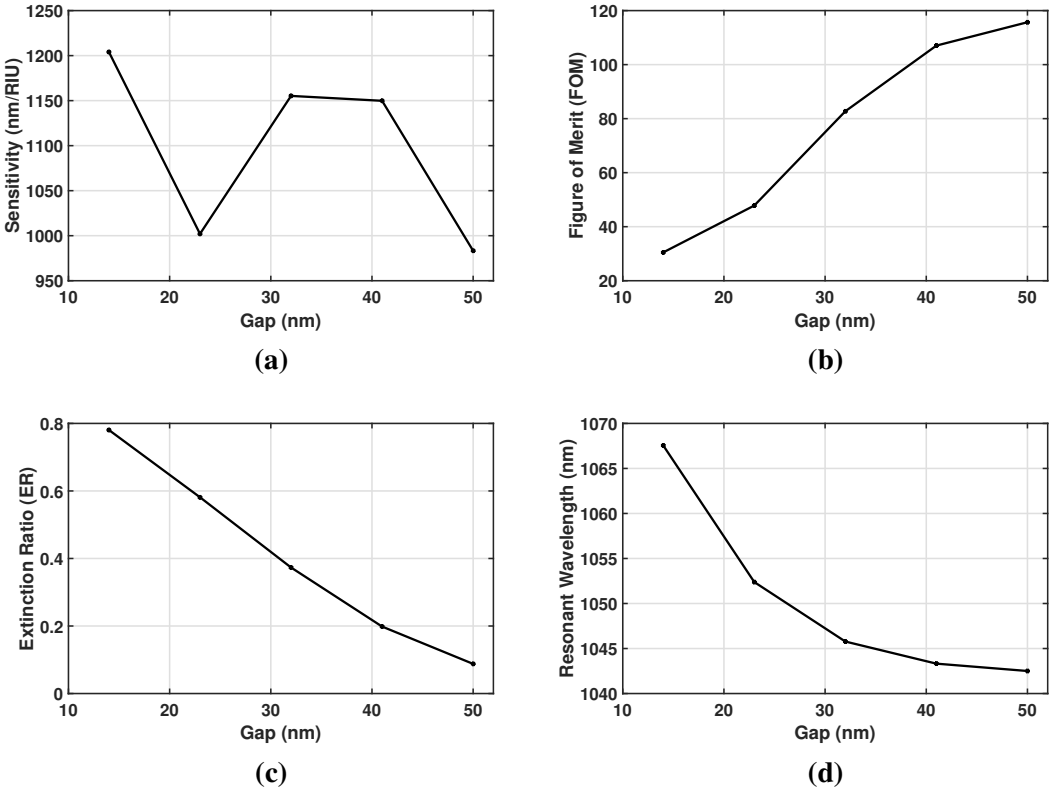

Figure 4.22: Performance parameters with the change of gap g of the RI sensor based on the disc-type pentagonal resonator. (a) Sensitivity, (b) FOM, (c) ER, and (d) Resonant Wavelength.

to the left with the increment of gap g.

The radius R of the circle which circumscribes the pentagonal shaped resonator has been varied as 331 nm, 373 nm, 415 nm, 457 nm, 500 nm for g = 14 nm and n = 1.0

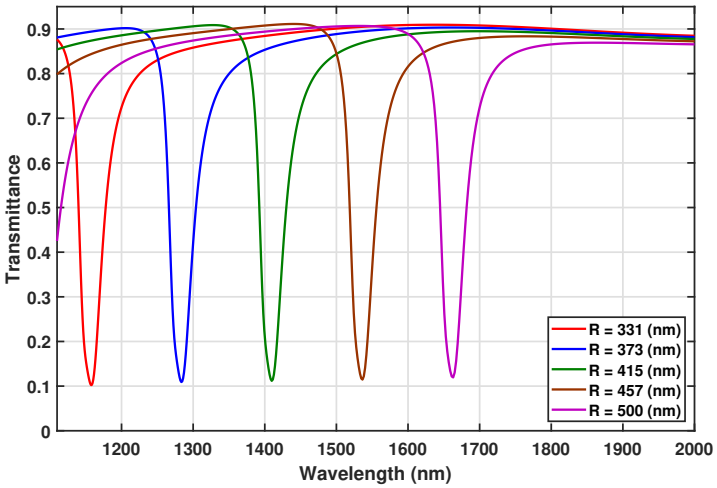

Figure 4.23: Transmittance vs wavelength for different values of radius R of the design with disc-type pentagonal resonator.

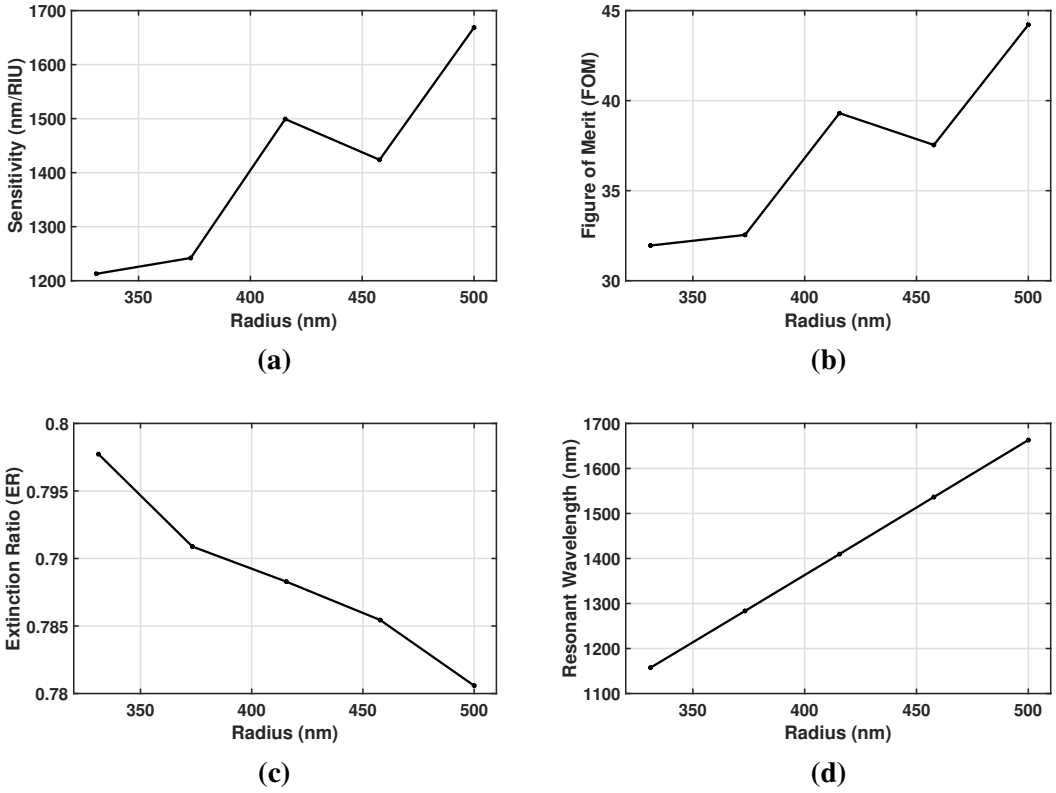

Figure 4.24: Performance parameters with the change of radius R of the RI sensor based on the disc-type pentagonal resonator. (a) Sensitivity, (b) FOM, (c) ER, and (d) Resonant Wavelength.

and their corresponding transmittance for the change of wavelength has been depicted in Fig. 4.23. With the increment of the radius R, the resonant wavelength is shifting to the right. The operating range of the sensor can be estimated from this. The other performance parameters have been depicted in Fig. 4.24. The ER is found to be in the

range of 0.78 to 0.8, which is quite high, but the sensitivity and FOM are increasing to some extent with the increment of the radius R. A maximum sensitivity of 1669 nm/RIU with having FOM of 44.21 has been achieved for radius R = 500nm and g = 14 nm at the resonant wavelength of 1663 nm.

Ring-Type Pentagonal Resonator

The numerical calculation of the transmittance of the sensor with the ring-type resonator has been performed using COMSOL Multiphysics for the refractive index change from n = 1.0 to n = 1.02 with the step of 0.005. The geometric parameters are set as the gap between the straight waveguide and the resonator g = 32 nm, the radius of the circle which circumscribes the outer pentagonal shape of the ring-type resonator R = 295 nm, and the width of the ring of the resonator W_2 = 70 nm. The transmittance for the change of the wavelength has been depicted in Fig. 4.25 for n of 1.0, 1.01, 1.02. In Fig. 4.26, the resonant wavelength shift for the change of refractive index has been depicted for two different modes. The relationship between resonant wavelength and the refractive index is almost linear, which can also be represented by a simple linear equation.

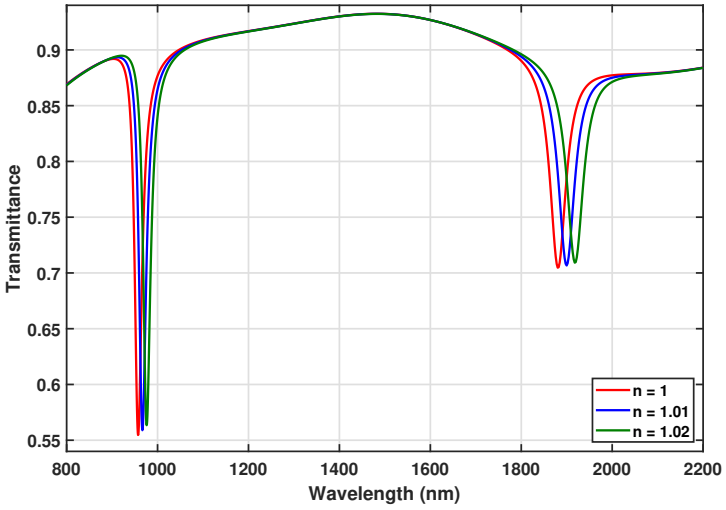

Figure 4.25: Transmittance vs wavelength for the design with ring-type pentagonal resonator for different values of n.

The Table 4.4 represents the calculation of sensitivity for the ring-type pentagonal shaped resonator for two different modes. From the representation, the maximum sensitivity achieved for mode 01 is 1013.4 nm/RIU having a FOM of 56.1 at resonant wavelength of 962.1 nm and the maximum sensitivity for the mode 02 has been achieved to be 2173.8 nm/RIU having a FOM of 57.1 at resonant wavelength of 1880.1 nm. The FOMs are found to be almost constant for both the mode 01 and mode 02.

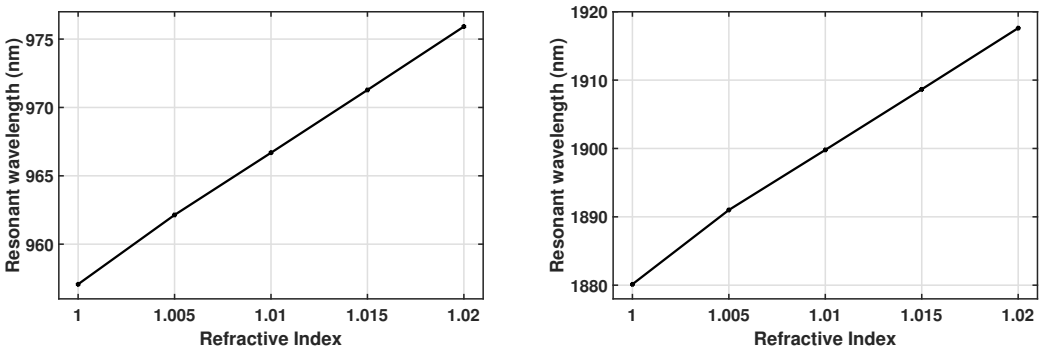

Figure 4.26: Change of resonant wavelength with the refractive index. (a) Mode 01, (b) Mode 02.

Table 4.4: Calculation of sensitivity and FOM for the design with ring-type pentagonal resonator.

n	Resonant Peak (nm)		Sensitivity (nm/RIU)		FOM	
	Mode 1	Mode 2	Mode 1	Mode 2	Mode 1	Mode 2
1	957.1	1880.1	———	———	———	———
1.005	962.1	1891.0	1013.4	2173.8	56.1	57.1
1.01	966.7	1899.8	909.9	1757.2	50.3	45.7
1.015	971.3	1908.7	918.5	1773.6	50.7	45.6
1.02	975.9	1917.6	927.3	1790.3	51.1	45.6

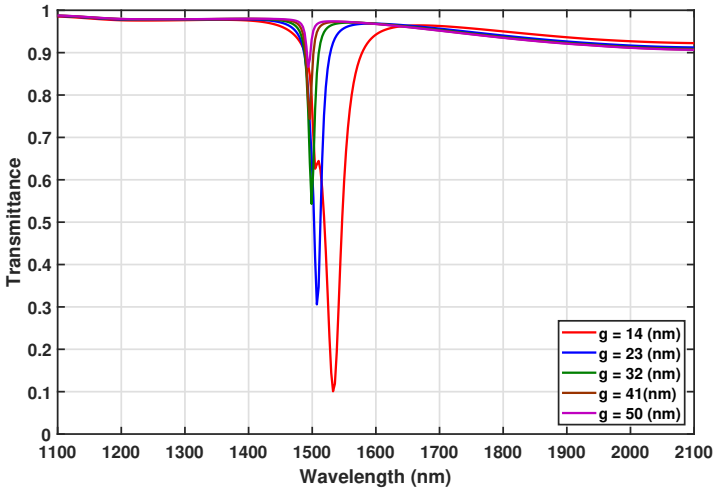

Figure 4.27: Transmittance vs wavelength for different values of gap of the design with ring-type pentagonal resonator.

To explore the design area, first the gap g is varied as 14 nm, 23 nm, 32 nm, 41 nm,

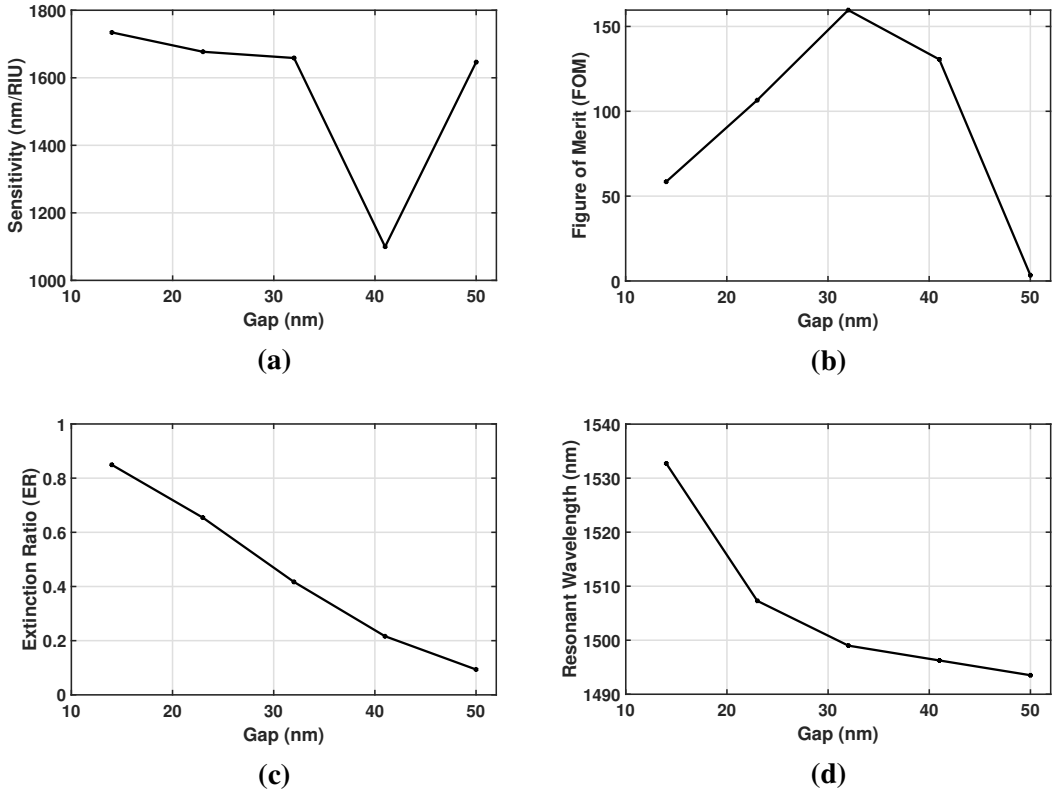

Figure 4.28: Performance parameters with the change of gap of the RI sensor based on the ring-type pentagonal resonator. (a) Sensitivity, (b) FOM, (c) ER, and (d) Resonant Wavelength.

and 50 nm keeping the other parameters as R = 235 nm, W_2 = 70 nm, and n = 1.0. The transmission response of the sensor for this setup has been depicted in Fig. 4.27 for the change in wavelength. The representations show that there is a small change in terms of resonant wavelength, but the extinction ratio is getting smaller with the increment of the gap g. It is clearly shown in Fig. 4.28 where it is representing the performance parameters change with the increment of the gap g. The maximum FOM is found to be 159.6, and the corresponding sensitivity is 1659 nm/RIU, ER is 0.416 at resonant wavelength of 1499 nm for gap g = 32 nm.

The radius of the circle which circumscribe the outer pentagonal shape of the ring-type resonator is varied as 217 nm, 236 nm, 255 nm, 274 nm, 293 nm, 312 nm, and 331 nm keeping other parameters as g = 32 nm, W_2 = 70 nm, and n = 1.0. The transmittance has been depicted in Fig. 4.29 for the change of wavelength. This representation has been clearly shown by the performance parameters, which has been depicted in Fig. 4.30. The resonant wavelength is shifting to the right i.e., increasing with the increment of the radius R, but the ER is decreasing. The sensitivity is increasing randomly and reached 2325 nm/RIU at R = 331 nm. The FOM profile is showing a peak of 52.7 at R = 293 nm, and other values are less than that.

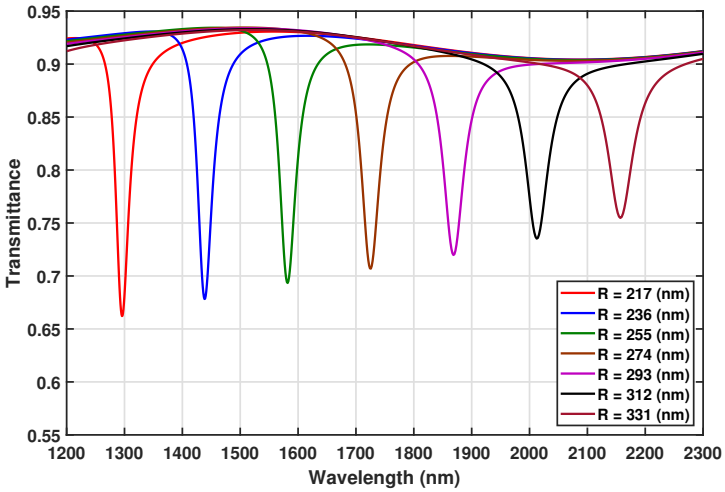

Figure 4.29: Transmittance vs wavelength for different values of radius of the design with ring-type pentagonal resonator.

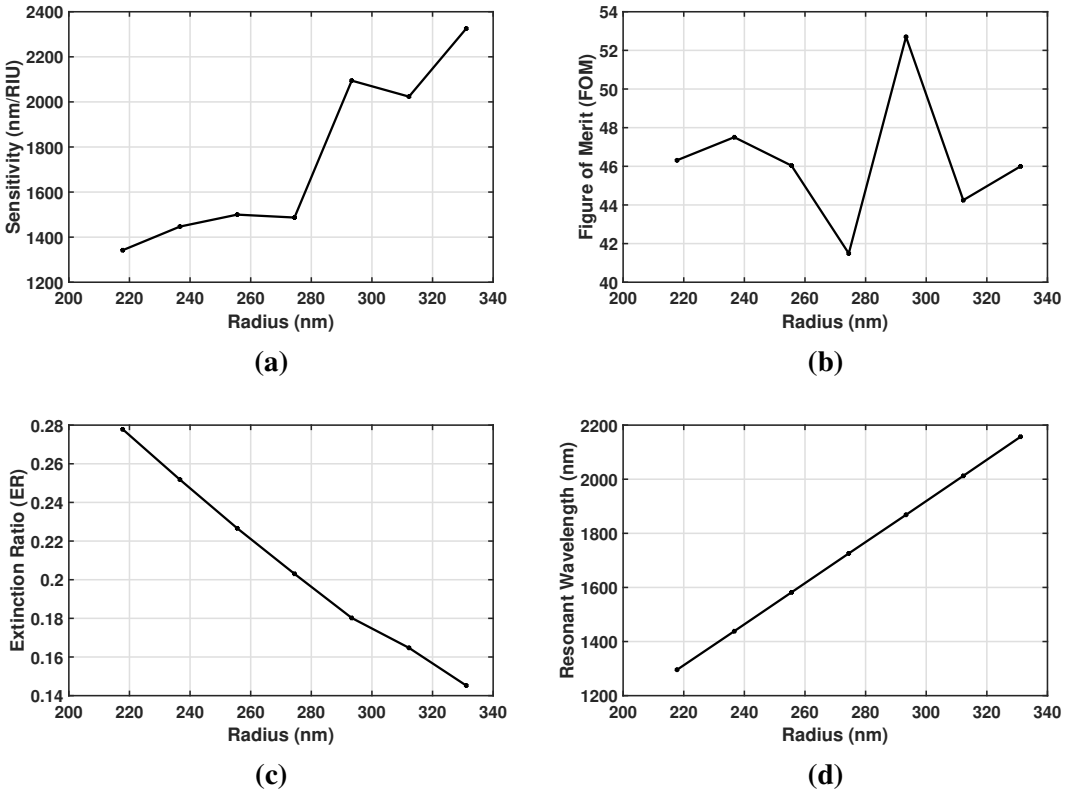

Figure 4.30: Performance parameters with the change of radius of the RI sensor based on the ring-type pentagonal resonator. (a) Sensitivity, (b) FOM, (c) ER, and (d) Resonant Wavelength.

Finally the width of the ring of the resonator W_2 has been varied as 45 nm, 71 nm, 96 nm, 122 nm, and 147 nm keeping the other parameters as g = 32 nm, R = 235 nm, and n = 1.0. The transmission response corresponding to this setup has been depicted in Fig. 4.31 and the performance parameters change with the increment of the width W_2

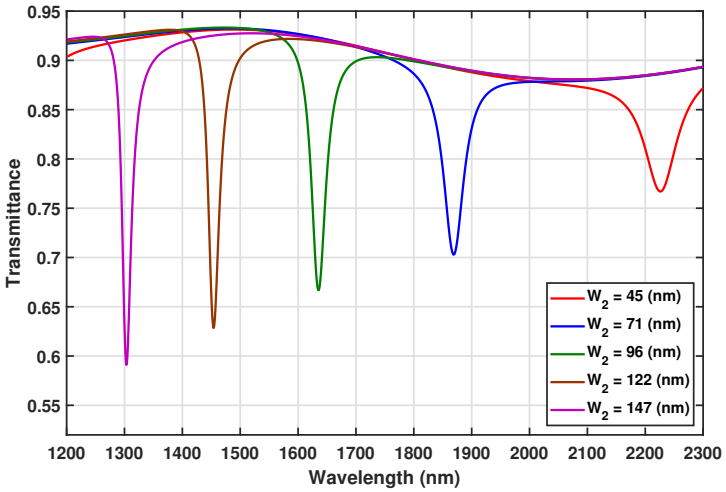

Figure 4.31: Transmittance vs wavelength for different values of width of the design with ring-type pentagonal resonator.

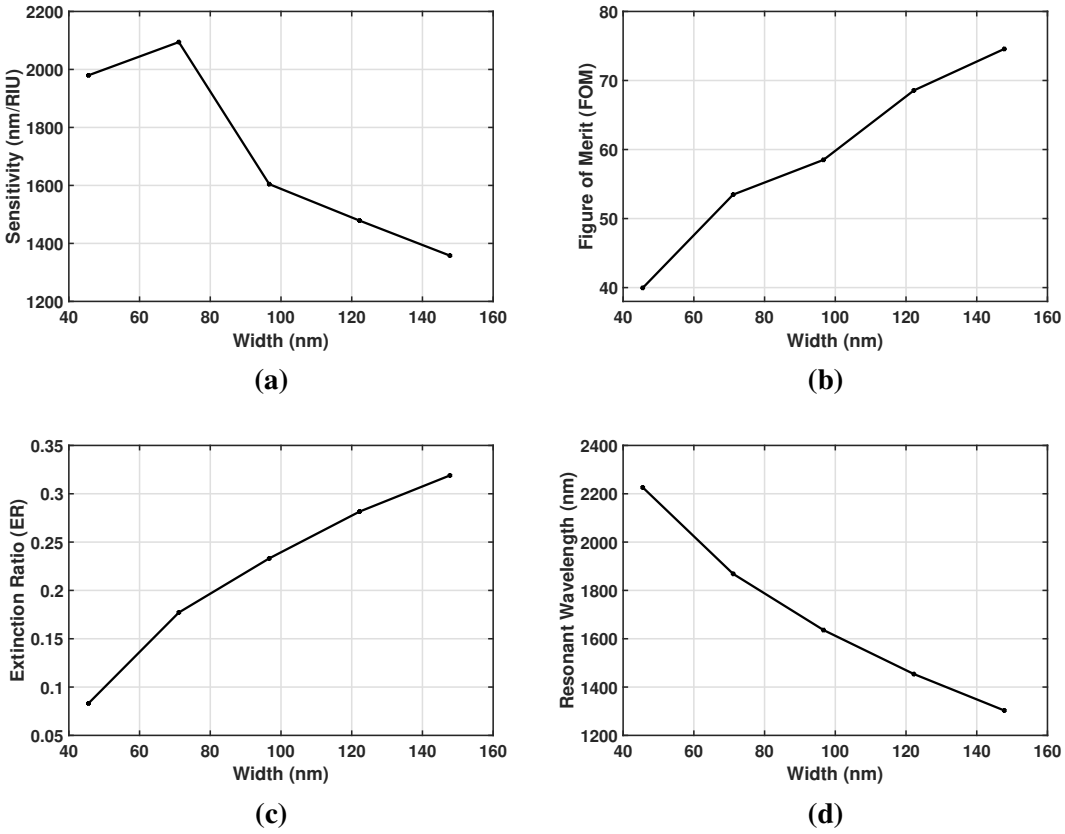

Figure 4.32: Performance parameters with the change of width of the RI sensor based on the ring-type pentagonal resonator. (a) Sensitivity, (b) FOM, (c) ER, and (d) Resonant Wavelength.

has been depicted in Fig. 4.32. The resonant wavelength is shifting towards the left i.e., decreasing with the increase of width W_2, but the ER is increasing with a lower rate. The sensitivity has fallen down after the radius increased above 70 nm, but the

FOM is increasing with the increase of the width W_2.

Considering all the cases, a maximum sensitivity of 2325 nm/RIU has been achieved with a FOM of 46 for the design parameters g = 32 nm, R = 331 nm, and W_2 = 70 nm at resonant wavelength peak of 2157 nm. The maximum FOM of 159.6 has been achieved with the sensitivity of 1659 nm/RIU for the design parameters g = 32 nm, R = 235 nm, and W_2 = 70 nm at the resonant wavelength peak of 1499 nm.

The comparison of the performance and design parameters of the disc-type and ring-type pentagonal resonator for maximum sensitivity and maximum FOM has been shown in Table 4.5.

Table 4.5: Comparison of the performance parameters and design parameters of the disc-type and ring-type pentagonal resonator for the maximum sensitivity and the maximum FOM.

		Disc-type Resonator		**Ring-type Resonator**	
		For Max Sensitivity	For Max FOM	For Max Sensitivity	For Max FOM
Performance Parameters	Sensitivity (nm/RIU)	1669	983.2	2325	1659
	FOM	44.21	115.7	46	159.6
	ER	0.78	0.09	0.15	0.42
	Resonant wavelength (nm)	1663	1043	2157	1499
Design Parameters	g (nm)	14	50	32	32
	R (nm)	500	300	331	235
	W_2 (nm)	N/A	N/A	70	70

4.2.3 Conclusion

The design with the ring-type pentagonal resonator is an upgrade of the design with the disc-type resonator in the sense of the performance of the sensors. Finally, among these, the ring-type pentagonal resonator is the proposed design, which has the maximum sensitivity of 2325 nm/RIU for a FOM of 46 at resonant wavelength 2157 nm for the design parameters as g = 32 nm, R = 331 nm and W_2 = 70 nm. For maximum FOM as high as 159.6 with the sensitivity of 1659 nm/RIU at resonant wavelength of 1499 nm for the design parameters as g = 32 nm, R = 235 nm and W_2 = 70 nm can be considered.

4.3 Sensor Design with Semi-Circular Resonator

4.3.1 Basic Structure

The proposed sensors consist of semi-circular resonators, which are of disc-type and ring-type. The two configurations of the refractive index sensor, disc-type and ring-type resonator, have been depicted in Fig. 4.33 and 4.34. The resonators are placed with a straight waveguide. The geometric parameters of the disc-type semi-circular are the width of the straight waveguide denoted by W, the radius of the circle to which the semi-circle belongs denoted by R, and the gap between the straight waveguide and the resonator denoted by g. The geometric parameters of the ring-type semi-circular resonator are the width of the straight waveguide denoted by W, the gap between the straight waveguide and the resonator denoted by g, and the radii of the circles to which the outer and inner semi-circle belongs denoted by R_1 and R_2 respectively. The width of the ring of the ring-type resonator can be expressed as

$$W_2 = R_1 - R_2. \tag{4.2}$$

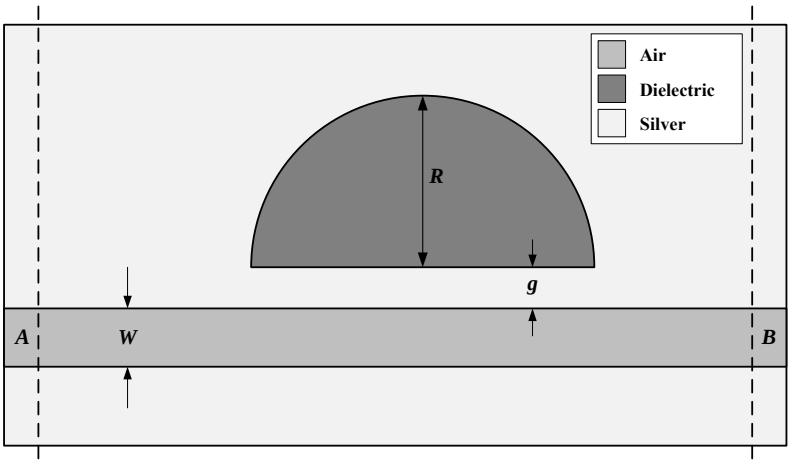

Figure 4.33: Basic structure of plasmonic waveguide with disc-type semi-circular resonator.

In the case of both the designs, the air has been placed in the straight waveguide, the dielectric whose refractive index is to be detected placed in the resonator (disc-type or ring-type), silver Ag has been placed in the rest of the part of the design. Here the input and output port has been marked with the dotted line and denoted by A and B, respectively. The transmittance can be calculated by the Equation 3.13 where power at port A is P_{in} and power at port B is P_{tr}.

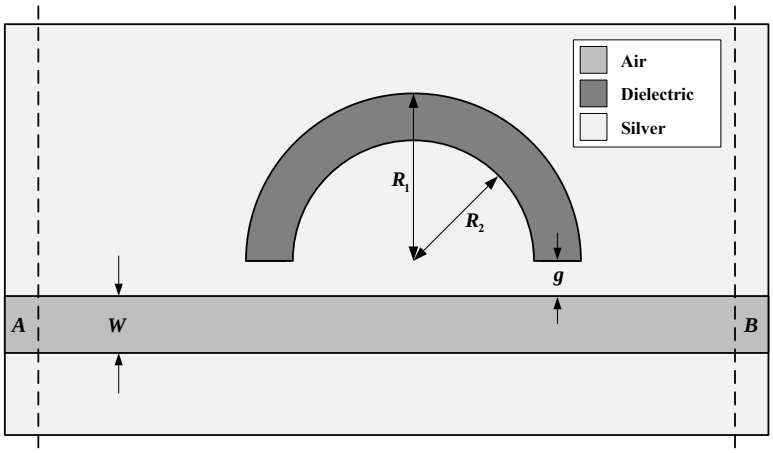

Figure 4.34: Basic structure of plasmonic waveguide with ring-type semi-circular resonator.

4.3.2 Results and Discussions

Disc-Type Semi-Circular Resonator

Initially, the geometric parameters are set as the gap between the straight waveguide and the disc-type resonator g = 32 nm, and the radius of the circle of which the semi-circle is a part R = 420 nm for the numerical calculation of the sensor. The refractive index of the dielectric is varied from 1.0 to 1.02, with a step of 0.005. The transmittance for the change of wavelength of the sensor for this setup has been depicted in Fig. 4.35 for n = 1.0, n = 1.01, and n = 1.02. Two modes of notch-type transmission response are observed. The resonant wavelength shift with the refractive index has been depicted in Fig. 4.36 for different modes, and the relationship is observed to be linear.

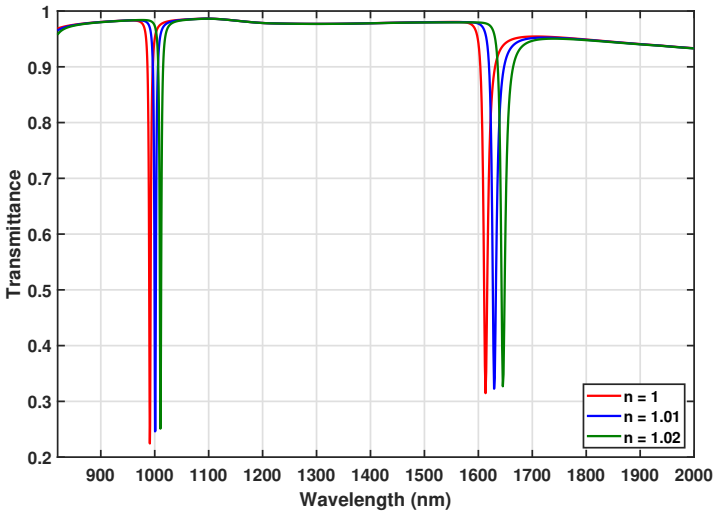

Figure 4.35: Transmittance vs wavelength for the design with disc-type semi-circular resonator for different values of n.

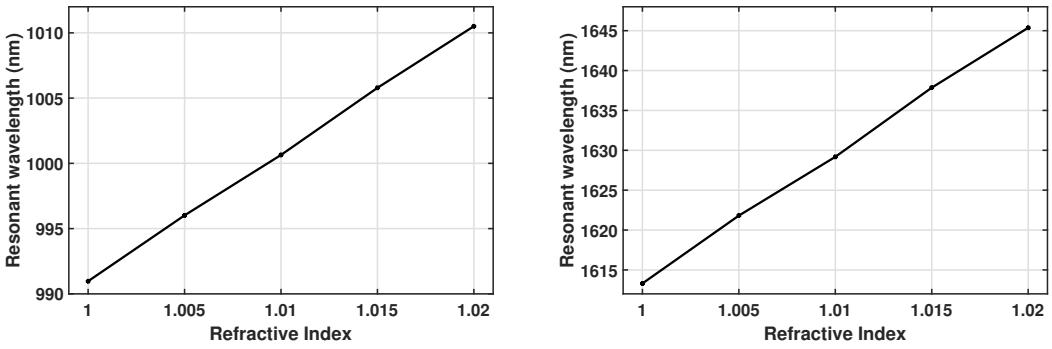

Figure 4.36: Change of resonant wavelength with the refractive index. (a) Mode 01, (b) Mode 02.

Table 4.6: Calculation of sensitivity and FOM for the design with disc-type semi-circular resonator.

n	Resonant Peak (nm)		Sensitivity (nm/RIU)		FOM	
	Mode 1	Mode 2	Mode 1	Mode 2	Mode 1	Mode 2
1	991.0	1613.3	——	——	——	——
1.005	996.0	1621.8	1008.7	1701.6	300.1	198.5
1.01	1000.6	1629.2	925.9	1472.8	278.37	168.9
1.015	1005.8	1637.9	1028.5	1735.3	309.6	199.15
1.02	1010.5	1645.4	944.2	1502.2	290.9	170.95

The calculation of sensitivity for the disc-type semi-circular shaped resonator has been shown in Table 4.6. The maximum sensitivity marked in mode 01 is 1028.5 nm/RIU, with a high FOM of 309.6 at a resonant wavelength of 1005.8 nm. For mode 02, the maximum sensitivity observed to be 1735 nm/RIU with a high FOM of 199.15 at the resonant wavelength of 1637.9 nm. The FOM of the refractive index sensor is much high for both the modes.

The gap has been varied as 14 nm, 23 nm, 32 nm, 41 nm, and 50 nm to explore the design area keeping the other parameters as R = 420 nm, n = 1.0. The transmission response of the sensor for this setup has been depicted in Fig. 4.37. The representations show that there is a small change in terms of resonant wavelength, but the extinction ratio is getting smaller with the increment of the gap g. One of the parameters for the magnitude of coupling is the gap between waveguides. As the gap increasing, transmission response shows less coupling. The performance parameters for the change of the gap g has been depicted in Fig. 4.38. The representation shows that the sensitivity is decreasing, and the FOM is increasing with the increment of the gap g. The resonant

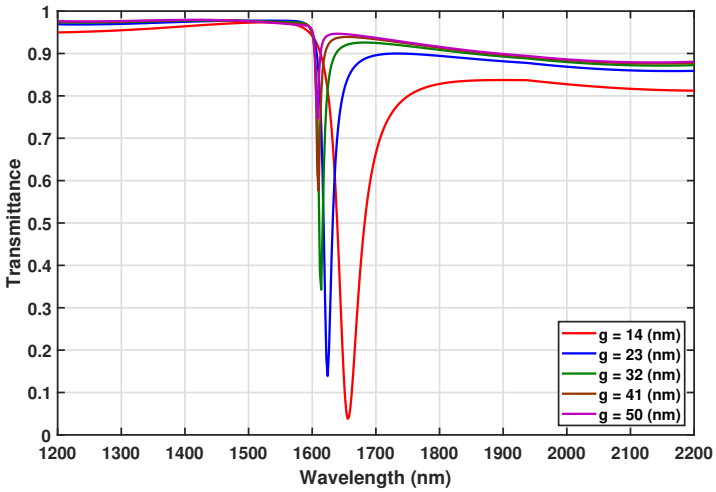

Figure 4.37: Transmittance vs wavelength for different values of gap of the design with disc-type semi-circular resonator.

wavelength observed to shift left i.e., decreasing but very small in magnitude, the ER is decreasing with a higher rate with the increment of the gap g. The maximum sensitivity achieved is 1715 nm/RIU with a FOM of 47.11 and an ER of 0.782 at a resonant wavelength of 1656 nm for g = 14 nm.

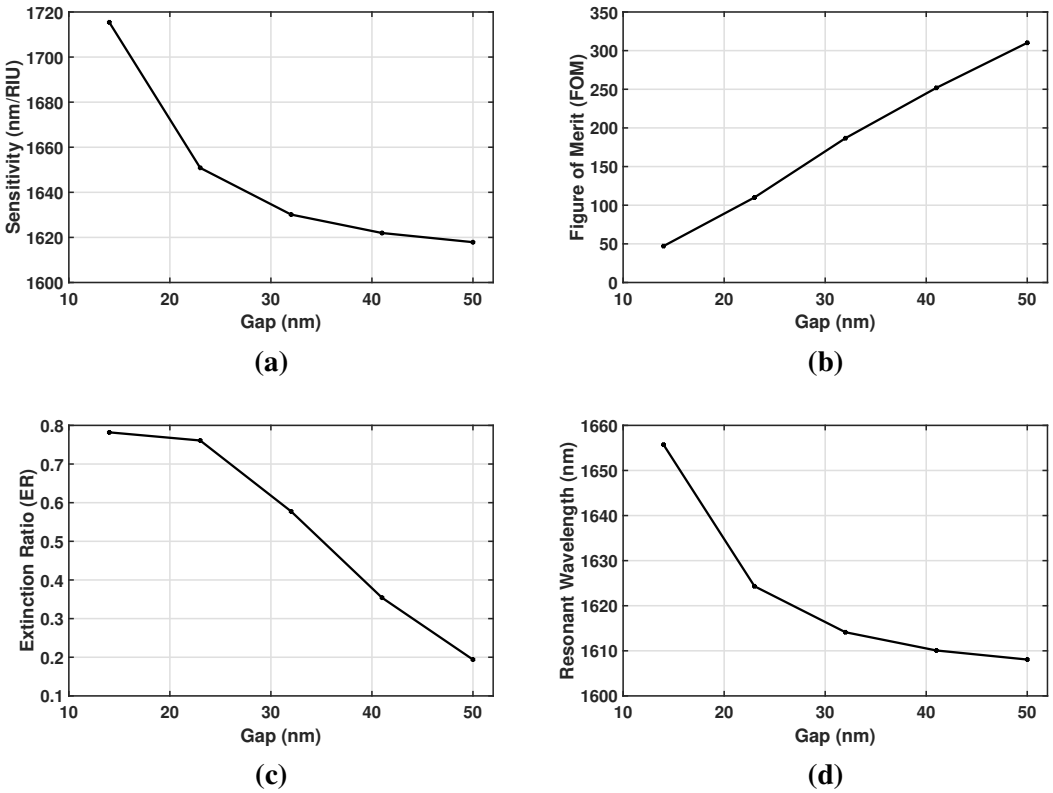

Figure 4.38: Performance parameters with the change of gap g of the RI sensor based on the disc-type pentagonal resonator. (a) Sensitivity, (b) FOM, (c) ER, and (d) Resonant Wavelength.

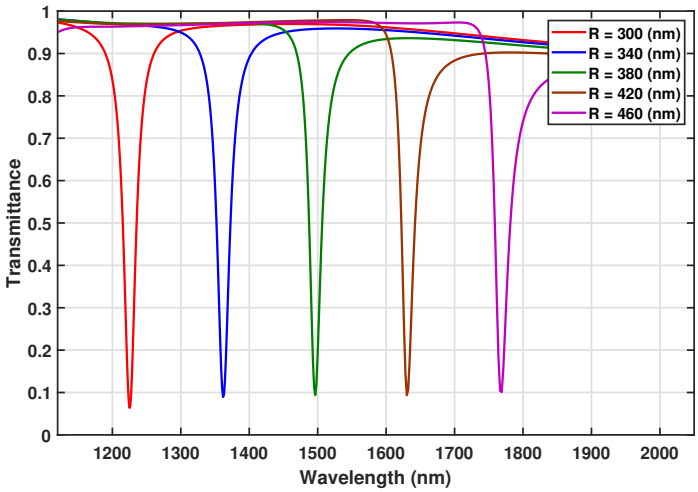

Figure 4.39: Transmittance vs wavelength for different values of radius R of the design with disc-type semi-circular resonator.

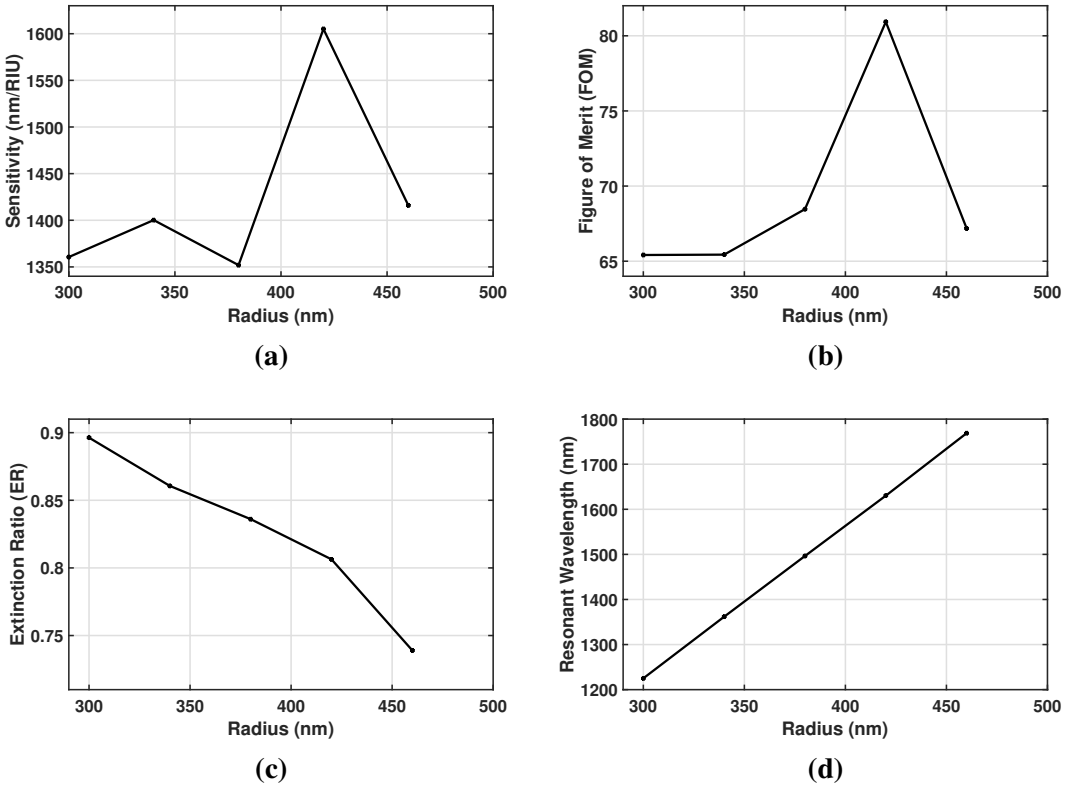

Figure 4.40: Performance parameters with the change of radius R of the RI sensor based on the disc-type pentagonal resonator. (a) Sensitivity, (b) FOM, (c) ER, and (d) Resonant Wavelength.

The radius R of the circle of which the semicircular resonator is a part, another design parameter, has been varied as 300 nm, 340 nm, 380 nm, 420 nm, and 460 nm keeping other parameters as g = 20 nm, and n = 1.0. For these parameters, the transmittance has been depicted in Fig. 4.39 and the performance parameters for the change of R

has been depicted in Fig. 4.40. The representation shows that the sensitivity and FOM profile has a spike i.e., the highest value for R = 420 nm where ER is found to be greater than 0.8. The ER is decreasing with the increment of the radius R. The resonant wavelength is shifting towards the right i.e., increasing with the increment of the radius R. The maximum sensitivity achieved is 1605 nm/RIU with a high FOM of 80.93 for radius R = 420 nm at resonant wavelength of 1630 nm.

Ring-Type Semi-Circular Resonator

The numerical calculation of the transmittance of the sensor with the ring-type resonator has been performed using COMSOL Multiphysics for the refractive index change from n = 1.0 to n = 1.02 with the step of 0.005. The geometric parameters are set as the gap between the straight waveguide and the resonator g = 20 nm, the radius of the circle of which the outer semicircle is a part R_1 = 235 nm, and the width of the ring of the resonator W_2 = 85 nm. With these parameters, the calculated transmittance with the change of wavelength has been depicted in Fig. 4.41 for n = 1.0, n = 1.01, and n = 1.02 where only single-mode transmittance is observed. The resonant shift with the change of refractive index has been depicted in Fig.4.42, which shows a linear relationship.

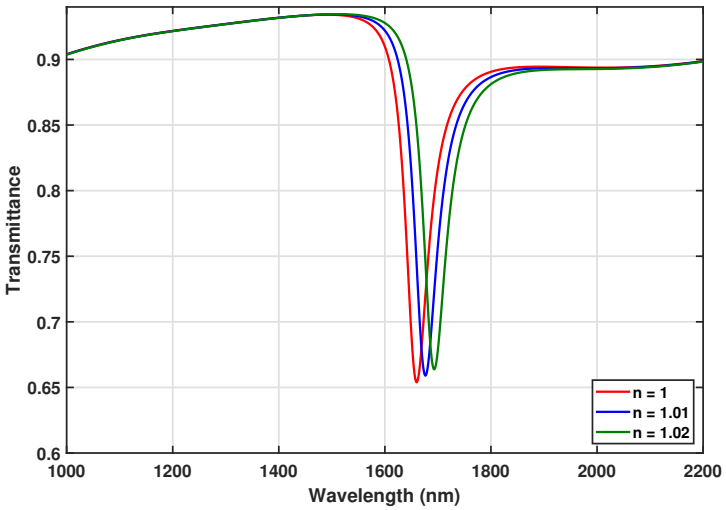

Figure 4.41: Transmittance vs wavelength for the design with ring-type semi-circular resonator for different values of n.

The calculation of sensitivity for the ring-type semi-circular shaped resonator has been shown in Table 4.7. The representation shows that maximum sensitivity is 1684.9 nm/RIU with an FOM of 36.3 at resonant wavelength of 1693 nm.

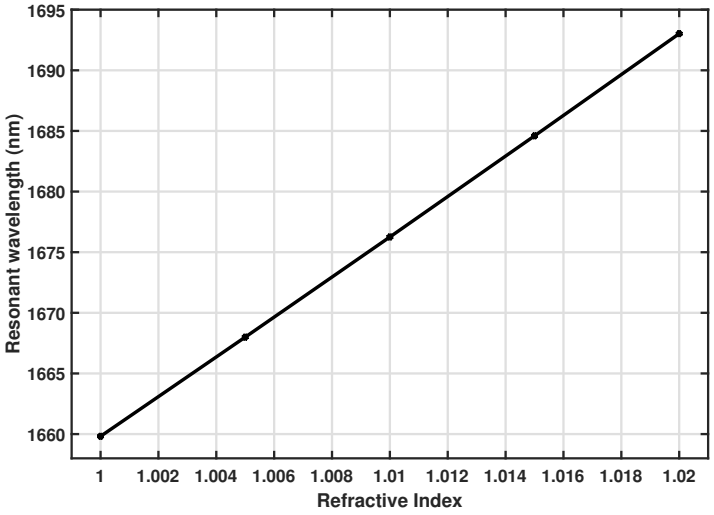

Figure 4.42: Change of resonant wavelength with the refractive index.

Table 4.7: Calculation of sensitivity and FOM for the design with ring-type semi-circular resonator.

n	Resonant Peak (nm)	Sensitivity (nm/RIU)	FOM
1	1659.8	——	——
1.005	1668.0	1635.6	35.9
1.01	1676.3	1651.8	36.1
1.015	1684.6	1668.2	36.3
1.02	1693.0	1684.9	36.3

To explore the design area, first the gap g is varied as 5 nm, 14 nm, 23 nm, 32 nm, and 41 nm keeping the other parameters as R = 235 nm, W_2 = 85 nm, and n = 1.0. The transmission response of the sensor for this setup has been depicted in Fig. 4.43 for the change in wavelength and the performance parameters has been depicted in Fig. 4.44. The sensitivity, the ER, and the resonant wavelength are decreasing with the increment of the gap g, but the FOM is increasing with the increment of gap g.

The radius R of the circle of which the outer semicircle is a part is varied as 171 nm, 192 nm, 213 nm, 234 nm, 255 nm, 276 nm, and 297 nm keeping other parameters as g = 20 nm, W_2 = 85 nm, and n = 1.0. The transmittance has been depicted in Fig. 4.45 for the change of wavelength. This representation will be more clear when we will look into the performance parameters, which has been depicted in Fig. 4.46. The sensitivity shows increment, and the ER is decreasing with the increase of the radius R. The resonant wavelength is shifting to the right i.e., increasing with the increment of the radius R, and the FOM is showing a peak at R = 235 nm.

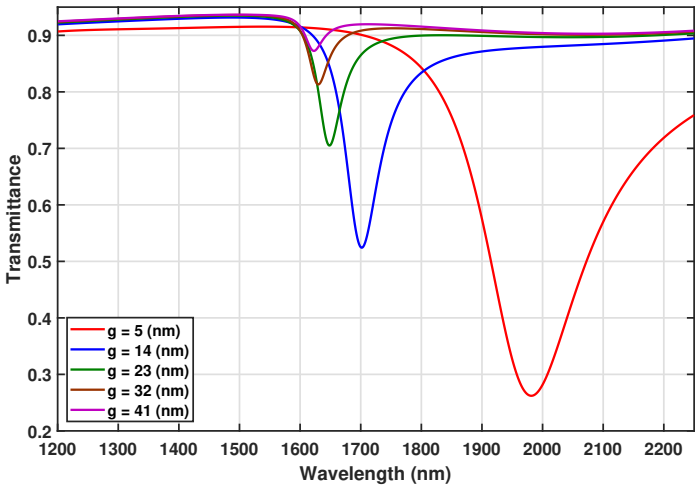

Figure 4.43: Transmittance vs wavelength for different values of gap of the design with ring-type semi-circular resonator.

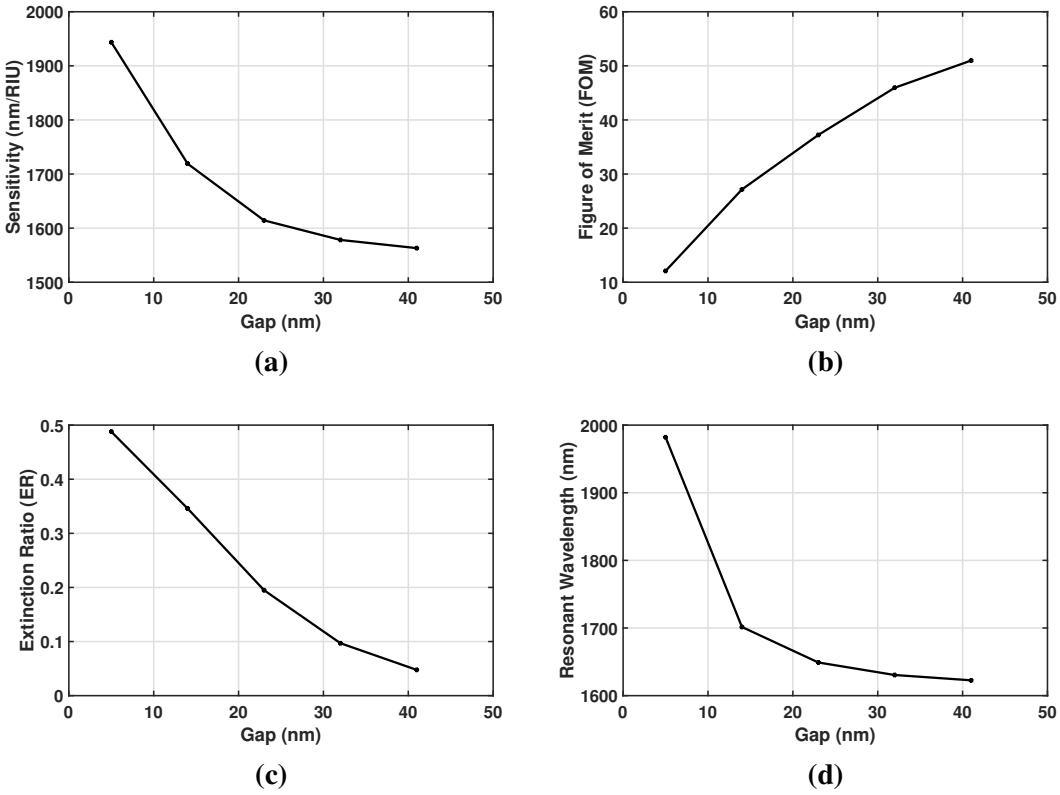

Figure 4.44: Performance parameters with the change of gap of the RI sensor based on the ring-type pentagonal resonator. (a) Sensitivity, (b) FOM, (c) ER, and (d) Resonant Wavelength.

Finally, the width of the ring of the resonator W_2 has been varied as 48 nm, 67 nm, 86 nm, 105 nm, 124 nm, 143 nm, 162 nm, 161 nm, 181 nm and 200 nm keeping the other parameters as g = 15 nm, R = 235 nm, and n = 1.0. The transmission response corresponding to this setup has been depicted in Fig. 4.47 and the performance param-

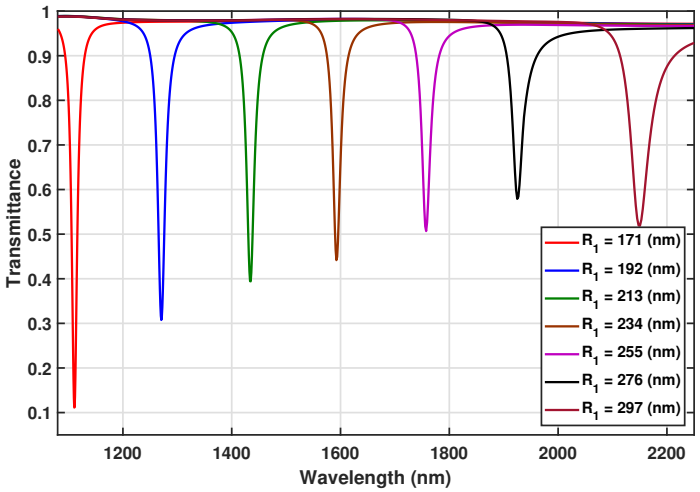

Figure 4.45: Transmittance vs wavelength for different values of radius of the design with ring-type semi-circular resonator.

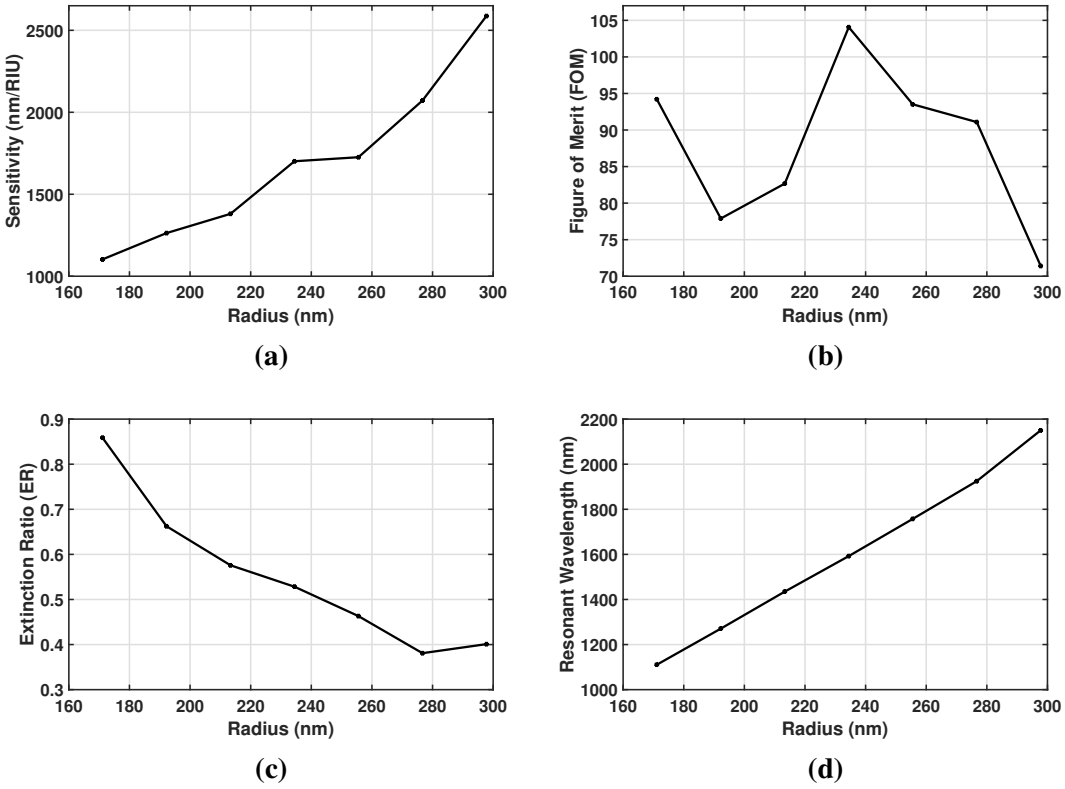

Figure 4.46: Performance parameters with the change of radius of the RI sensor based on the ring-type pentagonal resonator. (a) Sensitivity, (b) FOM, (c) ER, and (d) Resonant Wavelength.

eters change with the increment of the width W_2 has been depicted in Fig. 4.48. The sensitivity and the FOM are decreasing, but the ER is increasing with the increment of the width W_2. The resonant wavelength is shifting to the left with the increment of the width W_2.

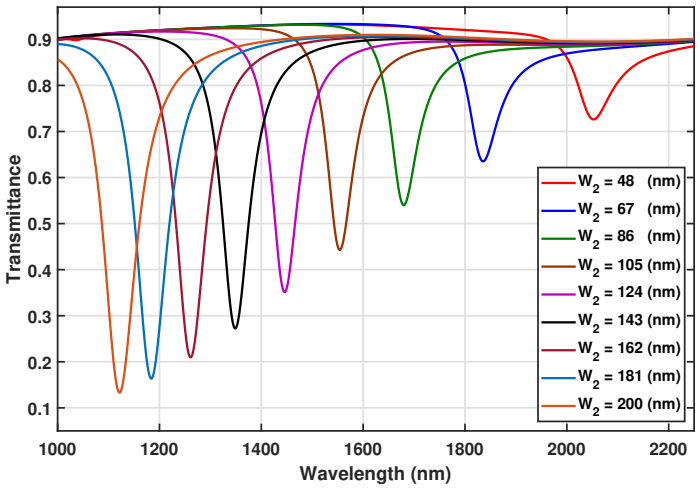

Figure 4.47: Transmittance vs wavelength for different values of width of the design with ring-type semi-circular resonator.

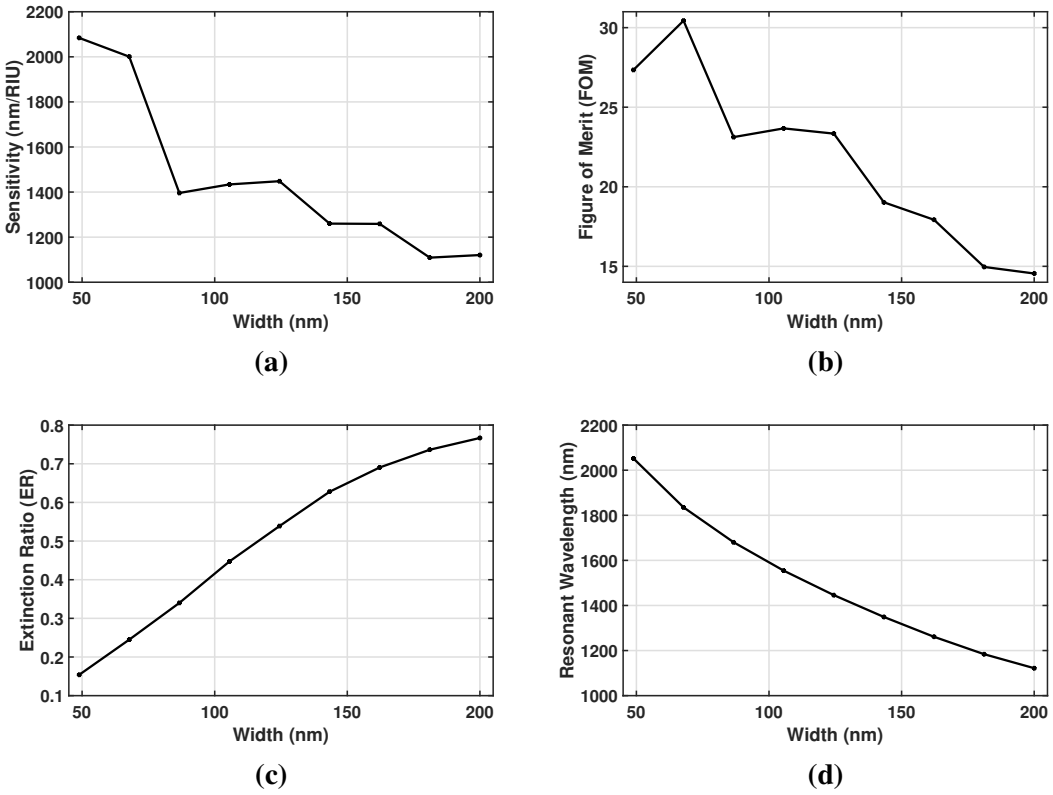

Figure 4.48: Performance parameters with the change of width of the RI sensor based on the ring-type pentagonal resonator. (a) Sensitivity, (b) FOM, (c) ER, and (d) Resonant Wavelength.

With the consideration of all the cases, a maximum sensitivity of 2587 nm/RIU has been achieved with a FOM of 71.4 for the design parameters g = 20 nm, R = 297 nm, and W_2 = 85 nm at resonant wavelength peak of 2150 nm. The maximum FOM of 104.1 has been achieved with the sensitivity of 1701 nm/RIU for the design parameters

g = 20 nm, R = 235 nm, and W_2 = 85 nm at the resonant wavelength peak of 1592 nm. The comparison of the performance parameters and design parameters of the disc-type and ring-type semi-circular resonator for maximum sensitivity and maximum FOM have been represented in Table 4.8.

Table 4.8: Comparison of the performance and design parameters of the disc-type and ring-type semi-circular resonator for the maximum sensitivity and the maximum FOM.

		Disc-type Resonator		**Ring-type Resonator**	
		For Max Sensitivity	For Max FOM	For Max Sensitivity	For Max FOM
Performance Parameters	Sensitivity (nm/RIU)	1715	1618	2587	1701
	FOM	47.11	310.1	71.4	104.1
	ER	0.782	0.2	0.4	0.53
	Resonant wavelength (nm)	1656	1608	2150	1592
Design Parameters	g (nm)	14	50	20	20
	R (nm)	420	420	297	235
	W_2 (nm)	N/A	N/A	85	85

4.3.3 Conclusion

In terms of sensitivity, ring-type semi-circular resonator design is preferable, but in terms of the FOM, disc-type resonator design will dominate. The maximum sensitivity achieved for the ring-type resonator is 2587 nm/RIU, and a maximum FOM of 310.1 has been achieved for the disc-type resonator.

4.4 Applications

4.4.1 As a Biosensor

In section 1.4: Literature Review, it has been shown that most of the biological specimen have their refractive index between 1.32 to 1.40. Here the proposed sensors are tested for that range of refractive indices. The transmittance versus wavelength for the bio-molecules with the sensor having triangular (ring-type) resonator has been depicted in Fig. 4.49. The maximum sensitivity investigated to be 2011.7 nm/RIU with a FOM of 25.5 which are quite high for a sensor.

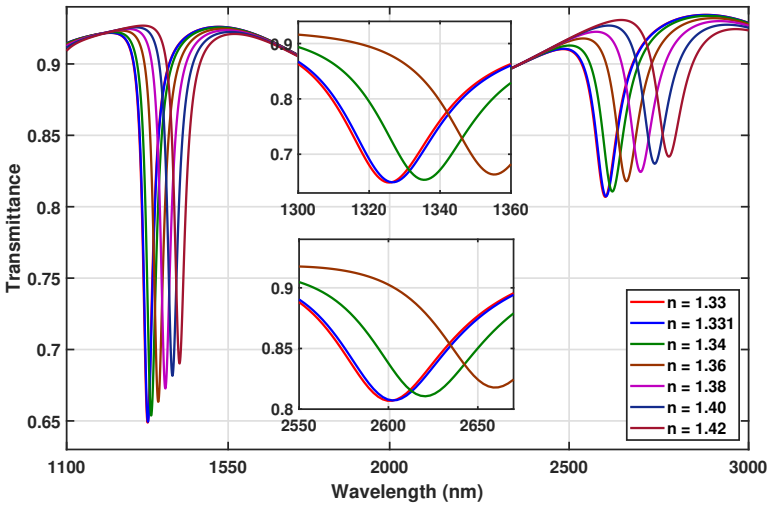

Figure 4.49: Transmittance versus wavelength of the sensor having triangular (ring-type) resonator for the different bio-molecules.

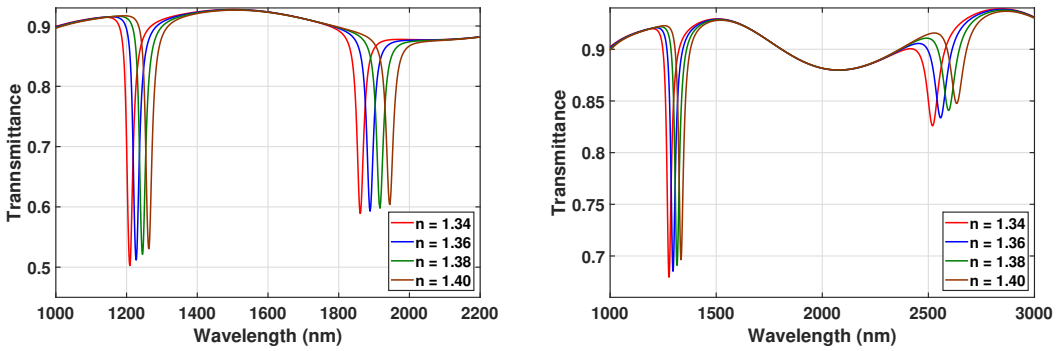

(a) **(b)**

Figure 4.50: Transmittance versus wavelength of the sensor having pentagonal resonator for the different bio-molecules. (a) Disc-type, (b) ring-type.

In Fig. 4.50, the transmittance versus wavelength for the bio-molecules with the sensor having pentagonal resonator both the disc-type and the ring-type has been shown. A

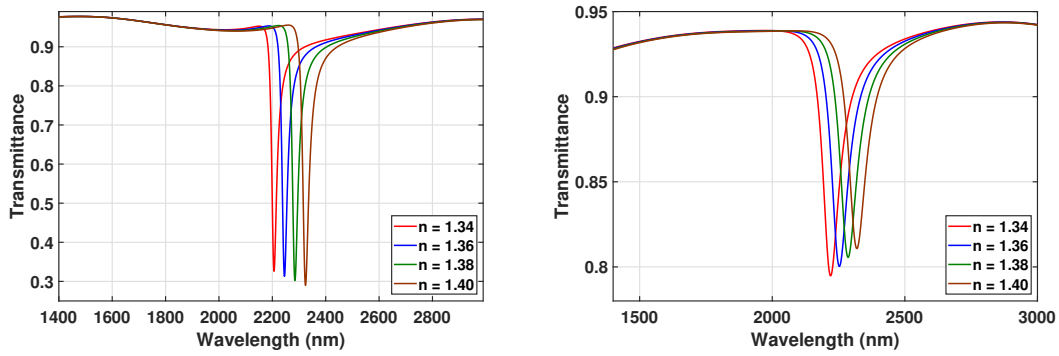

Figure 4.51: Transmittance versus wavelength of the sensor having semicircular resonator for the different bio-molecules. (a) Disc-type, (b) ring-type.

maximum sensitivity of 1517.8 nm/RIU with FOM 70.24 for the disc-type resonator and 1918.3 nm/RIU with FOM 28.6 for the ring-type resonator have been investigated for mode 02 of the sensors.

Finally, the transmittance versus wavelength for the bio-molecules with the sensor having semicircular resonator both the disc-type and the ring-type has been depicted in Fig. 4.51. A maximum sensitivity of 1996.1 nm/RIU with FOM 83.1 for the disc-type resonator and 1668.8 nm/RIU with FOM 22.6 for the ring-type resonator have been investigated for the single mode of the sensors.

4.4.2 As a Filter

As it is mentioned that the filter property, basically, depends on the quality factor, the quality factor of different sensors has been shown. All the proposed designs have notch-type transmission spectrum i.e., will work as a notch filter.

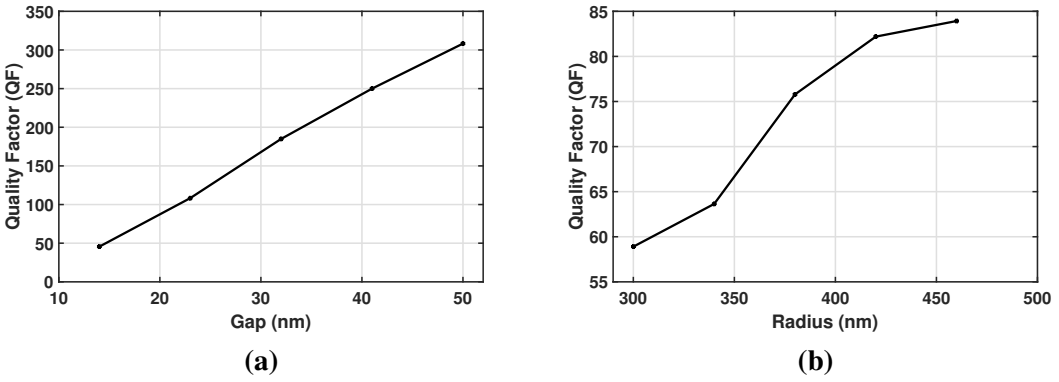

Figure 4.52: Quality Factor with the change of design parameters of the design with disc-type semi-circular resonator. (a) With the change of gap, (b) with the change of radius.

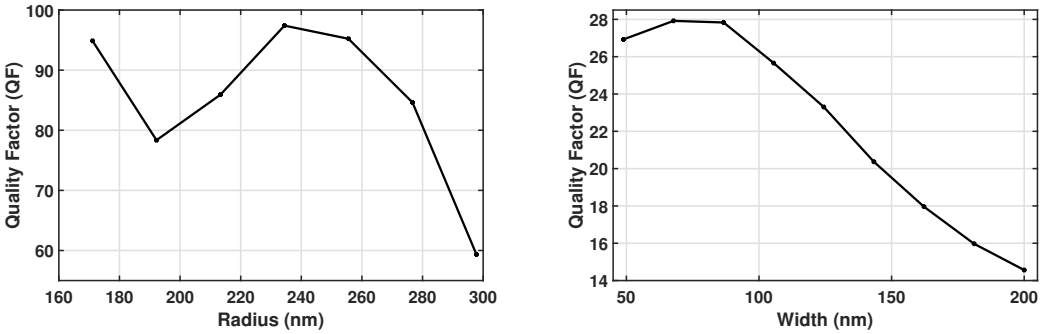

Figure 4.53: Quality Factor with the change of design parameters of the design with ring-type semi-circular resonator. (a) With the change of radius, (b) with the change of width.

The quality factor with the change of design parameters (gap, radius) of the disc-type semi-circular resonator has been depicted in Fig. 4.52. The quality factor with the change of design parameters (radius, width) of the ring-type semi-circular resonator has been depicted in Fig. 4.53. A maximum quality factor of 310, which is high enough, has been obtained for the sensor design with the disc-type semi-circular resonator. Similarly, for the designs with triangular and pentagonal resonator can be represented as good notch filters.

Chapter 5

Conclusions and Future Works

5.1 Conclusions

An investigation is performed in search of a refractive index sensor which has improved performance. Sensitivity is the change in resonant wavelength for the unit change in the refractive index. It determines how well a sensor can detect. It is easier to detect a resonance shift for the narrow linewidth of the spectrum. FOM is the measure of how well the sensor is in terms of both the sensitivity and narrow linewidth. ER is the difference between the maximum and minimum transmittance value.

The plasmonic sensors proposed here have been tuned by evaluating these key parameters like sensitivity, FOM, ER, etc. Three different designs of the resonator have been investigated, namely triangular, pentagonal, and semi-circular resonator. The resonators can be of disc-type and ring-type. Each of them has been investigated with their design parameters like radius, length, and gap of different waveguides present in the sensor.

The sensitivity and FOM of the proposed sensors and a few other sensors reported in the literature have been presented in Table 5.1. More other sensors with MIM configuration have been shown previously in Table 1.2 of Chapter 1: Literature Review part. The comparison shows that the performance parameters of the proposed sensors are high enough compared to the different sensors reported in the literature. A maximum sensitivity of 2713 nm/RIU and a maximum FOM of 310 has been found for the sensor designs with the ring-type side coupled triangular resonator and disc-type side coupled semi-circular resonator respectively. Two of the sensors from the literature shows better performance in terms of sensitivity only. However, the proposed sensors in this thesis have better performance in terms of sensitivity and FOM collectively.

Table 5.1: Comparison of the proposed sensor with refractive index sensors of MIM configuration reported in the literature with Silver as metal.

	Proposed Sensor	Year	Sensitivity	FOM
01	Zou *et. al.* [47]	2015	3960	—
02	Rakhshani *et. al.* [51]	2016	4270	22
03	Rakhshani *et. al.* [8]	2017	2320	—
04	Rakhshani *et. al.* [56]	2017	2610	52
05	Yi *et. al.* [63]	2018	1700	60.7
06	Zafar *et. al.* [22]	2018	1100	224
07	Butt *et. al.* [70]	2019	1367	25
08	Zhang *et. al.* [69]	2019	1268	280
09	Bazgir *et. al.* [73]	2020	1260	120
10	Rakhshani *et. al.* [72]	2020	1380	104
11	Proposed Disc-type triangular resonator	2020	1203	63.5
12	Proposed Ring-type triangular resonator	2020	2713	35.1
13	Proposed Disc-type pentagonal resonator	2020	1669	44.21
14	Proposed Ring-type pentagonal resonator	2020	2325	46
15	Proposed Disc-type semi-circular resonator	2020	1618	310
16	Proposed Ring-type semi-circular resonator	2020	2587	71.4

The sensors can sense the refractive index change of different gases (n = 1 to n = 1.03), which makes it suitable for gas sensors. The sensors can sense the refractive index change of water, different proteins, viruses, blood groups, blood components, and cancer cells, thus being used as a biosensor. Moreover, these can be represented as good notch filters for having high quality factor. The compact and simple design of the sensors also makes it suitable to be integrated into bio-implantable on-chip sensing applications.

5.2 Future Works

The thesis presents only a few designs of the refractive index sensor with MIM configuration and silver as a metal. Multiple future goals can be obtained with the current advancements of the work.

- The design area can be explored to get devices with compact design and better performance.
- Reverse designing is a field to explore. The deep neural network integration is one of the options for reverse designing, which can reduce the considerable computational cost during the simulation.
- Different materials can be investigated for these sensors to get better performance.

REFERENCES

[1] S. A. Maier, "Surface plasmon polaritons at metal/insulator interfaces", in *Plasmonics: Fundamentals and Applications*, Springer, 2007, pp. 21–37.

[2] W. L. Barnes, A. Dereux, and T. W. Ebbesen, "Surface plasmon subwavelength optics", *nature*, vol. 424, no. 6950, p. 824, 2003.

[3] D. K. Gramotnev and S. I. Bozhevolnyi, "Plasmonics beyond the diffraction limit", *Nature photonics*, vol. 4, no. 2, p. 83, 2010.

[4] S. A. Maier, "Plasmonics: The promise of highly integrated optical devices", *IEEE Journal of selected topics in Quantum Electronics*, vol. 12, no. 6, pp. 1671–1677, 2006.

[5] M. L. Brongersma, R. Zia, and J. Schuller, "Plasmonics–the missing link between nanoelectronics and microphotonics", *Applied Physics A*, vol. 89, no. 2, pp. 221–223, 2007.

[6] M. Wang, M. Zhang, Y. Wang, R. Zhao, and S. Yan, "Fano resonance in an asymmetric mim waveguide structure and its application in a refractive index nanosensor", *Sensors*, vol. 19, no. 4, p. 791, 2019.

[7] X. Zhang, Y. Qi, P. Zhou, H. Gong, B. Hu, and C. Yan, "Refractive index sensor based on fano resonances in plasmonic waveguide with dual side-coupled ring resonators", *Photonic Sensors*, vol. 8, no. 4, pp. 367–374, 2018.

[8] M. R. Rakhshani and M. A. Mansouri-Birjandi, "High sensitivity plasmonic refractive index sensing and its application for human blood group identification", *Sensors and Actuators B: Chemical*, vol. 249, pp. 168–176, 2017.

[9] Y. Kong, R. Lin, W. Qian, Q. Wei, C. Liu, and S. Wang, "Active dual-wavelength optical switch-based plasmonic demultiplexer using metal-kerr nonlinear material-metal waveguide", *IEEE Photonics Journal*, vol. 9, no. 4, pp. 1–8, 2017.

[10] M. Danaie and A. Shahzadi, "Design of a high-resolution metal–insulator–metal plasmonic refractive index sensor based on a ring-shaped si resonator", *Plasmonics*, pp. 1–13, 2019.

[11] P. Sharma and D. K. Vishwakarma, "Long range multilayer hybrid plasmonic waveguide components and integrated circuit", *IEEE Transactions on Nanotechnology*, vol. 18, pp. 940–947, 2019.

[12] J. H. Zhu, Q. J. Wang, P. Shum, and X. G. Huang, "A nanoplasmonic high-pass wavelength filter based on a metal-insulator-metal circuitous waveguide", *IEEE transactions on nanotechnology*, vol. 10, no. 6, pp. 1357–1361, 2011.

[13] M. Z. U. Rahman, K. M. Krishna, K. K. Reddy, M. V. Babu, S. S. Mirza, and S. Y. Fathima, "Ultra-wide-band band-pass filters using plasmonic mim waveguide-based ring resonators", *IEEE Photonics Technology Letters*, vol. 30, no. 19, pp. 1715–1718, 2018.

[14] P. Sharma and V. D. Kumar, "All optical logic gates using hybrid metal insulator metal plasmonic waveguide", *IEEE Photonics Technology Letters*, vol. 30, no. 10, pp. 959–962, 2018.

[15] J. Shibayama, H. Kawai, J. Yamauchi, and H. Nakano, "Analysis of a 3d mim waveguide-based plasmonic demultiplexer using the trc-fdtd method", *Optics Communications*, vol. 452, pp. 360–365, 2019.

[16] Y.-Y. Xie, C. He, J.-C. Li, T.-T. Song, Z.-D. Zhang, and Q.-R. Mao, "Theoretical investigation of a plasmonic demultiplexer in mim waveguide crossing with multiple side-coupled hexagonal resonators", *IEEE Photonics Journal*, vol. 8, no. 5, pp. 1–12, 2016.

[17] M. B. Heydari, M. Asgari, and N. Jafari, "Novel analytical model for nanocoupler between metal–insulator–metal plasmonic and dielectric slab waveguides", *Optical and Quantum Electronics*, vol. 50, no. 12, p. 432, 2018.

[18] Y. Yu, J. Si, Y. Ning, M. Sun, and X. Deng, "Plasmonic wavelength splitter based on a metal–insulator–metal waveguide with a graded grating coupler", *Optics letters*, vol. 42, no. 2, pp. 187–190, 2017.

[19] S. Fathpour and B. Jalali, *Silicon photonics for telecommunications and biomedicine*. CRC Press, 2011.

[20] Y. Kurokawa and H. T. Miyazaki, "Metal-insulator-metal plasmon nanocavities: Analysis of optical properties", *Physical Review B*, vol. 75, no. 3, p. 035 411, 2007.

[21] T. Cole, A. Kathman, S. Koszelak, and A. McPherson, "Determination of local refractive index for protein and virus crystals in solution by mach-zehnder interferometry", *Analytical biochemistry*, vol. 231, no. 1, pp. 92–98, 1995.

[22] R. Zafar, S. Nawaz, G. Singh, A. d'Alessandro, and M. Salim, "Plasmonics-based refractive index sensor for detection of hemoglobin concentration", *IEEE Sensors Journal*, vol. 18, no. 11, pp. 4372–4377, 2018.

[23] S. K. Chamoli, S. Singh, and C. Guo, "Design of extremely sensitive refractive index sensors in infrared for blood glucose detection", *IEEE Sensors Journal*, 2020.

[24] M. A. Jabin, K. Ahmed, M. J. Rana, B. K. Paul, M. Islam, D. Vigneswaran, and M. S. Uddin, "Surface plasmon resonance based titanium coated biosensor for cancer cell detection", *IEEE Photonics Journal*, vol. 11, no. 4, pp. 1–10, 2019.

[25] K. Ahmed, F. Ahmed, S. Roy, B. K. Paul, M. N. Aktar, D. Vigneswaran, and M. S. Islam, "Refractive index-based blood components sensing in terahertz spectrum", *IEEE Sensors Journal*, vol. 19, no. 9, pp. 3368–3375, 2019.

[26] S.-Y. Tseng, S.-Y. Li, S.-Y. Yi, A. Y. Sun, D.-Y. Gao, and D. Wan, "Food quality monitor: Paper-based plasmonic sensors prepared through reversal nanoimprinting for rapid detection of biogenic amine odorants", *ACS applied materials & interfaces*, vol. 9, no. 20, pp. 17 306–17 316, 2017.

[27] M. J. Al Mahmod, R. Hyder, and M. Z. Islam, "A highly sensitive metal–insulator–metal ring resonator-based nanophotonic structure for biosensing applications", *IEEE Sensors Journal*, vol. 18, no. 16, pp. 6563–6568, 2018.

[28] D. N. Batchelder and J. P. Willson, *Optical surface plasmon sensor device*, US Patent 4,844,613, 1989.

[29] R. Garabedian, C. Gonzalez, J. Richards, A. Knoesen, R. Spencer, S. Collins, and R. Smith, "Microfabricated surface plasmon sensing system", *Sensors and Actuators A: Physical*, vol. 43, no. 1-3, pp. 202–207, 1994.

[30] S. Nelson, K. S. Johnston, and S. S. Yee, "High sensitivity surface plasmon resonace sensor based on phase detection", *Sensors and actuators B: Chemical*, vol. 35, no. 1-3, pp. 187–191, 1996.

[31] J. Homola, J. Čtyrokỳ, M. Skalskỳ, J. Hradilova, and P. Kolářová, "A surface plasmon resonance based integrated optical sensor", *Sensors and Actuators B: Chemical*, vol. 39, no. 1-3, pp. 286–290, 1997.

[32] M. Naya and T. Akimoto, *Surface plasmon sensor*, US Patent 5,917,608, 1999.

[33] J. Čtyrokỳ, J. Homola, P. Lambeck, S. Musa, H. Hoekstra, R. Harris, J. Wilkinson, B. Usievich, and N. Lyndin, "Theory and modelling of optical waveguide sensors utilising surface plasmon resonance", *Sensors and Actuators B: Chemical*, vol. 54, no. 1-2, pp. 66–73, 1999.

[34] J. J. Mock, D. R. Smith, and S. Schultz, "Local refractive index dependence of plasmon resonance spectra from individual nanoparticles", *Nano letters*, vol. 3, no. 4, pp. 485–491, 2003.

[35] E. M. Larsson, J. Alegret, M. Käll, and D. S. Sutherland, "Sensing characteristics of nir localized surface plasmon resonances in gold nanorings for application as ultrasensitive biosensors", *Nano letters*, vol. 7, no. 5, pp. 1256–1263, 2007.

[36] A. G. Brolo, R. Gordon, B. Leathem, and K. L. Kavanagh, "Surface plasmon sensor based on the enhanced light transmission through arrays of nanoholes in gold films", *Langmuir*, vol. 20, no. 12, pp. 4813–4815, 2004.

[37] A. Lesuffleur, H. Im, N. C. Lindquist, and S.-H. Oh, "Periodic nanohole arrays with shape-enhanced plasmon resonance as real-time biosensors", *Applied Physics Letters*, vol. 90, no. 24, p. 243 110, 2007.

[38] X.-P. Jin, X.-G. Huang, J. Tao, X.-S. Lin, and Q. Zhang, "A novel nanometeric plasmonic refractive index sensor", *IEEE transactions on nanotechnology*, vol. 9, no. 2, pp. 134–137, 2010.

[39] J. Becker, A. Trügler, A. Jakab, U. Hohenester, and C. Sönnichsen, "The optimal aspect ratio of gold nanorods for plasmonic bio-sensing", *Plasmonics*, vol. 5, no. 2, pp. 161–167, 2010.

[40] S.-H. Kwon, "Deep subwavelength-scale metal–insulator–metal plasmonic disk cavities for refractive index sensors", *IEEE Photonics Journal*, vol. 5, no. 1, pp. 4 800 107–4 800 107, 2013.

[41] L. Xu, S. Wang, and L. Wu, "Refractive index sensing based on plasmonic waveguide side coupled with bilaterally located double cavities", *IEEE Transactions on Nanotechnology*, vol. 13, no. 5, pp. 875–880, 2014.

[42] M. Bahramipanah, M. S. Abrishamian, S. A. Mirtaheri, and J.-M. Liu, "Ultracompact plasmonic loop–stub notch filter and sensor", *Sensors and Actuators B: Chemical*, vol. 194, pp. 311–318, 2014.

[43] B. Ni, X. Chen, D. Xiong, H. Liu, G. Hua, J. Chang, J. Zhang, and H. Zhou, "Infrared plasmonic refractive index-sensitive nanosensor based on electromagnetically induced transparency of waveguide resonator systems", *Optical and Quantum Electronics*, vol. 47, no. 6, pp. 1339–1346, 2015.

[44] Y.-Y. Xie, Y.-X. Huang, W.-L. Zhao, W.-H. Xu, and C. He, "A novel plasmonic sensor based on metal–insulator–metal waveguide with side-coupled hexagonal cavity", *IEEE Photonics Journal*, vol. 7, no. 2, pp. 1–12, 2015.

[45] S.-B. Yan, L. Luo, C.-Y. Xue, and Z.-D. Zhang, "A refractive index sensor based on a metal-insulator-metal waveguide-coupled ring resonator", *Sensors*, vol. 15, no. 11, pp. 29 183–29 191, 2015.

[46] R. Zafar and M. Salim, "Enhanced figure of merit in fano resonance-based plasmonic refractive index sensor", *IEEE Sensors Journal*, vol. 15, no. 11, pp. 6313–6317, 2015.

[47] S. Zou, F. Wang, R. Liang, L. Xiao, and M. Hu, "A nanoscale refractive index sensor based on asymmetric plasmonic waveguide with a ring resonator: A review", *IEEE Sensors Journal*, vol. 15, no. 2, pp. 646–650, 2014.

[48] Z. Chen, L. Yu, L. Wang, G. Duan, Y. Zhao, and J. Xiao, "A refractive index nanosensor based on fano resonance in the plasmonic waveguide system", *IEEE Photonics Technology Letters*, vol. 27, no. 16, pp. 1695–1698, 2015.

[49] L. Chen, Y. Liu, Z. Yu, D. Wu, R. Ma, Y. Zhang, and H. Ye, "Numerical analysis of a near-infrared plasmonic refractive index sensor with high figure of merit based on a fillet cavity", *Optics express*, vol. 24, no. 9, pp. 9975–9983, 2016.

[50] F. Chen and D. Yao, "Realizing of plasmon fano resonance with a metal nanowall moving along mim waveguide", *Optics Communications*, vol. 369, pp. 72–78, 2016.

[51] M. R. Rakhshani and M. A. Mansouri-Birjandi, "High-sensitivity plasmonic sensor based on metal–insulator–metal waveguide and hexagonal-ring cavity", *IEEE Sensors Journal*, vol. 16, no. 9, pp. 3041–3046, 2016.

[52] T. Wu and W. Cao, "A multifunction filter based on plasmonic waveguide with double-nanodisk-shaped resonators", *Optik*, vol. 127, no. 20, pp. 8976–8982, 2016.

[53] Z. Zhang, L. Luo, C. Xue, W. Zhang, and S. Yan, "Fano resonance based on metal-insulator-metal waveguide-coupled double rectangular cavities for plasmonic nanosensors", *Sensors*, vol. 16, no. 5, p. 642, 2016.

[54] X. Zhang, M. Shao, and X. Zeng, "High quality plasmonic sensors based on fano resonances created through cascading double asymmetric cavities", *Sensors*, vol. 16, no. 10, p. 1730, 2016.

[55] A. Akhavan, H. Ghafoorifard, S. Abdolhosseini, and H. Habibiyan, "Plasmon-induced transparency based on a triangle cavity coupled with an ellipse-ring resonator", *Applied optics*, vol. 56, no. 34, pp. 9556–9563, 2017.

[56] M. R. Rakhshani and M. A. Mansouri-Birjandi, "Utilizing the metallic nanorods in hexagonal configuration to enhance sensitivity of the plasmonic racetrack resonator in sensing application", *Plasmonics*, vol. 12, no. 4, pp. 999–1006, 2017.

[57] Y. Tang, Z. Zhang, R. Wang, Z. Hai, C. Xue, W. Zhang, and S. Yan, "Refractive index sensor based on fano resonances in metal-insulator-metal waveguides coupled with resonators", *Sensors*, vol. 17, no. 4, p. 784, 2017.

[58] J. Zhou, H. Chen, Z. Zhang, J. Tang, J. Cui, C. Xue, and S. Yan, "Transmission and refractive index sensing based on fano resonance in mim waveguide-coupled trapezoid cavity", *AIP Advances*, vol. 7, no. 1, p. 015 020, 2017.

[59] C. Wu, H. Ding, T. Huang, X. Wu, B. Chen, K. Ren, and S. Fu, "Plasmon-induced transparency and refractive index sensing in side-coupled stub-hexagon resonators", *Plasmonics*, vol. 13, no. 1, pp. 251–257, 2018.

[60] A. Akhavan, H. Ghafoorifard, S. Abdolhosseini, and H. Habibiyan, "Metal–insulator–metal waveguide-coupled asymmetric resonators for sensing and slow light applications", *IET Optoelectronics*, vol. 12, no. 5, pp. 220–227, 2018.

[61] S. Ghorbani, M. A. Dashti, and M. Jabbari, "Plasmonic nano-sensor based on metal-dielectric-metal waveguide with the octagonal cavity ring", *Laser Physics*, vol. 28, no. 6, p. 066 208, 2018.

[62] M. R. Rakhshani and M. A. Mansouri-Birjandi, "Engineering hexagonal array of nanoholes for high sensitivity biosensor and application for human blood group detection", *IEEE Transactions on Nanotechnology*, vol. 17, no. 3, pp. 475–481, 2018.

[63] X. Yi, J. Tian, and R. Yang, "Tunable fano resonance in plasmonic mdm waveguide with a square type split-ring resonator", *Optik*, vol. 171, pp. 139–148, 2018.

[64] Z. Zhang, J. Yang, X. He, J. Zhang, J. Huang, D. Chen, and Y. Han, "Plasmonic refractive index sensor with high figure of merit based on concentric-rings resonator", *Sensors*, vol. 18, no. 1, p. 116, 2018.

[65] M. Butt, S. Khonina, and N. Kazanskiy, "Hybrid plasmonic waveguide-assisted metal–insulator–metal ring resonator for refractive index sensing", *Journal of Modern Optics*, vol. 65, no. 9, pp. 1135–1140, 2018.

[66] Z. Li, K. Wen, L. Chen, L. Lei, J. Zhou, D. Zhou, Y. Fang, and B. Wu, "Control of multiple fano resonances based on a subwavelength mim coupled cavities system", *IEEE Access*, vol. 7, pp. 59 369–59 375, 2019.

[67] X. Yang, E. Hua, M. Wang, Y. Wang, F. Wen, and S. Yan, "Fano resonance in a mim waveguide with two triangle stubs coupled with a split-ring nanocavity for sensing application", *Sensors*, vol. 19, no. 22, p. 4972, 2019.

[68] M. Butt, S. Khonina, and N. Kazanskiy, "A plasmonic colour filter and refractive index sensor applications based on metal–insulator–metal square μ-ring cavities", *Laser Physics*, vol. 30, no. 1, p. 016 205, 2019.

[69] Y. Zhang and M. Cui, "Refractive index sensor based on the symmetric mim waveguide structure", *Journal of Electronic Materials*, vol. 48, no. 2, pp. 1005–1010, 2019.

[70] M. Butt, S. Khonina, and N. Kazanskiy, "Plasmonic refractive index sensor based on metal–insulator-metal waveguides with high sensitivity", *Journal of Modern Optics*, vol. 66, no. 9, pp. 1038–1043, 2019.

[71] Y. Zhang, Y. Kuang, Z. Zhang, Y. Tang, J. Han, R. Wang, J. Cui, Y. Hou, and W. Liu, "High-sensitivity refractive index sensors based on fano resonance in the plasmonic system of splitting ring cavity-coupled mim waveguide with tooth cavity", *Applied Physics A*, vol. 125, no. 1, p. 13, 2019.

[72] M. R. Rakhshani, "Optical refractive index sensor with two plasmonic double-square resonators for simultaneous sensing of human blood groups", *Photonics and Nanostructures-Fundamentals and Applications*, vol. 39, p. 100 768, 2020.

[73] M. Bazgir, M. Jalalpour, F. B. Zarrabi, and A. S. Arezoomand, "Design of an optical switch and sensor based on a mim coupled waveguide using a dna composite", *Journal of Electronic Materials*, pp. 1–6, 2020.

[74] W. Lai, K. Wen, J. Lin, Z. Guo, Q. Hu, and Y. Fang, "Plasmonic filter and sensor based on a subwavelength end-coupled hexagonal resonator", *Applied optics*, vol. 57, no. 22, pp. 6369–6374, 2018.

[75] S. Khani, M. Danaie, and P. Rezaei, "Tunable single-mode bandpass filter based on metal–insulator–metal plasmonic coupled u-shaped cavities", *IET Optoelectronics*, 2019.

[76] W. Wei, X. Zhang, and X. Ren, "Plasmonic circular resonators for refractive index sensors and filters", *Nanoscale research letters*, vol. 10, no. 1, pp. 1–6, 2015.

[77] C. Li, S. Li, Y. Wang, R. Jiao, L. Wang, and L. Yu, "Multiple fano resonances based on plasmonic resonator system with end-coupled cavities for high-performance nanosensor", *IEEE Photonics Journal*, vol. 9, no. 6, pp. 1–9, 2017.

[78] A. D. Rakić, A. B. Djurišić, J. M. Elazar, and M. L. Majewski, "Optical properties of metallic films for vertical-cavity optoelectronic devices", *Applied optics*, vol. 37, no. 22, pp. 5271–5283, 1998.

[79] C. S. Desai and J. F. Abel, *Introduction to the finite element method; a numerical method for engineering analysis*. Van Nostrand Reinhold, 1971.

[80] N. S. Matthew, *Numerical techniques in electromagnetics*. CRC Press, 2000.

[81] O. Andersen, "Laplacian electrostatic field calculations by finite elements with automatic grid generation", *IEEE Transactions on Power Apparatus and Systems*, no. 5, pp. 1485–1492, 1973.

[82] D. G. Rabus, *Integrated ring resonators*. Springer, 2007.

[83] E. J. R. Vesseur, R. De Waele, H. Lezec, H. Atwater, F. J. Garcıˇa de Abajo, and A. Polman, "Surface plasmon polariton modes in a single-crystal au nanoresonator fabricated using focused-ion-beam milling", *Applied Physics Letters*, vol. 92, no. 8, p. 083 110, 2008.

[84] S. I. Bozhevolnyi, V. S. Volkov, E. Devaux, J.-Y. Laluet, and T. W. Ebbesen, "Channel plasmon subwavelength waveguide components including interferometers and ring resonators", *Nature*, vol. 440, no. 7083, pp. 508–511, 2006.

[85] H. Ditlbacher, J. R. Krenn, G. Schider, A. Leitner, and F. R. Aussenegg, "Two-dimensional optics with surface plasmon polaritons", *Applied Physics Letters*, vol. 81, no. 10, pp. 1762–1764, 2002.

[86] P. Nagpal, N. C. Lindquist, S.-H. Oh, and D. J. Norris, "Ultrasmooth patterned metals for plasmonics and metamaterials", *Science*, vol. 325, no. 5940, pp. 594–597, 2009.

List of Publications

Journals

1. **R. Al Mahmud**, Faruque, M. O., and R. H. Sagor, " A Highly Sensitive Plasmonic Refractive Index Sensor Based on Triangular Resonator," in *Optics Communications*, 2020
   (Under Review)

2. **R. Al Mahmud**, Faruque, M. O., and R. H. Sagor, "Plasmonic Refractive Index Sensor Based on Ring-Type Pentagonal Resonator with High Sensitivity ," in *Journal of Optoelectronics and Advanced Materials*, 2020
   (Under Review)